Dissertation
submitted to the
Combined Faculty of Mathematics, Engineering and Natural Sciences
of Heidelberg University, Germany
for the degree of
Doctor of Natural Sciences

Put forward by
Jonas Frederik Faust
born in: Leonberg
Oral examination: 23.07.2025

Rapid 3D passive needle localization
for automatic slice alignment in MR-guided interventions

Referees: Prof. Dr. Mark E. Ladd
Prof. Dr. Leif Schröder

Rapid 3D passive needle localization for automatic slice alignment in MR-guided interventions

In Magnetic Resonance Imaging (MRI)-guided needle interventions, typically 2D real-time imaging is used for the visual tracking of the needle. For imaging planes insufficiently aligned with the needle, realignment can become necessary for better needle display. In this work, techniques for the visualization of metallic needles with MRI and rapid 3D needle localization for automatic imaging plane alignment were developed and investigated.

First, the image artifact of a needle was characterized quantitatively for conventional gradient-echo (GRE) imaging with the fast low-angle shot (FLASH) technique, as well as for a positive, susceptibility-based imaging technique (dephased GRE). A model-based method for needle localization, using a baseline-subtracted radial FLASH k-space acquisition, was then developed and evaluated in phantom measurements, as well as demonstrated in an animal experiment. Additionally, a localization method based on undersampled dephased FLASH imaging and Convolutional Neural Network-based postprocessing was developed, investigated, and compared with the model-based method.

The needle artifacts were well described by the developed quantitative models (measured deviation ≤ 2 pixels). Both developed localization methods allowed for fast 3D needle localization (under 1 s). Feasibility of automatic slice alignment of 2D imaging planes with the detected needles was demonstrated retrospectively.

The developed methods for rapid, passive 3D needle localization can accelerate the workflow of MRI-guided interventions and facilitate clinical applicability.

Schnelle passive 3D Nadellokalisierung zur automatischen Schichtausrichtung bei MR-geführten Interventionen

In Magnetresonanztomographie (MRT)-geführten Nadelinterventionen wird üblicherweise eine 2D-Echtzeitbildgebung zur visuellen Verfolgung der Nadel eingesetzt. Bei unzureichender Ausrichtung der bildgebenden Schicht an der Nadel kann eine Schichtnachführung für eine bessere Darstellung der Nadel notwendig werden. In dieser Arbeit wurden Techniken zur Visualisierung metallischer Nadeln mit der MRT und zur schnellen 3D-Nadellokalisierung für eine automatische Schichtausrichtung entwickelt und untersucht.

Zunächst wurde das Bildartefakt einer Nadel für konventionelle Gradientenechobildgebung (GRE) mit der fast low-angle shot (FLASH)-Methode sowie für eine positive, suszeptibilitätsbasierte Bildgebungsmethode (dephasierte GRE) quantitativ charakterisiert. Anschließend wurde eine modellbasierte Methode zur Nadellokalisierung unter Verwendung einer referenz-subtrahierten radialen FLASH-Abtastung des k-Raums entwickelt und in Phantommessungen evaluiert sowie in einem Tierversuch demonstriert. Zusätzlich wurde eine Lokalisierungsmethode, basierend auf einer unterabgetasteten Bildaufnahme mit dephasiertem FLASH-Kontrast und einer anschließenden Bildverarbeitung mithilfe eines Convolutional Neural Networks, entwickelt, untersucht und mit der modellbasierten Methode verglichen.

Die Nadelartefakte ließen sich durch die entwickelten quantitativen Modelle gut beschreiben (gemessene Abweichungen ≤ 2 Pixel). Beide entwickelten Lokalisierungsansätze erlaubten eine schnelle 3D-Nadellokalisierung (unter 1 s). Die Möglichkeit der automatischen Ausrichtung einer 2D-bildgebenden Schicht entlang lokalisierter Nadeln wurde retrospektiv demonstriert.

Die entwickelten Methoden zur schnellen, passiven 3D-Nadellokalisierung können den Arbeitsablauf von MRT-geführten Interventionen beschleunigen und somit die klinische Anwendbarkeit vereinfachen.

Contents

List of Figures

List of Tables

List of Acronyms

ADC	analogue-to-digital converter
ASP	automatic slice positioning
bSSFP	balanced steady-state free precession
CNN	convolutional neural network
d-bSSFP	dephased balanced steady-state free precession
d-FLASH	dephased spoiled fast low-angle shot
DL	deep learning
d-SSFP	dephased steady-state free precession
FFT	fast Fourier transform
FID	free induction decay
FISP	fast imaging with steady-state free precession
FLASH	fast low-angle shot
FT	Fourier transform
GRE	gradient echo
IQR	interquartal range
MIP	maximum intensity projection
ML	machine learning
MR	magnetic resonance
MRI	magnetic resonance imaging
MSE	mean squared error
NMR	nuclear magnetic resonance
NUFFT	non-uniform fast Fourier transform
PCA	principal component analysis
PRF	proton resonance frequency
PSIF	time-reversed fast imaging with steady-state free precession
RF	radiofrequency
ROI	region of interest
SE	spin echo
SGD	stochastic gradient descent
SNR	signal-to-noise ratio
SPIO	superparamagnetic iron oxides
SSFP	steady-state free precession
VSF	voxel sensitivity function
WM	white marker

List of Symbols

γ	Gyromagnetic ratio
S	Magnetic resonance signal
$\vec{k}$	k-Space vector
$\mathcal{F}$	Fourier transform operator
$M_\perp$	Transverse magnetization
Δk	Spacing of samples in k-space
Δx	Spacing of samples in image space
t_d	Dwell time
E_m	Energy eigenstates of a spin magnetic moment in an external magnetic field
$\hat{H}$	Hamiltonian describing a spin magnetic moment in an external magnetic field
I	Spin quantum number, representing angular momentum
$\hat{\vec{I}}$	Spin operator
T	Temperature
$\hat{\rho}$	Density operator
m	Magnetic quantum number, representing projection of angular momentum along magnetic field
ω_1	Rotating frequency of rotating frame around z-axis
$M_\parallel$	Longitudinal magnetization
p_m	Occupation probability for the energy eigenstates of the spin
t_{RF}	Application time of the RF pulse
M_0	Equilibrium magnetization
N_{spins}	Number of spins in a volume
k_B	Boltzmann constant
$\vec{M}$	Magnetization vector
ω_0	Larmor frequency (for protons, also called proton resonance frequency)
B_1	Oscillating magnetic field
$\hbar$	Planck constant
B_0	Main magnetic field
B	Magnetic field
Φ_{RF}	Phase of the applied RF pulse
V	Volume
$\hat{\vec{\mu}}$	Magnetic moment operator

k_{max}	Maximum sampled wave number
$\mu_{\text{r,ext}}$	Relative magnetic permeability of the outer material, e.g., tissue
$\mu_{\text{r,in}}$	Relative magnetic permeability of the inner material, i.e., of the metallic needle
$\vec{B}_{\text{ext}}$	Magnetic field outside the infinite cylinder modeling the needle
$\vec{B}_{\text{in}}$	Magnetic field inside the infinite cylinder modeling the needle
ΔB_{susc}	Local, susceptibility-induced change in the magnetic field
$\vec{x}$	Position vector in space
N_k	Number of samples in k-space (for a respective direction)
N_x	Number of pixels in image space (for a respective direction)
q	Voxel sensitivity function
W	Density weight matrix
A_{nc}	Non-Cartesian sampling function
C	Convolution kernel for gridding procedure
θ_k	Inclination angle of a radial k-space spoke
ϕ_k	Azimuthal angle of a radial k-space spoke
d_{KB}	Width of the Kaiser-Bessel window
I_0	Zeroth-order Bessel function
β_{KB}	Emipirical shape factor for Kaiser-Bessel window
$\vec{B}_{\text{eff}}$	Effective magnetic field in the rotating frame
$\vec{M}_{\text{rot}}$	Magnetization in the rotating frame
t	Time
t_{PE}	Application time of the phase-encoding gradient
t_{FE}	Application time of the frequency-encoding gradient
T_{E}	Echo time
T_{R}	Repetition time
res	Image resolution
FOV	Field of view
bw	Receiver bandwidth
fa	Flip angle
G_{WM}	White-marker magnetic field gradient
G_{susc}	Susceptibility-induced magnetic field gradient
G_{spoil}	Spoiling magnetic field gradient
G_{FE}	Frequency-encoding magnetic field gradient
G_{PE}	Phase-encoding magnetic field gradient
$\vec{G}$	Magnetic field gradient
S'	Discretely-sampled magnetic resonance signal
$M'_{\perp}$	Spatial representation of the transverse magnetization

m_0	Induced net gradient moment at T_E
$m_{0,\mathrm{susc}}$	Susceptibilty-induced net gradient moment at T_E
$m_{0,\mathrm{WM}}$	External white-marker gradient moment at T_E
Θ	Induced phase advance between two RF pulses
N_FE	Number of frequency encoding steps
N_PE	Number of phase encoding steps
S_voxel	Signal magnitude per voxel
S_SS	Steady-state signal magnitude per voxel
S_SSC	Coherent steady-state signal magnitude per voxel
S_SSI	Incoherent steady-state signal magnitude per voxel
Δz	Voxel edge length in z-direction
d_voxel	Voxel edge length of isotropic voxel
Φ	Phase of the magnetization at t = T_E
Φ_0	Phase of the magnetization at t = 0
τ	Discrete magentization phase offset
$\bar{S}_\mathrm{d\text{-}FLASH}$	Average voxel signal magnitude for d-FLASH
$\bar{S}_\mathrm{d\text{-}SSFP}$	Average voxel signal magnitude for d-SSFP
$\bar{S}_\mathrm{d\text{-}bSSFP}$	Average voxel signal magnitude for d-bSSFP
S_voxel	Voxel signal magnitude
S_artifact	Signal magnitude for voxels that are part of the needle artifact
S_BG	Signal magnitude for voxels that are part of the background
χ_i	Magnetic susceptibility of the interior material (e.g., needle)
χ_e	Magnetic susceptibility of the exterior material (e.g., tissue)
R	Needle radius
r_FLASH	Needle artifact radius for FLASH contrast
$r_\mathrm{d\text{-}GRE}$	Needle artifact radius for d-GRE contrast variants
T_1	Longitudinal relaxation time
T_2	Transverse relaxation time
T_2^*	Transverse relaxation time including signal decay due to field inhomogeneities
T_2'	Transverse relaxation time describing signal decay due to field inhomogeneities
ρ	Effective spin density
L_object	Extend of the imaged object in the FOV
θ	Needle inclination angle to $\vec{B}_0$
ϕ	Needle azimuthal angle with $\vec{B}_0$
l	Needle insertion depth
$\vec{x}_\mathrm{ac}$	Needle artifact center

DSC	Dice similarity coefficient
d_H	Hausdorff distance
l_c	Length of the cuboid needle artifact model
w_c	Length of the cuboid needle artifact model
$\hat{\vec{v}}_{c,0}$	Unit vector along long axis of cuboid needle artifact model
$\hat{\vec{v}}_{c,1}$	Unit vector along first short axis of cuboid needle artifact model
$\hat{\vec{v}}_{c,2}$	Unit vector along second short axis of cuboid needle artifact model
Δc	Needle center-to-detected-axis deviation
Δs	Needle tip-to-detected-axis deviation
$\Delta\alpha$	Needle angular deviation
t_{recon}	Image reconstruction time
n_{spokes}	Number of k-space spokes used for image reconstruction
t_{acq}	Time of k-space acquisition
t_{loc}	Needle localization time
L^2	Mean-squared-error loss

Preface

Parts of this dissertation were published in an adapted form in peer-reviewed conference proceedings and scientific journals (see list of publications at the end of this dissertation).

Adapted versions of Section 2.3.2, Section 3.1.1, Section 4.1.1 and Section 5.1.1 were published in [1].

Adapted versions of Section 2.2.3, Section 2.3.2, Section 3.1.2, Section 4.1.2 and Section 5.1.2 were published in [2].

The methods presented in Section 3.2 and an adapted version of Section 5.2.1 were published in part in [3].

Adapted versions of Section 3.3, Section 4.3 and Section 5.2.2 were published in [4].

For all publications listed above, I, Jonas Frederik Faust, am the principle author, responsible for the developed theoretical concepts and the design of the experiments and having performed all phantom and ex-vivo data acquisition, data analysis and interpretation. All publications, including figures and tables, were drafted by me. In-vivo data was acquired during animal experiments at Cook Advanced Technology by Nathan Ooms, Jesse Roll and Joshua Krieger, following my instructions, and data with dephased GRE contrast, as well as radially-sampled FLASH data, was acquired using my MR pulse sequence implementations. In-vivo data analysis and interpretation were performed by me.

1 Introduction

Magnetic resonance (MR)-guided percutaneous needle interventions are minimally invasive medical procedures performed for diagnostic or therapeutic purposes [5–7]. These include, e.g., tissue biopsies, ablation procedures and targeted drug application. Interventions can be performed under interactive real-time image guidance employing magnetic resonance imaging (MRI), allowing the interventionalist to monitor needle placement on an in-room monitor while performing the in-bore procedure [8]. A metallic needle itself is invisible to the MRI machine because it does not contain resonant hydrogen nuclei, which are used for imaging. However, because its magnetic susceptibility differs from the tissue surrounding the needle, it will locally disturb the magnetic field which can cause an artifact in the MR image [9–11]. This artifact is usually used by the interventionalist to locate the needle and visually follow the path of the needle.

1.1 Delineation of needles in magnetic resonance imaging

The appearance of the image artifact caused by a metallic needle depends on the imaging technique, or, more specifically, on the MR pulse sequence used for the image acquisition [12]. The needle-induced inhomogeneity of the local magnetic field leads to the establishment of a magnetic field gradient in the proximity of the needle [9, 10]. For gradient echo (GRE) imaging, this field gradient can locally dephase the magnetization, leading to a decrease in signal intensity [11]. Consequently, a hypointense needle artifact is formed due to the presence of the needle. In the past, the shape and size of the needle artifact for GRE imaging have been characterized in simulations and measurements [11–17].

Furthermore, susceptibility-based, positive contrast imaging techniques have been introduced for the delineation of interventional devices [18–23]. These techniques make use of the local field inhomogeneity introduced by the needle to generate a hyperintense needle artifact on an otherwise signal-suppressed background. A popular approach is dephased GRE [20]. By the introduction of an additional external magnetic field gradient, the local needle-induced field gradient can be counteracted, leading to restoration of phase coherence and, therefore, signal intensity near the needle (referred to as white marker (WM) phenomenon [24]). Coincidentally, magnetization further away from the needle, which experiences a homogeneous magnetic field, is dephased by the external gradient (WM gradient) and the signal is suppressed. In the past, a WM gradient has been introduced in different variations of GRE pulse sequences, creating variants of the dephased GRE contrast technique: dephased spoiled fast low-angle shot (d-FLASH) [20], dephased steady-state free precession (d-SSFP) [21] and dephased balanced steady-state free

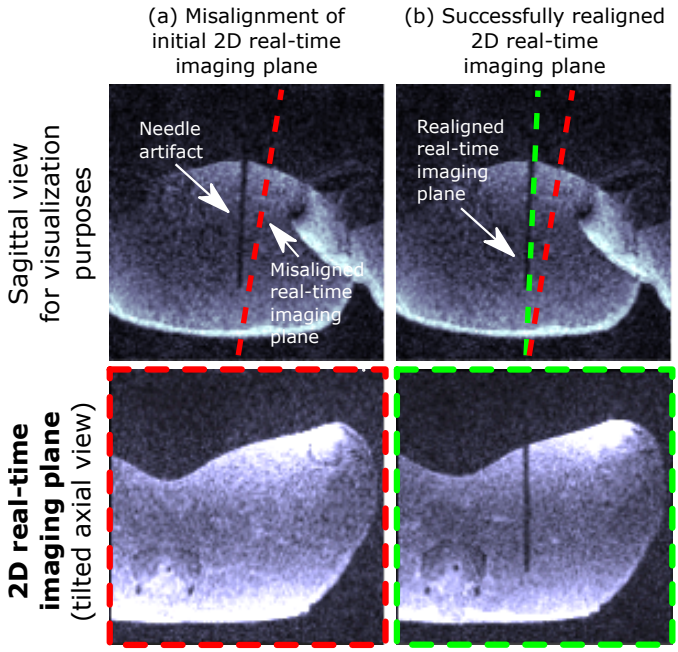

Figure 1.1: Needle intervention in a porcine animal model. (a) Misalignment of 2D real-time imaging plane with the needle artifact results in the need for correction of the position and orientation of the 2D plane. Manual correction steps can lead to longer procedure times. Incorrectly aligned planes can prevent successful image guidance during an MR intervention. (b) An (automatic) realignment of the imaging plane with the needle artifact can restore needle visibility to the interventionalist and image guidance is again feasible. Image data used in this figure was reformatted from a 3D image for demonstration purposes and has been previously published by Faust et al. [4].

precession (d-bSSFP) [25–27]. Empirically, d-bSSFP was found to be favorable to d-FLASH in terms of achieved positive artifact signal magnitude [27].

1.2 Passive needle localization for automatic slice positioning

For MR-guided in-bore needle interventions, interventionalists commonly use 2D real-time imaging planes for guidance. If the imaging slices are not correctly aligned with the needle so that the needle artifact is either only partly or not visible at all (see Fig. 1.1), visual tracking of the needle and targeting will be impaired and manual slice realignment is required. This can involve multiple iterative realignment steps, usually performed by a technologist operating the MR system during the intervention, which can complicate and prolong the workflow [8]. Alternatively, a technique for automatic slice realignment, or automatic slice positioning (ASP), can be used. Automatic methods can reduced the number of manual steps necessary and, therefore, have the potential of accelerating the interventional procedure. For an automatic slice realignment, the

orientation and position of the needle can be determined using 3D needle localization and a 2D real-time imaging slice is then automatically aligned with the detected needle trajectory. Passive localization techniques hereby only rely on the intrinsic effect of the needle (or, sometimes, attached passive markers) on the MR image, i.e., the needle artifact. They do not leverage additional electronic tracking hardware, such as, e.g., local radiofrequency (RF) coils that can be integrated into interventional devices, but are associated with additional safety risks such as RF-induced heating [28]. Various methods for 3D passive needle localization have been proposed in the past, which can be classified by the implemented type of algorithm: methods that localize the needle by matching a template image with an acquired image [29–31], methods that localize the needle by artifact segmentation in the image [32–34] or methods that optimize over a forward model to find needle positional and orientational parameters that fit to an acquired image [35, 36]. For 3D artifact segmentation, the use of convolutional neural networks (CNNs) was originally proposed by Mehrtash et al. [32]. They localized the needle artifact in intra-procedural MR images of prostate biopsies. A necessity for real-time interventions is a rapid needle localization and subsequent slice alignment to interrupt the workflow as little as possible. Full 3D MR image acquisition, as e.g. employed by Mehrtash et al., is time intensive and therefore only of limited real-time applicability. Some methods explored in the past for automatic slice alignment make use of 2D tracking slices to localize a needle trajectory in 3D which reduces acquisition times compared to a full 3D acquisition. De Oliveira et al. investigated a cross-correlation method to localize a passive marker, attached to a needle, in two 2D tracking slices [29]. Li et al. proposed to localize the needle artifact in multiple adjacent image slices, using a CNN, which would then allow for the alignment of a 2D real-time slice with the needle trajectory [33]. Strehl et al. proposed a 3D needle tracking approach based on modeling the needle artifact in multiple 2D images, parallel and orthogonal to the needle path, and evaluated the method in phantoms [35]. 2D tracking slices require pre-positioning before the localization which can also complicate and prolong the workflow, making a fully-3D needle localization with a rapid/accelerated, and therefore real-time applicable acquisition desirable.

In this work, the artifact of a biopsy needle was characterized for GRE (more specifically fast low-angle shot (FLASH)), as well as dephased GRE imaging as a first step. For FLASH, the artifact was quantitatively compared to a simple dephasing model. For dephased GRE, artifact size and shape were theoretically derived and validated in measurements for the three variants d-FLASH, d-SSFP and d-bSSFP. For that purpose, models were introduced to describe the positive signal formation in d-SSFP and d-bSSFP. Characteristics of the emerging positive signal were then compared for the related dephased GRE techniques, including d-FLASH. In a second step, a method for rapid 3D needle localization, based on modeling baseline-subtracted radial FLASH k-space data, was introduced and investigated for the purpose of ASP. To accelerate the method, localization from only a limited number of sampled k-space lines was evaluated. In a third and last step, an alternative method for rapid 3D needle localization without the need for a baseline scan before the insertion (as required by the first investigated method) was proposed and investigated, using an undersampled positive contrast acquisition with d-FLASH and a CNN-based postprocessing algorithm.

2 Theory

This chapter provides an overview on the theoretical background essential for the investigations conducted in this dissertation. After a condense general introduction to the origin of the MR signal and MR imaging, the effect of a metallic needle in MRI is analyzed for the two imaging techniques used in this work, GRE (more specifically FLASH) and dephased GRE imaging. Lastly, a theoretical motivation for needle localization from an undersampled k-space acquisition is given.

2.1 MR imaging basics

This section introduces the fundamental principles of the generation, acquisition and spatial encoding of the MR signal, as well as the reconstruction of MR images. More detailed explanations on MR imaging can be found in the standard literature by Slichter [37], Brown et al. [38] and Bernstein et al. [39].

2.1.1 Proton spin and macroscopic magnetization

At the basis of MRI lies the nuclear spin, a quantum-mechanical angular momentum carried by atomic nuclei with an odd number of nucleons. It can be represented by the operator $\hat{\vec{I}}$ and is linked to a magnetic moment

$$\hat{\vec{\mu}} = \gamma \hat{\vec{I}}. \tag{2.1}$$

Here, γ is the gyromagnetic ratio. For conventional proton MRI, making use of the spin of hydrogen nuclei, the proton gyromagnetic ratio is used.

For the spin operator with $\hat{\vec{I}} = (\hat{I}_x, \hat{I}_y, \hat{I}_z)$, the following commutator relations hold:

$$\begin{aligned} [\hat{I}_i, \hat{I}_j] &= \epsilon_{ijk} \hbar \hat{I}_k \\ [\hat{\vec{I}}^2, \hat{I}_i] &= 0 \end{aligned} \tag{2.2}$$

Choosing the z-axis as the axis of quantization, we find the eigenvalue equations:

$$\begin{aligned} \hat{\vec{I}}^2 |I, m\rangle &= I(I+1)\hbar^2 |I, m\rangle, \\ \hat{I}_z |I, m\rangle &= m\hbar |I, m\rangle. \end{aligned} \tag{2.3}$$

The eigenfunctions $|I, m\rangle$ of the spin operator are characterized by the spin quantum number I, which has a value of $\frac{1}{2}$ for protons, and the magnetic quantum number m, for which we find values from $-I$ to I in integer steps, ergo $\pm\frac{1}{2}$ for protons.

Let a spin magnetic moment with operator $\hat{\vec{\mu}}$ now be placed in an external magnetic field $\vec{B}_0 = (0, 0, B_0)$, which is aligned here in the z-direction without loss of generality. The system's behavior can be described with the Hamiltonian

$$\hat{H} = -\hat{\vec{\mu}}\vec{B}_0 = -\gamma B_0 \hat{I}_z. \tag{2.4}$$

To find the energy eigenvalues of the quantum states, we solve the time-independent Schrödinger equation

$$\hat{H}|I, m\rangle = E_m|I, m\rangle, \tag{2.5}$$

The splitting of quantum energy states in an external magetic field is called the Zeeman effect [40]. With $m = \pm\frac{1}{2}$, we find that the two possible energy eigenvalues for the proton spin are given by

$$E_m = -m\gamma\hbar B_0. \tag{2.6}$$

We now consider an ensemble of nuclear spins. The occupation probability p_m for the energy eigenstates of the spins is governed by the Boltzmann distribution with

$$p_m = \frac{1}{\sum_{m=-I}^{I} e^{-\frac{E_m}{k_B T}}} e^{-\frac{E_m}{k_B T}}, \tag{2.7}$$

where k_B is the Boltzmann constant and T is the temperature. To describe the statistics of a quantum-mechanical system occupying the quantum eigenstates $|I, m\rangle$ with the occupation probability p_m as introduced above, the density operator $\hat{\rho}$ is used with

$$\hat{\rho} = \sum_m p_m |I, m\rangle\langle I, m|. \tag{2.8}$$

For a spin from an ensemble prepared as above and described by the density operator $\hat{\rho}$, we can now calculate the expectation value for $\hat{I}_i$ as

$$\langle \hat{I}_i \rangle = \mathrm{Tr}\{\hat{\rho}\hat{I}_i\}. \tag{2.9}$$

At room temperature, the exponential function of the Boltzmann distribution can be approximated by a first-order Taylor expansion as $E_m \ll k_B T$. For an ensemble of spins, calculating the sum of the expectation values $\langle \hat{I}_z \rangle$ for all N_{spins} spins per volume V results in the macroscopic magnetization along z-direction

$$M_z = \frac{1}{V}\sum_{i=1}^{N_{\text{spins}}} \langle \hat{\mu}_z \rangle = \frac{1}{V}\sum_{i=1}^{N_{\text{spins}}} \gamma \langle \hat{I}_z \rangle \simeq \frac{N_{\text{spins}}\hbar^2\gamma I(I+1)B_0}{V 3 k_B T}. \tag{2.10}$$

An analogous treatment as above for the x- and y-components of the spin magnetic moment leads to vanishing expectation values in thermal equilibrium with the magnetic field oriented in z-direction. We therefore find the equilibrium magnetization $\vec{M}_0 = (0, 0, M_0)$ oriented along the $\vec{B}_0$-field with

$$M_0 \simeq \frac{N_{\text{spins}} \gamma^2 \hbar^2 B_0}{V 4 k_B T}. \tag{2.11}$$

2.1.2 Equation of motion and relaxation processes

The dynamics of a quantum-mechanical ensemble are described by the von-Neumann equation

$$i\hbar \frac{d\hat{\rho}}{dt} = [\hat{H}, \hat{\rho}]. \tag{2.12}$$

We can use Eq. 2.12 to calculate the time evolution of the expectation value of the magnetic moment as given in Eq. 2.9. As the magnetic moment $\hat{\vec{\mu}}$ as given in Eq. 2.1 is not explicitly time-dependent, we get

$$\frac{\mathrm{d}\langle\hat{\vec{\mu}}\rangle}{\mathrm{d}t} = -\frac{i}{\hbar}\langle[\hat{\vec{\mu}}, \hat{H}]\rangle. \tag{2.13}$$

Inserting the Hamiltonian from Eq. 2.4 and applying the commutator relations for the angular momentum from Eq. 2.3 yields the equation of motion for the macroscopic magnetization

$$\frac{\mathrm{d}\vec{M}}{\mathrm{d}t} = \vec{M} \times \gamma \vec{B}. \tag{2.14}$$

This equation is analogous to the equation describing a classical spinning top. For a magnetization oriented in z-direction, which is also called the longitudinal magnetization $M_\parallel$, the time derivative of $\vec{M}$ vanishes, resulting in a constant time evolution. If the magnetization has a component orthogonal to the z-direction, the equation describes a precession movement of the magnetization around the direction of the magnetic field $\vec{B}$. Introducing a complex description of the magnetization in the xy-plane, which is also called the transversal magnetization $M_\perp$, the solution to Eq. 2.14 is calculated as

$$\begin{aligned} M_\parallel(t) &= M_\parallel(0) \\ M_\perp(t) &= M_x(t) + iM_y(t) \\ &= M_\perp(0) e^{-i\omega_0 t + i\Phi_0} \end{aligned} \tag{2.15}$$

Here, ω_0 describes the precession frequency of the transversal magnetization and Φ_0 is a phase offset at time $t = 0$. ω_0 is called the Larmor frequency or, for proton nuclear magnetic resonance (NMR), the proton resonance frequency (PRF), with

$$\omega_0 = \gamma B_0, \tag{2.16}$$

The solution describes the magnitude of the longitudinal and transversal magnetization as time-independent. However, in reality, the magnetization in the xy-plane decreases with time while

the magnetization in z-direction returns to the thermal equilibrium value provided in Eq. 2.11. To describe these effect mathematically, Bloch introduced two relaxation terms to Eq. 2.14, leading to the phenomenological Bloch equations of motion [41]

$$\begin{aligned}\frac{\mathrm{d}M_x}{\mathrm{d}t} &= \gamma(\vec{M}\times\vec{B})_x - \frac{M_x}{T_2},\\ \frac{\mathrm{d}M_y}{\mathrm{d}t} &= \gamma(\vec{M}\times\vec{B})_y - \frac{M_y}{T_2},\\ \frac{\mathrm{d}M_z}{\mathrm{d}t} &= \gamma(\vec{M}\times\vec{B})_z - \frac{M_0 - M_z}{T_1}.\end{aligned} \tag{2.17}$$

Here, the relaxation parameter T_1 describes the return of the longitudinal magnetization to its equilibrium state while the parameter T_2 describes the decay of the transversal magnetization. The solutions for the Bloch equations are found as

$$\begin{aligned}M_{\parallel}(t) &= M_0 - \left(M_0 - M_{\parallel}(0)\right) e^{-\frac{t}{T_1}},\\ M_{\perp}(t) &= M_{\perp}(0) e^{-\frac{t}{T_2}} e^{-i\omega_0 t + i\Phi_0}.\end{aligned} \tag{2.18}$$

The decay of the transversal magnetization is attributed to a loss of phase coherence of the individual spins due to mutual interaction. An additional dephasing effect can appear due to a time-constant local distortion of the magnetic field, described by the relaxation constant $T_2^{'}$. To account for this effect, the effective relaxation constant T_2^* can be introduced with

$$\frac{1}{T_2^*} = \frac{1}{T_2} + \frac{1}{T_2^{'}} \tag{2.19}$$

To account for transversal relaxation with T_2^*, it can be swapped with T_2 in the solution to the Bloch equations given by Eq. 2.18. The dephasing attributed to a local field disturbance is reversible, in contrast to pure T_2 relaxation (see Section 2.2.1 on the spin-echo imaging technique). The decay of the transversal magnetization over time is called free induction decay (FID).

2.1.3 Magentic resonance and NMR signal

The underlying physical principle of MRI is the NMR phenomenon, which was discovered by Bloch [41], Purcell et al. [42] and Rabi et al. [43]. It describes the manipulation of the nuclear spin, placed in an external magnetic field, by an oscillating magnetic field and, in response, the production of an electromagnetic signal. For a large ensemble of spins as introduced above, the response of the macroscopic magnetization to an oscillating magnetic field can be understood from the equation of motion Eq. 2.14. In thermal equilibrium, the magnetization $\vec{M}$ is oriented along the direction of the main magnetic field $\vec{B}_0$ as described in Section 2.1.1. By applying a RF-excitation, the orientation of $\vec{M}$ can be manipulated. We introduce the oscillating magnetic field $\vec{B}_1$ with

$$\vec{B}_1(t) = B_1(\vec{e}_x \cos(\omega_1 t + \Phi_{\mathrm{RF}}) + \vec{e}_y \sin(\omega_1 t + \Phi_{\mathrm{RF}})), \tag{2.20}$$

where $\vec{e}_x$ and $\vec{e}_z$ are the unit vectors along the x- and the z-axis. The field is oriented orthogonally to the main magnetic field $\vec{B}_0$ and circularly polarized with the frequency ω_1 and a phase offset Φ_{RF}. For a simpler calculation, the reponse of the magnetization to the oscillating field can be investigated in a coordinate frame rotating with ω_1 around the z-axis. The effective magnetic field is then given by

$$\vec{B}_{\text{eff}} = \frac{(\omega_0 - \omega_1)\,\vec{e}_{z'} + \omega_1(\vec{e}_{x'}\cos(\Phi_{\text{RF}}) + \vec{e}_{y'}\sin(\Phi_{\text{RF}}))}{\gamma}, \tag{2.21}$$

where $\vec{e}_{x'}$ and $\vec{e}_{z'}$ are the unit vectors in the rotating coordinate system. We can rephrase equation Eq. 2.14 in the rotating frame as

$$\frac{d}{dt}\vec{M}_{\text{rot}} = \gamma\vec{M}_{\text{rot}} \times \vec{B}_{\text{eff}}. \tag{2.22}$$

For the on-resonant case $\omega_0 = \omega_1$, the z'-component of the effective magnetic field disappears and we find the solution to Eq. 2.22 as

$$\vec{M}_{\text{rot}} = M_0[(\sin(\omega_1 t)\cos(\Phi_{\text{RF}}))\vec{e}_{x'} + (\sin(\omega_1 t)\sin(\Phi_{\text{RF}}))\vec{e}_{y'} + \cos(\omega_1 t)\vec{e}_{z'}]. \tag{2.23}$$

Magnetization is therefore rotated around the rotation axis $\vec{e}_x\cos(\Phi_{\text{RF}}) + \vec{e}_y\sin(\Phi_{\text{RF}})$ with the so-called flip angle

$$\text{fa} = \int_0^{t_{\text{RF}}} \omega_1(t)\,\mathrm{d}t = \gamma\int_0^{t_{\text{RF}}} B_1(t)\,\mathrm{d}t, \tag{2.24}$$

where t_{RF} is the duration time of the RF pulse. Changing the orientation of B_1 in the rotating frame (phase of the RF pulse) therefore allows a change in rotation axis of the magnetization. For the rectangular-shaped RF pulses used in this work (hard pulses), Eq. 2.24 can be simplified to

$$\text{fa} = \gamma t_{\text{RF}} B_1(t). \tag{2.25}$$

A precessing magnetization in the transverse plane can induce a current in a coil which is placed near the excited volume (Faraday induction). The magnitude of the signal depends on system-dependent factors, such as coil sensitivities or amplification, but is proportional to the magnitude of the transversal magnetization:

$$S(t) \propto M_\perp(0)e^{-\frac{t}{T_2^*}}e^{-i\omega_0 t + i\Phi_0}. \tag{2.26}$$

2.1.4 Spatial signal encoding and image reconstruction

Magnitude and phase of the local magnetization generally vary across the investigated volume, e.g., due to differences in spin density or relaxation times and local differences in magnetic field strength due to distortions in the main magnetic field. A spatially varying MR signal constitutes

the origin of the MR image contrast. To spatially encode the signal, external magnetic field gradients $\vec{G}(t)$ can be applied to the magnetization [44]:

$$\begin{aligned}\vec{G}(t) &= \frac{\partial B_z(t)}{\partial x}\vec{e}_x + \frac{\partial B_z(t)}{\partial y}\vec{e}_y + \frac{\partial B_z(t)}{\partial z}\vec{e}_z \\ &= G_x(t)\vec{e}_x + G_y(t)\vec{e}_y + G_z(t)\vec{e}_z\end{aligned} \tag{2.27}$$

A spatially varying magnetic field due to an external gradient introducing a linear field variation in space causes a local change in Larmor frequency

$$\omega(\vec{x}, t) = \gamma(B_0 + \vec{x}\vec{G}(t)). \tag{2.28}$$

Here, $\vec{x}$ describes the position vector in space. If the gradient is applied for a time t, local magnetization will acquire a phase

$$\Phi(\vec{x}, t) = \gamma \int_0^t \vec{G}(t')\, dt'\vec{x} = 2\pi\vec{k}(t)\vec{x}. \tag{2.29}$$

Here, the wave vector $\vec{k}$ was defined as

$$\vec{k}(t) = \frac{\gamma}{2\pi} \int_0^t \vec{G}(t')\, \mathrm{d}t'. \tag{2.30}$$

The measured MR signal is proportional to the transverse magnetization integrated over the sensitivity volume of the coil. As elucidated in Section 2.1.2, the magnitude of the transverse magnetization will depend on the initial value after excitation and, due to transverse relaxation, on the time of acquisition. The time after which the center of k-space is acquired is called echo time T_E. Neglecting relaxation effects during the acquisition process, we find the expression

$$S(\vec{k}(t)) \propto \int_V M_\perp(\vec{x}, T_\mathrm{E}) e^{-2\pi i\vec{k}(t)\vec{x}}\, \mathrm{d}\vec{x} \equiv \mathcal{F}\{M_\perp(\vec{x}, T_\mathrm{E})\} \tag{2.31}$$

We can see from Eq. 2.31 that the measured signal $S(\vec{k}(t))$ is given by the Fourier transform (FT) of the local magnetization $\mathcal{F}\{M_\perp(\vec{x}, T_\mathrm{E})\}$. The magnitude and phase of the local magnetization can therefore be determined by performing an inverse FT on the acquired signal

$$M_\perp(\vec{x}, T_\mathrm{E}) \propto \int S(\vec{k}(t)) e^{2\pi i\vec{k}(t)\vec{x}}\, \mathrm{d}\vec{k} \equiv \mathcal{F}^{-1}\{S(\vec{k}(t))\}. \tag{2.32}$$

Using different gradient coils, it is possible to generate magnetic field gradients in all three spatial directions. In this way, different values for $\vec{k}(t)$ can be generated. Applying the gradient fields with different timings and order allows to acquire the various parts of the so-called k-space, following different types of trajectories (see below for Cartesian and non-Cartesian sampling). For 2D imaging, a slice selection technique can be applied before the encoding of k-space. Using

tailored RF pulses while applying a magnetic field gradient in slice selection direction allows to only excite magnetization in a slice with a certain thickness and not all of the investigated volume, making a subsequent 2D k-space encoding of the excited slice sufficient for image generation. As only 3D k-space encodings were used in the scope of this thesis, the slice selection technique is not further discussed here.

Cartesian acquisition

As described above, the spatial information of the image is encoded in the MR signal using magnetic field gradients. Applying magnetic field gradients subsequently in varying spatial directions allows to acquire k-space data, following a certain k-space trajectory. After the acquisition of k-space, an image of the local magnetization can be reconstructed by means of a multidimensional FT (compare Eq. 2.32). For Cartesian imaging techniques, k-space is sampled by traversing it along parallel lines. Discrete sampling points are hereby placed on an evenly spaced finite sampling grid.

For a 3D Cartesian readout of k-space, usually, after excitation of the magnetization, a position at the edge of k-space is first selected by applying so-called phase encoding gradients $\vec{G}_{\text{PE}}$ (prior to the actual acquisition). The k-space is then subsequently traversed while acquiring the data in regular intervals, applying a gradient $\vec{G}_{\text{FE}}$ in so-called frequency encoding direction. The signal is hereby discretly sampled by the MR hardware, using a so-called analogue-to-digital converter (ADC). Without loss of generality, we choose a phase encoding in x- and y-direction and a readout in z-direction. In this case, Cartesian sampling can therefore be described by the acquired wave vectors

$$\begin{aligned}\vec{k}_{\text{Cartesian}} &= m\frac{\gamma G_{\text{PE},x} t_{\text{PE,x}}}{N_{\text{PE},x}}\vec{e}_x + j\frac{\gamma G_{\text{PE,y}} t_{\text{PE,y}}}{N_{\text{PE},y}}\vec{e}_y + p\frac{\gamma G_{\text{FE}} t_{\text{FE}}}{N_{\text{FE}}}\vec{e}_z \\ &= m\Delta k_{\text{PE,x}}\vec{e}_x + j\Delta k_{\text{PE,y}}\vec{e}_y + p\Delta k_{\text{FE}}\vec{e}_z.\end{aligned} \tag{2.33}$$

Here, $t_{\text{PE},x}$ and $t_{\text{PE,y}}$, as well as t_{FE} describe the application times of the respective gradients and $m = -\frac{N_{\text{PE},x}}{2}, \ldots, \frac{N_{\text{PE},x}}{2} - 1$, $j = -\frac{N_{\text{PE},y}}{2}, \ldots, \frac{N_{\text{PE},y}}{2} - 1$ and $p = -\frac{N_{\text{FE}}}{2}, \ldots, \frac{N_{\text{FE}}}{2} - 1$ are defined with the number of sampling steps $\frac{N_{\text{PE},x}}{2}$, $\frac{N_{\text{PE},y}}{2}$, $\frac{N_{\text{FE}}}{2}$ in each respective encoding direction. The time interval between the acquisition of two samples for the frequency encoding step is called the dwell time t_d, from which the receiver bandwidth is defined as

$$\text{bw} = \frac{1}{t_d} = \frac{N_{\text{FE}}}{t_{\text{FE}}} = \frac{\gamma G_{\text{FE}}}{\Delta k_{\text{FE}}}. \tag{2.34}$$

By subsequent acquisition of parallel k-space lines with varying phase encoding, k-space is filled during the acquisition process. Commonly, RF excitation pulses are applied between the acquisition of different lines of k-space to (re-)excite the magnetization that, in practice, strives back to its equilibrium value with time due to relaxation. The time between RF excitation pulses is called repetition time T_{R}. Depending on the timing and type of applied gradients and RF pulses, different magnetization states can be reached, including different types of steady-state

magnetization, leading to differences in established contrast for the various techniques (see Section 2.2).

Acquiring discrete samples of the continuous k-space signal, given in Eq. 2.31, as described by Eq. 2.33 has consequences for image reconstruction. The discrete sampling of the signal can be mathematically described with the sampling or "comb" function

$$\text{Ш}_{\Delta k}(k) = \frac{1}{\Delta k}\,\text{Ш}\left(\frac{k}{\Delta k}\right) \equiv \sum_{n=-\infty}^{\infty} \delta(k - n\Delta k). \tag{2.35}$$

Here δ denotes the Dirac delta function. While Eq. 2.35 represents the one-dimensional sampling function, a generalization to multiple dimensions is straight forward. For the sake of brevity, we continue here with the 1D sampling function. Its FT is given by

$$\mathcal{F}\{\text{Ш}_{\Delta k}(k)\} = \frac{1}{\Delta k}\text{Ш}_{1/\Delta k}(x) = \text{Ш}(\Delta k x). \tag{2.36}$$

The discretely sampled signal $S'(k)$ can be represented by multiplying the continuous signal $S(k)$ with Eq. 2.35:

$$S'(k) = S(k) \cdot \text{Ш}_{\Delta k}(k) = \sum_{n=-\infty}^{\infty} S(n\Delta k)\,\delta(k - n\Delta k). \tag{2.37}$$

Applying a FT to Eq. 2.37 allows to calculate the spatial representation of the transverse magnetization

$$M'_{\perp}(x) = \mathcal{F}^{-1}\{S'(k)\} \propto M_{\perp}(x) * \text{Ш}(\Delta k x) = \frac{1}{\Delta k}\sum_{n=-\infty}^{\infty} M_{\perp}\left(x - \frac{n}{\Delta k}\right). \tag{2.38}$$

From Eq. 2.38, we can see that the spatial representation of the magnetization $M'_{\perp}(x)$ is given by periodic repetition of the physical magnetization $M_{\perp}(x)$ with the sampling rate $\frac{1}{\Delta k}$, allowing the definition of the FOV as

$$\text{FOV} = \frac{1}{\Delta k}. \tag{2.39}$$

If the imaged object (with extend L_{object} in the respective spatial direction) is larger than the FOV, the reconstructed image will present with so-called aliasing artifacts, allowing the formulation of the so-called Nyquist-Shannon sampling theorem as a criterion for aliasing-free imaging [45]:

$$\Delta k < \frac{1}{L_{\text{object}}}. \tag{2.40}$$

In practice, k-space is not only sampled discretly, but also only up to a maximum wave number $k_{\text{max}} = \frac{N_k \Delta k}{2}$ in the respective direction, with N_k being the total number of k-space points sampled (compare Eq. 2.33). The finite sampling can be mathematically modeled by multiplying the discretized signal equation Eq. 2.37 with the rectangular function

$$\text{rect}\left(\frac{k}{2k_{\text{max}}}\right) = \begin{cases} 0, & \text{if } |k| > \frac{2k_{\text{max}}}{2} \\ \frac{1}{2}, & \text{if } |k| = \frac{2k_{\text{max}}}{2} \\ 1, & \text{if } |k| < \frac{2k_{\text{max}}}{2}, \end{cases} \tag{2.41}$$

with the width of the acquired k-space $2k_{\text{max}} = N_k \Delta k$. We can calculate the FT of Eq. 2.41 as

$$\mathcal{F}\left\{\text{rect}\left(\frac{k}{2k_{\text{max}}}\right)\right\} = 2k_{\text{max}}\,\frac{\sin(\pi 2k_{\text{max}}x)}{\pi 2k_{\text{max}}x} \equiv 2k_{\text{max}}\,\text{sinc}\left(\pi 2k_{\text{max}}x\right). \tag{2.42}$$

The discretely sampled signal with finite support in k-space can hence be expressed as the multiplication of the continuous signal with infinite support $S(k)$ with the

$$S'(k) = S(k)\cdot \text{Ш}_{\Delta k}(k)\cdot \text{rect}\left(\frac{k}{2k_{\text{max}}}\right) = \sum_{n=-N_k/2}^{N_k/2-1} S(n\Delta k)\,\delta(k-n\Delta k). \tag{2.43}$$

Applying the FT again allows us to find an expression for the spatial representation of the transverse magnetization (now for discrete and finite sampling)

$$M'_{\perp}(x) = \mathcal{F}^{-1}\{S'(k)\} \propto M_{\perp}(x) * \text{Ш}(\Delta k x) * 2k_{\text{max}}\,\text{sinc}(\pi 2k_{\text{max}}x). \tag{2.44}$$

The image of the transverse magnetization is convoluted with a sinc-function, leading to a blurring in the image. The resolution of MR image is usually described as the physical distance between two objects that can still be visually separated in an image. A possible definition of the resolution is therefore given by the distance between the maximum of the sinc function and its first minimum

$$\text{res} = \frac{1}{2k_{\text{max}}}. \tag{2.45}$$

To reconstruct an image from the discretly sampled k-space, a discrete FT can be employed. An acquisition of N_k samples allows the reconstruction of N_x voxels with voxel edge length res in the respective direction. The reconstructed intensity for each voxel is hereby not merely the complex sum of the magnetization across the voxel, but is defined by the voxel sensitivity function (VSF), which can be deduced directly from the characteristics of the FT [46]:

$$q(x) = \frac{1}{N_x}\cdot\frac{\sin\left(\pi\frac{x}{\Delta x}\right)}{\sin\left(\pi\frac{x}{N_x\Delta x}\right)}. \tag{2.46}$$

Here, Δx is the width of the voxel in the respective spatial direction. Partial magnetization from off-center locations in a voxel is therefore underrepresented in the reconstructed image. For example, with $N_x = 64$, only a fraction of $q(\frac{\Delta x}{2}) \approx 0.64\,q(0)$ of partial magnetization from the voxel edge will contribute to the voxel's intensity.

An advantage of Cartesian sampling is that due to sampling on the regular grid, the fast and computationally efficient fast Fourier transform (FFT) algorithm can be used for rapid image reconstruction [47].

Non-Cartesian acquisition

The magnetic field gradients in the different spatial directions (Eq. 2.27) can be arbitrarily combined. This allows the traversing of k-space following non-Cartesian trajectories. Traversing k-space along straight lines through it's origin with a varying spherical angle constitutes a radial k-space trajectory, as was also used in this thesis. The coordinates in k-space along one radial spoke, defined by its angular orientation (θ_k, ϕ_k), are given as

$$\vec{k}_{\text{radial}} = m\Delta k_{\text{FE}} \sin\theta_k \cos\phi_k \, \vec{e}_x + m\Delta k_{\text{FE}} \sin\theta_k \sin\phi_k \, \vec{e}_y + m\Delta k_{\text{FE}} \sin\phi_k \, \vec{e}_z. \tag{2.47}$$

with $m = -\frac{N_{\text{FE}}}{2}, \ldots, \frac{N_{\text{FE}}}{2} - 1$. The direction of the frequency encoding changes with the angular orientation of the spoke.

If the trajectory sampling the k-space does not follow the Cartesian grid, the application of the FFT algorithm is not directly applicable. Instead, a so-called non-uniform fast Fourier transform (NUFFT) can be performed to reconstruct the image from the acquisition. The application of a NUFFT for non-Cartesian image reconstruction was, e.g., summarized by Pauly et al. [48] or Block [49]. It includes the following steps:

1. Sampling of the k-space on a non-cartesian grid
2. Density compensation to counterbalance a disproportionally sampled k-space
3. Convolution of the k-space samples with an interpolation kernel (gridding [50])
4. Evaluation of the interpolated k-space on a Cartesian grid
5. Inverse FFT to transform k-space to image space
6. Correction for apodization by division with the FT of the interpolation kernel
7. Cropping of the image to chosen FOV to remove oversampling

We can therefore express the spatial representation of the transverse magnetization after the NUFFT procedure with the equation

$$M_\perp{}'(x) = \mathcal{F}\{[(S(k) \cdot A_{\text{nc}}(k) \cdot W(k)) * C(k)] \cdot \text{Ш}_{\Delta k}(k)\} / \mathcal{F}\{C(k)\} \tag{2.48}$$

Here, $C(k)$ is a gridding kernel (with its FT given by $\mathcal{F}\{C(k)\}$), $A_{\text{nc}}(k)$ is the non-Cartesian sampling function and $W(k)$ is the weighting function for the density compensation. The gridded k-space can then be transformed to image space using the standard FFT procedure, similar to Cartesian image reconstruction.

The non-Cartesian sampling function $A_{\text{nc}}(k)$ is defined by the non-equidistantly distributed samples in k-space k_i, defined by the k-space trajectory as, e.g., given in Eq. 2.47:

$$A_{\text{nc}}(k) = \sum_i \delta(k - k_i). \tag{2.49}$$

For the interpolation kernel, usually a Kaiser-Bessel function is chosen as a finite approximation of the sinc function [51], which corresponds to a rectangular function in image space

$$C(k) = \begin{cases} \frac{1}{d_{\text{KB}}} I_0 \left(\beta_{\text{KB}} \sqrt{1 - \left(\frac{2k}{d_{\text{KB}}} \right)^2} \right) & \text{for } |k| \leq \frac{d_{\text{KB}}}{2} \\ 0 & \text{for } |k| > \frac{d_{\text{KB}}}{2} \end{cases} \tag{2.50}$$

Here, I_0 is the zeroth-order Bessel function, d_{KB} is the width of the Kaiser-Bessel window and β_{KB} is an empirically determined shape factor [52].

Many non-Cartesian trajectories sample the k-space unevenly, e.g. acquiring disproportionally many samples from the center region. To counteract this imbalance, each acquired k-space point must be weighted according to the local sampling density. Pipe et al. proposed a numerical iterative method to calculate the weightings for each sampling point, which takes the coordinates of the sampled k-space points as input [53]. Initializing the weights as a matrix of ones W_0, the weight matrix is iteratively updated with

$$W_{t+1} = \frac{W_t}{(C\mathcal{F})(C\mathcal{F})^{\text{H}} W_t}. \tag{2.51}$$

Here, C is again the chosen interpolation kernel and $\mathcal{F}$ denotes theFFT. After a chosen number of iterations, the final weight matrix is extracted.

The convolution of the non-uniformly sampled k-space with a finite gridding kernel (apodization) will lead to a modulation of the image space signal with the Fourier transform of the kernel. This can be corrected for by deviding the image space signal by the kernel's Fourier transform.

The use of a finite interpolation kernel also leads to the occurrence of side lobes, signal originally placed outside the FOV, but aliased back into the image. Typically, a two-fold oversampling is used for non-Cartesian imaging in the frequency readout direction, allowing the reconstruction of a FOV twice as large. Aliasing will now mainly affect the image outside the original FOV size to which the image is then cropped in a final step of the NUFFT procedure.

To prevent aliasing in the image when, e.g., encoding k-space using a radial trajectory, the Nyquist-Shannon sampling theorem must be fulfilled not only for the frequency encoding direction, but also for angular sampling. The distance between two radial spokes through the k-space center will be greatest for the outmost points of the spokes. From Eq. 2.40, we can infer a limitation for the angular sampling increments $\Delta\phi_k$ and $\Delta\theta_k$:

$$k_{\text{max}} \Delta\phi_k = k_{\text{max}} \Delta\theta_k = \frac{1}{\text{FOV}}. \tag{2.52}$$

Considering a uniform angular distribution of center-through k-space spokes, we can calculate the required number of spokes N_{spokes} to prevent aliasing, making use of the spherical angle 4π, as (cf. Park et al. [54])

$$N_{\text{spokes}} = \frac{1}{2} \frac{4\pi}{\Delta\phi_k \Delta\theta_k} = 2\pi \left(\frac{N_{\text{FE}}}{2} \right)^2. \tag{2.53}$$

Undersampling k-space in the angular dimension, i.e. sampling less radial k-space spokes than required by Eq. 2.53, will cause the image to present with characteristic streaking artifacts, lines of high signal intensity extending through the image.

2.2 Image contrast and MR pulse sequences

The contrast of an MR image is determined by the magnitude and phase of the local transverse magnetization, as described in Section 2.1.4. The magnitude of the local signal hereby depends on various tissue parameters, for example spin density, the initial value of the transverse magnetization after excitation, and relaxation constants, while the phase can be influenced by local inhomogeneities in the magnetic field.

An MR pulse sequence describes a series of RF pulses, used for the excitation of transverse magnetization in an MR acquisition, and external magnetic field gradient moments, applied by the MRI machine, that also influence magnitude and phase of the local magnetization. In the following, the sequence types used in this thesis will be introduced.

2.2.1 Spin-echo imaging

In a spin echo (SE) acquisition, magnetization is flipped into the transversal plane by an initial excitation RF pulse. Local inhomogeneities in the magnetic field can lead to an intra-voxel phase distribution, which can cause a decrease in signal due to destructive interference of the partial magnetization (T_2^* relaxation, see Section 2.1.2). To counteract the decay of signal due to local inhomogeneities in the magnetic field, an additional RF puls is introduced to the sequence after the initial excitation pulse. This second RF pulse is usually applied after a time of $\frac{T_\mathrm{E}}{2}$ with a flip angle of fa $= 180°$, so that it reverses the orientation of the magnetization in the transverse plane and causes a rephasing ("spin echo" [55]) of the magnetization at T_E, which is then sampled by the ADC. Common implementations of SE sequences can be found in the standard literature, such as in Bernstein et al. [39].

SE sequences can, e.g., be used to create T_2-weighted images, as influences leading to T_2^* relaxation are reversed by the $180°$ pulse. The SE sequence type is therefore also inherently immune to dephasing artifacts caused by metallic devices, e.g., biopsy needles, that can invoke a magnetic field inhomogeneity in their proximity (see Section 2.3 below). In this thesis, SE sequences were used only for the acquisition of reference scans without needle dephasing artifacts.

2.2.2 Gradient-echo imaging

In GRE imaging, no extra RF pulse is played out between the excitation pulse and the acquisition, i.e., the FID is sampled directly. For GRE sequences, typically RF-spoiled GRE (commonly called RF-spoiled FLASH, or simply FLASH) and (balanced) steady-state free precession (SSFP)

are distinguished [56]. The signal and contrast of an image acquisition depend on the used GRE sequence subtype and is described in the following sections.

For the different GRE sequence types, different magnetization steady-states S_{SS} can be established which govern the general signal magnitude. For GRE sequences, image contrast will also be determined by the intra-voxel phase distribution Φ as, compared to the SE technique, an accumulated phase difference between partial magnetization is not (fully) reversed and signal from partial magnetization within a voxel will interfere either constructively or destructively, depending on the respective local phase. For an intra-voxel phase distribution $\Phi(z)$ established along a voxel of edge length Δz, neglecting relaxation processes and assuming a uniform voxel sensitivity function (therefore neglecting Eq. 2.46), the integrated voxel signal magnitude can be expressed by (cf., e.g., Bakker et al. [20])

$$S_{\mathrm{voxel}} = S_{\mathrm{SS}} \left| \int \mathrm{rect}(\frac{z}{\Delta z}) e^{-i\Phi(m_0,z,\tau)} \, \mathrm{d}z \right|. \tag{2.54}$$

Here, the steady-state voxel signal magnitude S_{SS} is assumed to be location-independent. The intra-voxel phase distribution Φ can depend on $m_0 = \int_0^{T_{\mathrm{E}}} G(t)\mathrm{d}t$, which is the induced gradient moment at T_{E} for a gradient $G(t)$ acting on local magnetization in z-direction, and a local additional phase offset τ. An intra-voxel phase distribution can hereby be introduced by local gradients in the main magnetic field (e.g., susceptibility-induced gradients in the proximity of metallic devices as described in Section 2.3 below) or by external gradients played out during the MR acquisition.

Spoiled fast low-angle shot

The FLASH pulse sequence was proposed to allow for rapid imaging with T_{R} shorter than the tissue's longitudinal relaxation time T_1 [57]. Due to the short T_{R}, magnetization cannot return to equilibrium between to RF pulses. Each RF pulse is therefore only able to flip the fraction of the magnetization into the transverse plane, that has already been restored to the longitudinal direction trough T_1 relaxation. Commonly, a so-called RF-spoiling mechanism is used with FLASH imaging to disrupt transverse coherences at the end of each T_{R}. Otherwise, the transverse component of the magnetization would also experience an excitation with the flip angle of the RF pulse and could contribute to the signal which is undesired as it would change the contrast. For effective spoiling, Zur et al. proposed to apply a quadratic RF phase cycling scheme [58], meaning the phase Φ_{RF} of each applied RF pulse is shifted by an angle $\Phi_{\mathrm{RF},j}$ which can be calculated using the recursive formula

$$\Phi_{\mathrm{RF},j} = \frac{\Phi_{\mathrm{RF},0}}{2}(j^2 + j + 2). \tag{2.55}$$

This shift in RF phase is combined with a spoiler gradient moment G_{spoil} dephasing the transverse magnetization at the end of T_{R} by $\frac{2\pi}{\mathrm{px}}$ for effective spoiling of the transverse magnetization.

After a transition phase of several T_R, a so-called incoherent steady-state magnetization is reached, with S_SSI, the steady-state signal magnitude per voxel, given by (see, e.g., Brown et al. [38])

$$S_\mathrm{SSI} \propto M_0 \frac{\sin(\mathrm{fa})\left(1 - e^{\left(-\frac{T_\mathrm{R}}{T_1}\right)}\right)}{1 - \cos(\mathrm{fa}) e^{\left(-\frac{T_\mathrm{R}}{T_1}\right)}}. \tag{2.56}$$

The FLASH signal magnitude is characterized by this steady-state magnetization and the T_2^* relaxation up to the echo time T_E. As can be seen from Eq. 2.56, the magnitude of the steady-state magnetization is dependent on the applied flip angle fa by the RF pulses. The optimal flip angle, allowing for maximum signal, is the so-called Ernst angle fa_E [59]. It can be calculated by maximizing Eq. 2.56 ($\frac{\partial S_\mathrm{SSI}}{\partial(\mathrm{fa})} \stackrel{!}{=} 0$), leading to

$$\mathrm{fa}_E = \arccos(e^{-T_\mathrm{R}/T_1}). \tag{2.57}$$

Applying a gradient moment m_0 up to T_E will introduce a phase Φ to the local magnetization. As the transverse magnetization is spoiled at the end of each T_R for a FLASH sequence, local phase at T_E will depend linear on the applied gradient moment up to T_E (ergo, not influenced by any phase evolution from previous T_R). Assuming a gradient moment m_0 acting in z-direction, causing a linear field variation, the phase of the local magentization can be calculated as

$$\Phi_\mathrm{spoiled}(z, m_0, \tau) = \gamma m_0 z + \tau, \tag{2.58}$$

with τ being a constant phase offset, characterizing the position of the evaluated local magnetization with respect to the resonance (i.e., characterizing the location z where $\Phi = 0$). Inserting Eq. 2.58 into Eq. 2.54, the integrated voxel signal magnitude for a FLASH sequence can be shown to be characterized by the well-known sinc function (cf., e.g., Bakker et al. [20]):

$$\begin{aligned} S_\mathrm{FLASH} &= S_\mathrm{SSI} \left| \int \mathrm{rect}\left(\frac{z}{\Delta z}\right) e^{-i(\gamma m_0 z)} \mathrm{d}z \right| \\ &= S_\mathrm{SSI} \left| \mathrm{sinc}\left(\frac{\gamma m_0 \Delta z}{2}\right) \right| \end{aligned} \tag{2.59}$$

Here, τ could be neglected for the integration as it is only a constant phase factor. The sinc function is maximized for $m_0 = 0$, i.e., a constant intra-voxel phase distribution.

In MR-guided interventions, the variation in magnetic susceptibility between metallic interventional devices and the adjacent tissue creates a local magnetic field gradient. This leads to dephasing of local magnetization, and therefore, according to Eq. 2.59, signal loss [9, 11], contributing to a characteristic device artifact, which is discussed in Section 2.3.2 for biopsy needles.

(Balanced) steady-state free precession

In comparison to RF-spoiled FLASH, no RF-spoiling is performed at the end of T_R for SSFP sequences and therefore, there is no disruption of transverse coherences [60, 61]. For short repetition times $T_\mathrm{R} \ll T_1$, the magnetization has not enough time to return to the equilibrium state and the RF puls at the start of T_R will act on the longitudinal as well as on the transversal component of the magnetization which is not yet fully relaxed from previous excitations. For a train of RF pulses, this characteristic will cause the magnetization to, after passing through a transient phase, approach a so-called coherent steady state with magnitude per voxel S_SSC and a characteristic local phase $\Phi_\mathrm{unspoiled}$ [62, 63].

To bring the magnetization close to the coherent steady state to start imaging without awaiting the passing of the transient phase, the magnetization can be prepared before the start of the image acquisition using different strategies (see [64]). A popular approach is the application of a (fa$/2$ - $T_\mathrm{R}/2$) preparation pulse, meaning an RF pulse is applying only half of the flip angle to the magnetization, followed by a waiting period of $T_\mathrm{R}/2$ before the first T_R of the actual image acquisition [65].

When the steady state is reached, magnitude $S_\mathrm{SSC}(\Theta)$ and phase $\Phi_\mathrm{unspoiled}(\Theta)$ of the signal at time T_E will depend on the net gradient moment acting on the magnetization during T_R, introducing a certain phase advance Θ to the local magnetization. In the following, we assume an induced net gradient moment of $2m_0$ to act across T_R. Depending on the placement of T_E in relation to the induced gradient moment, different contrast techniques can be distinguished [56]. Signal readout is commonly placed either after the RF pulse and before the introduction of the residual gradient moment $2m_0$, creating a so-called fast imaging with steady-state free precession (FISP) sequence. Alternatively, the signal readout can be placed after the introduction of $2m_0$, constituting a so-called time-reversed fast imaging with steady-state free precession (PSIF) sequence. The FISP and the PSIF sequence have some unique properties that render them useful for various imaging applications in the clinical routine (see, e.g., [66]), but are however not used in the context of this thesis which is why they will not be further discussed here. We instead investigate a readout placed in such a way that half of the induced residual gradient moment ($1m_0$) is induced before T_E and the other half ($1m_0$) is induced after T_E. The total phase advance of local magnetization at position x between two consecutive RF pulses is then given by $\Theta = 2(\gamma m_0 z + \tau)$. Here, τ is again a discrete phase offset, characterizing the position of the evaluated local magnetization with respect to the resonance. The signal magnitude is then given as [67, 68]

$$S_\mathrm{SSC}(\Theta) \propto \left| \frac{(1-E_1)(E_2 \sin \mathrm{fa} \sin\Theta) + i(1-E_1)((1-E_2\cos\Theta)\sin \mathrm{fa})}{D} \right|, \tag{2.60}$$

with $E_{1,2} = e^{\frac{-T_\mathrm{R}}{T_{1,2}}}$ and $D = (1-E_1\cos\alpha)(1-E_2\cos\Theta) - (E_1-\cos\alpha)(E_2-\cos\Theta)E_2$. Figure 2.1 shows the signal magnitude, depending on the local phase advance at T_E. The magnitude changes with the induced phase advance, becoming zero for multiples of $\Theta = 2\pi$.

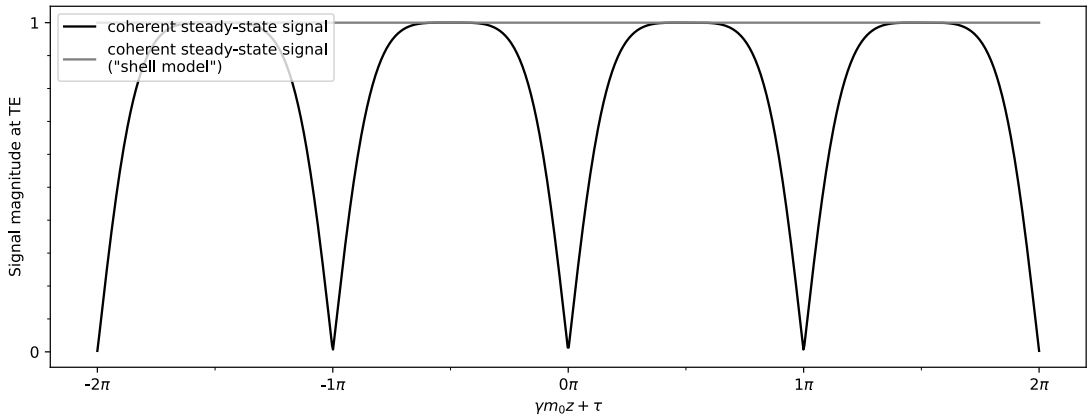

Figure 2.1: Magnitude of the coherent steady-state signal for an induced phase advance $\gamma m_0 z + \tau$ of the local magnetization at T_E (normed signal magnitude, example sequence parameters: $T_1 = 40T_\mathrm{R}, T_2 = 20T_\mathrm{R}, \mathrm{fa} = 70°$). In the context of the model introduced by Lebel et al. ("shell model" [69], used in this thesis), a constant signal magnitude is assumed.

Similar to the signal magnitude, the local phase depends on the induced phase advance Θ of the local magnetization between two T_R with

$$\Phi_\text{unspoiled}(\Theta) = \arg\left(\frac{(1-E_1)(E_2\sin(\mathrm{fa})\sin\Theta)+i(1-E_1)((1-E_2\cos\Theta)\sin(\mathrm{fa}))}{D}\right). \quad (2.61)$$

Figure 2.2 shows the signal phase at T_E, depending on the local phase advance. A gradient moment will induce a "flip" in phase where the induced phase advance at T_E locally surpasses multiples of π. If no external net magnetic gradient moment is applied throughout T_R to the local magnetization (can be achieved by balancing all applied gradient moments at the end of T_R with an additionally applied gradient moment of opposite polarity), no phase flips are introduced and the contrast is called balanced steady-state free precession (bSSFP). The resonance offset $2\tau = \pi$ is usually set to maximize the signal. Gradient moments that are balanced within a T_R are, similarly to spoiled gradient moments (see section on FLASH imaging above), not seen by the magnetization in subsequent T_R. A balanced gradient will therefore, similarly to spoiled gradients, induce a linear phase variation with m_0.

The relations Eq. 2.60 and Eq. 2.61 appear quite complex and can be impractical for use in derivations. Lebel et al. therefore proposed two simplifications to provide a simplified model of magnitude and phase of the SSFP signal: (i) to model the magnitude as constant and independent of the net gradient moment induced, and (ii) to model the phase as a simple square wave function:

$$\begin{aligned}\Phi_\text{spoiled or balanced}(z, m_0, \tau) &= \gamma m_0 z + \tau \\ \Phi_\text{unspoiled/unbalanced}(z, m_0, \tau) &= \mathrm{SW}(\gamma m_0 z + \tau) \\ &= \begin{cases}\pi \text{ for } (2k-1)\pi < \gamma m_0 z + \tau < 2k\pi \\ 0 \text{ for } 2k\pi < \gamma m_0 z + \tau < (2k+1)\pi,\end{cases}\end{aligned} \quad (2.62)$$

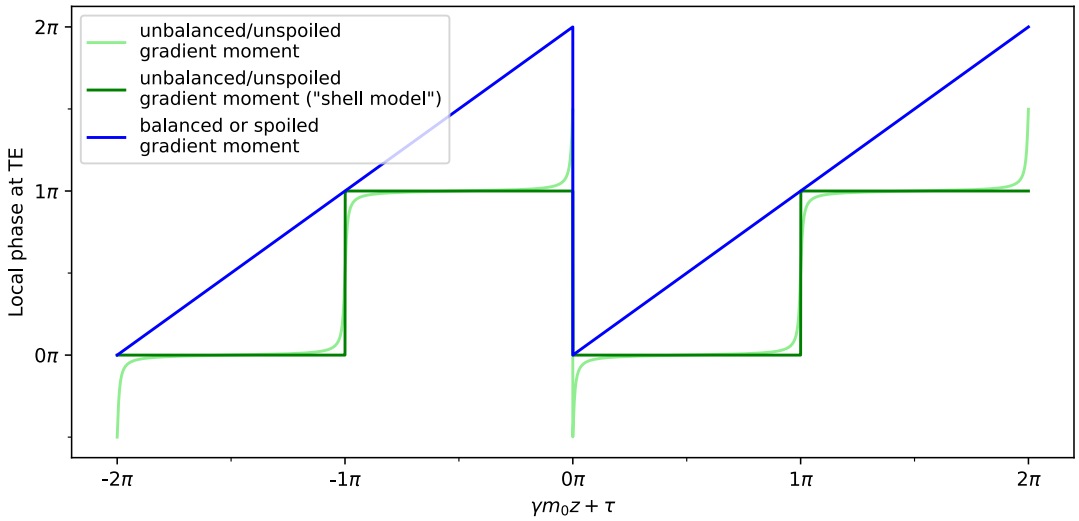

Figure 2.2: For a gradient moment m_0 acting on local magnetization along the z-direction at T_E, the phase of local magnetization at T_E varies depending on whether the acting gradient moment is spoiled or balanced, or unspoiled/unbalanced at the end of T_R. While the phase at T_E depends linearly on m_0 for a spoiled or balanced gradient moment, the dependence on m_0 for an unspoiled/unbalanced gradient moment is more complex and can be described by Eq. 2.61 (assuming a net induced gradient moment of $2m_0$ at the end of T_R; example sequence parameters: $T_1 = 40T_\mathrm{R}, T_2 = 20T_\mathrm{R}, \mathrm{fa} = 70°$). Lebel et al. modeled this dependency as a simple square wave as given in Eq. 2.62 ("shell model" [69]). Figure adapted from Faust et al. [2].

with $k \in \mathbb{Z}$. Lebel et al.'s model, which is termed "shell model", is additionally depicted in Fig. 2.1 and Fig. 2.2.

Near a metallic perturber, such as a biopsy needle, a local susceptibility-induced gradient (see Section 2.3) can cause phase flips which are spaced closer together for stronger gradient moments that usually appear closer to the device. This can form a local hypointense needle artifact, similar to FLASH imaging, in bSSFP images.

2.2.3 Susceptibility-based positive contrast imaging using dephased GRE

Artifacts introduced by metallic needles in conventional FLASH imaging, as described below in Section 2.3.2, are often characterized by signal voids in the proximity of the device due to susceptibility-induced dephasing. The device artifact can be used by the interventionalist to localize the needle in the image (see, e.g., Weiss et al. [5]). Signal voids in MR images can, however, have ambiguous origin (different tissue types, flow artifacts, non-tissue background etc.), and notable voids situated near devices can obstruct accurate device localization. Dephased MRI is a technique that exploits the inhomogeneity in the magnetic field caused by a metallic device to create increased signal intensities close to the interventional device and, therefore, allow for the visualization of metallic devices by the evocation of a hyperintense device artifact while suppressing the background signal further away from the device [20]. In dephased MRI, introducing an additional external gradient moment, prior to image readout, can counteract the gradient moment induced by the local susceptibility difference between the device and the surrounding material, thereby restoring phase coherence of the local magnetization and recovering signal. Meanwhile, this external gradient dephases signal further away from the device where the magnetic field remains largely unaffected by the susceptibility-induced inhomogeneity, thus diminishing the background signal and creating a hyperintense device artifact in the image. Seppenwoolde et al. achieved a positive device signal aritfact by shortening the slice-selection rephaser gradient in a FLASH sequence, deliberately creating a residual excess gradient moment in the slice-selection direction to locally balance a susceptibility-induced gradient moment [19]. The evoked emergence of a hyperintense device artifact was called the "WM phenomenon". Later, Bakker et al. extended the principle of introducing a global gradient dephasing, e.g. for device visualization by evoking the WM phenomenon, to general gradient directions (analogous to shifting the image reconstruction window of the acquisition k-space) and coined the term "dephased MRI" [20]. Dephased contrast imaging has been implemented for locating paramagnetic markers and interventional devices [19, 31]. A similar technique using gradient compensation has been applied to generate positive contrast for superparamagnetic iron oxides (SPIO)–labeled cells [70].

Generally, creating dephased contrast is achievable with GRE-type sequences, as in spin-echo sequences, susceptibility-induced dephasing is inherently counteracted (see Section 2.2.1). In the following, an additional gradient moment introduced into a GRE imaging sequence to generate dephased GRE will be termed a WM gradient moment, thereby reflecting on the work of Seppenwoolde et al. [19]. As listed in Section 2.2.2, GRE-type sequences generally include RF-spoiled GRE (commonly known as spoiled FLASH), SSFP, and bSSFP [56]. While Seppenwoolde et al.'s original work utilized dephased spoiled FLASH contrast [19], referred to

here as d-FLASH, Patil et al. introduced the "echo-dephased SSFP" method [21], which will be called dephased SSFP (d-SSFP) in the following. Dephased bSSFP (d-bSSFP) has also been used by various authors for visualizing interventional catheters and needles [25, 26]. Reiß et al. showed in preliminary experimental work that d-bSSFP contrast can provide a higher positive signal intensity compared to d-FLASH [27]. In the following, signal models for d-SSFP and d-bSSFP are introduced, characterized and compared to the well-known signal model for d-FLASH [20].

In their study, Seppenwoolde et al. explored the appearance of bright contrast near metallic devices following the application of an external gradient G_{WM} [19]. They attributed this effect, referred to as the WM phenomenon as mentioned earlier, to the compensation of local gradient moments. A susceptibility-induced magnetic field inhomogeneity near a metallic object can be described by a local magnetic field gradient G_{susc}. For small voxels, this gradient can be approximated as constant, which corresponds to a first-order Taylor approximation of the magnetic field distortion. Let $G_{\text{WM}}(t)$ and $G_{\text{susc}}(t)$ therefore be magnetic field gradients that generate linear field variations in z-direction (without loss of generality) and that act on local magnetization at time t during the repetition time T_{R}. At the echo time T_{E}, the gradients will have introduced a gradient moment $m_{0,\text{WM}} = \int_0^{T_{\text{E}}} G_{\text{WM}}(t)\text{d}t$ and $m_{0,\text{susc}} = \int_0^{T_{\text{E}}} G_{\text{susc}}(t)\text{d}t$, respectively. An external WM gradient moment is now assumed to introduce a phase $\gamma m_{0,\text{WM}} = \frac{2\pi}{\Delta z}$ to local magnetization at T_{E}. An underlying susceptibility-induced gradient moment $m_{0,\text{susc}}$ (assumed to similarly act in the z-direction) is considered to be applied to the local magnetization, simultaneously with the external WM gradient. Three cases can be distinguished:

1. Both the effects of $m_{0,\text{susc}}$ and $m_{0,\text{WM}}$ on the magentization are spoiled at the conclusion of T_{R} and induced intra-voxel phase is therefore described by the relation $\Phi_{\text{spoiled or balanced}}$ given in Eq. 2.62. This case corresponds to the contrast type of d-FLASH described by Seppenwoolde et al. and Bakker et al. [19, 20]. Due to the employed spoiling, the steady-state magnitude is described by S_{SSI}.

2. Both the effects of $m_{0,\text{susc}}$ and $m_{0,\text{WM}}$ on local magnetization remain unspoiled at the conclusion of T_{R} and the gradients are also not balanced. This case corresponds to the contrast type of d-SSFP described and simulated by Patil et al. [21]. To further evaluate this sequence type with a closed-form signal model, Lebel et al.'s magnitude and phase description (see above Eq. 2.62 [69]) was employed in this dissertation with the phase introduced by both gradients described by $\Phi_{\text{unspoiled/unbalanced}}$. As no spoiling is employed, the steady-state magnitude is described by S_{SSC} (assumed as constant by the terms of Lebel et al.'s model).

3. The effect of $m_{0,\text{susc}}$ on local magnetization is unspoiled/unbalanced while $m_{0,\text{WM}}$ is balanced at the conclusion of T_{R}. This case corresponds to the contrast type of d-bSSFP, which was employed in the past for device imaging [25, 26], but not yet thoroughly introduced or analyzed. The phase of the acting gradient moments is again proposed to be described by $\Phi_{\text{unspoiled/unbalanced}}$ and $\Phi_{\text{spoiled or balanced}}$ in Eq. 2.62, respectively. As no spoiling is employed, the steady-state magnitude is described by S_{SSC} (assumed as constant by the terms of Lebel et al.'s model).

Table 2.1: Type of the gradient moments $m_{0,\mathrm{WM}}$ and $m_{0,\mathrm{susc}}$ that act in superposition on local magnetization when applying the investigated dephased GRE techniques (d-FLASH, d-SSFP, and d-bSSFP) for positive susceptibility-based contrast imaging. Depending on the applied technique, gradient moments are either spoiled or balanced, or unspoiled/unbalanced, determining their influence on the phase of the local magnetization (cf. Eq. 2.62). Table reproduced from Faust et al. [2].

	Susceptibilty-induced gradient moment $m_{0,\mathrm{susc}}$	**White-Marker gradient moment $m_{0,WM}$**
d-FLASH	Spoiled	Spoiled
d-SSFP	Unspoiled/unbalanced	Unspoiled/unbalanced
d-bSSFP	Unspoiled/unbalanced	Balanced

Table 2.1 summarizes the types of acting gradient moments for the distinct contrast approaches. By incorporating the phase relationships from Eq. 2.62 into Eq. 2.54, the mean voxel signal amplitudes $\bar{S}_{\text{d-FLASH}}$, $\bar{S}_{\text{d-SSFP}}$, and $\bar{S}_{\text{d-bSSFP}}$ can be computed based on the gradient types:

$$\begin{aligned}
\bar{S}_{\text{d-FLASH}} &= S_{\text{SSI}} \left| \int \text{rect}\left(\frac{z}{\Delta z}\right) e^{-i(\gamma m_{0,\text{susc}} z + \frac{2\pi}{\Delta z} z)} \mathrm{d}z \right| \\
\bar{S}_{\text{d-SSFP}} &= S_{\text{SSC}} \frac{\int_0^{2\pi} \left| \int \text{rect}\left(\frac{z}{\Delta z}\right) e^{-i\,\text{SW}(\gamma m_{0,\text{susc}} z + \frac{2\pi}{\Delta z} z + \tau)} \mathrm{d}z \right| \mathrm{d}\tau}{2\pi} \\
\bar{S}_{\text{d-bSSFP}} &= S_{\text{SSC}} \frac{\int_0^{2\pi} \left| \int \text{rect}(\frac{z}{\Delta z}) e^{-i(\text{SW}(\gamma m_{0,\text{susc}} z + \tau) + \frac{2\pi}{\Delta z} z)} \mathrm{d}z \right| \mathrm{d}\tau}{2\pi}
\end{aligned} \tag{2.63}$$

In the case of d-FLASH, a discrete phase offset is not accounted for when integrating the signal across the voxel because it merely introduces a constant factor that does not alter the integrated signal's magnitude. However, for d-SSFP and d-bSSFP, it is essential to average over a discrete phase offset τ to determine the average signal magnitude. A closed-form solution for the signal equations (up to the initial signal maximum at $\gamma m_{0,\text{susc}} = \pm\frac{2\pi}{\Delta z}$ for $\bar{S}_{\text{d-bSSFP}}$) can be found in Appendix A.1 and is given by Eq. A.1. In Fig. 2.3, the voxel signal magnitudes are plotted for the three investigated contrast types ($\bar{S}_{\text{d-bSSFP}}$ is numerically continued for $|\gamma m_{0,\text{susc}}| > \frac{2\pi}{\Delta z}$). The solution for $\bar{S}_{\text{d-FLASH}}$ is the familiar sinc function, as was already described for d-FLASH by Bakker et al. [20]. The sinc fucntion appears shifted so that signal is maximzed for complete gradient compensation $\gamma m_{0,\text{WM}} = -\gamma m_{0,\text{susc}} = 2\pi\Delta z$. For $\bar{S}_{\text{d-SSFP}}$, the maximum signal occurs in a similar way for complete gradient compensation. In contrast to d-FLASH and d-SSFP, d-bSSFP exhibits two signal maxima instead of one. The signal is maximized at $\gamma m_{0,\text{WM}} = -\gamma m_{0,\text{susc}} = \frac{2\pi}{\Delta z}$ and also at $\gamma m_{0,\text{WM}} = +\gamma m_{0,\text{susc}} = \frac{2\pi}{\Delta z}$. While the full S_{SSI} and S_{SSC} signal magnitudes can be attained with d-FLASH and d-SSFP at maximum gradient compensation, approximately $64\,\%$ of the full S_{SSC} signal can be achieved with d-bSSFP, according to the model described in Eq. A.1. To better illustrate signal formation at these maxima, Fig. 2.4 depicts the intra-voxel phase for the two cases $\gamma m_{0,\text{WM}} = -\gamma m_{0,\text{susc}}$ and $\gamma m_{0,\text{WM}} = +\gamma m_{0,\text{susc}}$ for d-FLASH, d-SSFP, and d-bSSFP. For d-FLASH and d-SSFP, phase coherence is reestablished

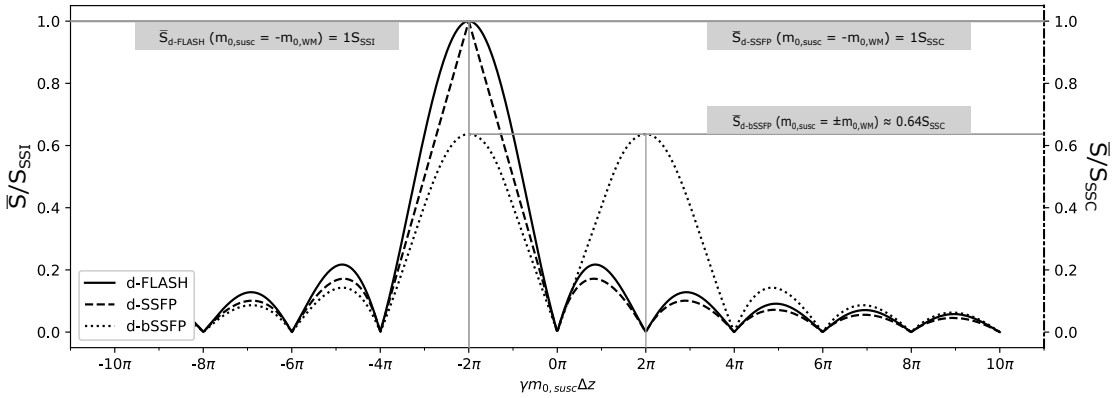

Figure 2.3: For d-FLASH, d-SSFP, and d-bSSFP contrast ($\gamma m_{0,\mathrm{WM}} = \frac{2\pi}{\Delta z}$), the average voxel signal magnitude Eq. 2.63 is plotted for a varying susceptibility-induced gradient moment $m_{0,\mathrm{susc}}$. For d-SSFP,d-bSSFP and d-FLASH the signal magnitude is normalized to the underlying coherent (S_{SSC}) or incoherent (S_{SSI}) steady-state signal magnitude, respectively. Figure adapted from Faust et al. [2].

only when $m_{0,\mathrm{susc}}$ and $m_{0,\mathrm{WM}}$ are of opposite polarities, whereas for d-bSSFP, limited phase coherence is reestablished regardless of the gradient polarities.

2.3 Delineation of needles in interventional MRI

A metallic biopsy needle itself does not invoke an MR signal as it does not contain resonant hydrogen nuclei, but can be delineated in the MR image as it can cause an image artifact, attributed to the needle's interaction with the main magnetic field $\vec{B}_0$. This distinctive artifact in the MR image can be employed for passive localization of the device, aiding the interventionalist in navigation [5, 7, 8, 12]. In the following, the interaction of the needle with $\vec{B}_0$ is described. The emerging needle image artifact is then discussed for GRE, more specifically FLASH imaging, as well as for dephased GRE imaging. Lastly, a theoretical motivation is given on how the effect of the needle on the MR signal can allow the encoding of the needle positional and orientational parameters in a subset of k-space, enabling the 3D localization of a needle from a limited, and therefore rapid, k-space acquisition as employed by the two needle localization methods investigated in this thesis.

2.3.1 Physical effect of a metallic needle on a magnetic field

Ladd et al. proposed to model a metallic biopsy needle as an infinite metallic cylinder that interacts with the main magnetic field of the MR scanner [9], which is described in the following.

Let the needle, without loss of generality, be oriented along y-direction in a right-handed coordinate system (schematically shown in Fig. 2.5). Let, furthermore, the needle enclose an angle

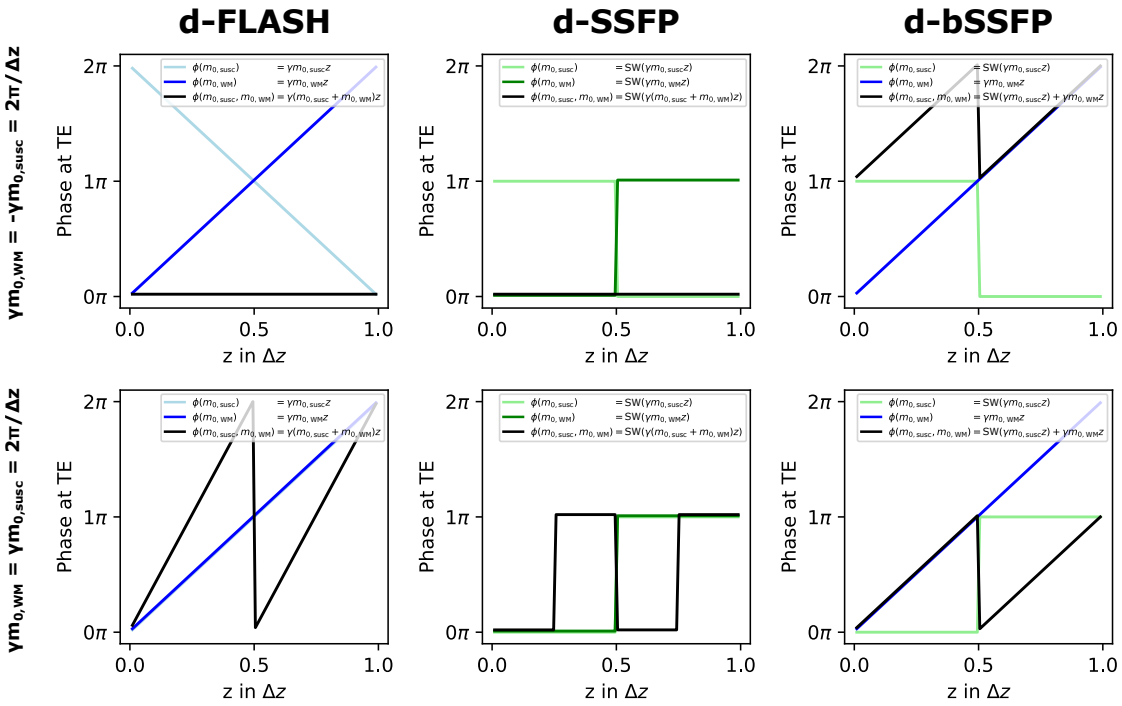

Figure 2.4: For d-FLASH, d-SSFP, and d-bSSFP, the intravoxel phase (voxel edge length Δz) of the local magnetization at T_{E} is analyzed for the two acting gradient moments $m_{0,\mathrm{susc}}$ and $m_{0,\mathrm{WM}}$. The two cases $\gamma m_{0,\mathrm{WM}} = -\gamma m_{0,\mathrm{susc}} = \frac{2\pi}{\Delta z}$ (expected signal maximum for d-FLASH, d-SSFP, and d-bSSFP) and $\gamma m_{0,\mathrm{WM}} = \gamma m_{0,\mathrm{susc}} = \frac{2\pi}{\Delta z}$ (expected additional signal maximum for d-bSSFP) are evaluated. Following Eq. 2.62, the intravoxel phase is plotted for $m_{0,\mathrm{susc}}$ and $m_{0,\mathrm{WM}}$ acting independently (for illustrative purposes) and both gradient moments acting in superposition (effective phase). Due to the gradients acting in superposition effectivly canceling each other out, magnetization across the voxel does not experience any resulting dephasing at $m_{0,\mathrm{susc}} = -m_{0,\mathrm{WM}}$ for d-FLASH and d-SSFP, while for $m_{0,\mathrm{susc}} = +m_{0,\mathrm{WM}}$, further dephasing of the signal is induced (no resulting signal magnitude). For d-bSSFP, intravoxel phase is partially rephased for $m_{0,\mathrm{susc}} = \pm m_{0,\mathrm{WM}}$. Lines are drawn with a slight offset for better visibility. Figure reproduced from Faust et al. [2].

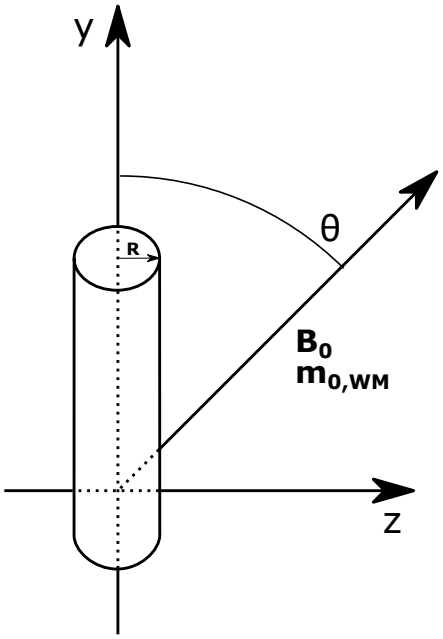

Figure 2.5: An needle (modeled as an infinite metallic cylinder) is placed in a right-handed coordinate system with the x-axis going into the image plane (not depicted for the sake of clarity). Figure adapted from Faust et al. [4].

θ with the field $\vec{B}_0 = (0, B_0 \cos\theta, B_0 \sin\theta)$. A metallic needle, characterized by the material's magnetic susceptibility $\chi_i = \mu_{\text{r,in}} - 1$ with $\mu_{\text{r,in}}$ being the relative permeability of the material, will cause a local change in the magnetic field. Modeling the needle as an infinite metallic cylinder and characterizing the outer material with $\chi_e = \mu_{\text{r,ext}} - 1$, the magnetic field inside the cylinder $\vec{B}_{\text{in}}$ and outside the cylinder $\vec{B}_{\text{ext}}$ can be calculated from the Laplace equation of magnetostatics ([10, 71]). For the two cases of the needle being oriented orthogonal or parallel to $\vec{B}_0$, the exterior field $\vec{B}_{\text{ext}}$ is given by

$$\begin{aligned}
\vec{B}_{\text{ext}}(\theta = 0^\circ) &= B_0\, \vec{e}_y \\
\vec{B}_{\text{ext}}(\theta = 90^\circ) &= B_0 \{ \vec{e}_z \left[1 + R^2 \left(\frac{\mu_{\text{r,ext}} - \mu_{\text{r,in}}}{\mu_{\text{r,ext}} + \mu_{\text{r,in}}} \right) \left(\frac{z^2 - x^2}{(z^2 + x^2)^2} \right) \right] \\
&\quad + \vec{e}_x \left[2R^2 \left(\frac{\mu_{\text{r,ext}} - \mu_{\text{r,in}}}{\mu_{\text{r,ext}} + \mu_{\text{r,in}}} \right) \left(\frac{zx}{(z^2 + x^2)^2} \right) \right] \}.
\end{aligned} \tag{2.64}$$

For the needle enclosing an arbitrary angle θ with the B_0 field, the field can be calculated as a superposition of the two cases in Eq. 2.64:

$$\begin{aligned}
\vec{B}_{\text{ext}}(\theta) &= \vec{B}_{\text{ext}}(\theta = 0^\circ) \cos\theta + \vec{B}_{\text{ext}}(\theta = 90^\circ) \sin\theta \\
&= B_0 \{ \vec{e}_z \left[1 + R^2 \left(\frac{\mu_{\text{r,ext}} - \mu_{\text{r,in}}}{\mu_{\text{r,ext}} + \mu_{\text{r,in}}} \right) \left(\frac{z^2 - x^2}{(z^2 + x^2)^2} \right) \right] \sin\theta \\
&\quad + \vec{e}_x \left[2R^2 \left(\frac{\mu_{\text{r,ext}} - \mu_{\text{r,in}}}{\mu_{\text{r,ext}} + \mu_{\text{r,in}}} \right) \left(\frac{zx}{(z^2 + x^2)^2} \right) \right] \sin\theta + \vec{e}_y \cos\theta \}.
\end{aligned} \tag{2.65}$$

From Eq. 2.65, the susceptibility-introduced change ΔB_{susc} of the magnetic field in the direction of the main magnetic field B_0 can now be calculated. Usually, materials with a susceptibility $|\chi_i| \ll 1$ are used for devices that find application in interventional MR. Here, the relation $\frac{\mu_{\text{r,ext}}-\mu_{\text{r,in}}}{\mu_{\text{r,ext}}+\mu_{\text{r,in}}} \simeq \frac{\chi_e-\chi_i}{2}$ usually holds and the change of the magnetic field is found as

$$\begin{aligned}\Delta B_{\text{susc}} &= B_0 - B_{\text{ext,z}} \sin\theta - B_{\text{ext,y}} \cos\theta \\ &= B_0 R^2 \left(\frac{\chi_e - \chi_i}{2}\right) \sin^2\theta \left(\frac{x^2 - y^2}{(x^2+y^2)^2}\right).\end{aligned} \tag{2.66}$$

2.3.2 MR image artifacts caused by a needle

A metallic needle can introduce an artifact in the MR image. Three separate effects can be observed that describe the influence of the needle on the MR signal (see, e.g., Ladd et al. [9]):

1. Hypointensity in the signal due to tissue displacement
2. Spatial shift artifact due to varying PRF near the needle
3. Dephasing artifact due to susceptibility-induced magnetic field gradient

The three effects determine together the visual representation of the needle artifact in the MR image and are discussed in the following paragraphs.

The needle itself will deplace the surrounding material, i.e. the tissue, along its path with consequently no signal being emitted from the location of the needle. This will lead to a hypointensity in the MR image, corresponding to the shape of the needle. This hypointensity is independent of the orientation of the needle to the $\vec{B}_0$ field.

Due to the susceptibility-introduced distortion of the magnetic field, the PRF varies in proximity of the needle. As described in Section 2.1.4, the MR signal is spatially encoded by modulating the PRF using external magnetic field gradients. For the frequency encoding direction, a modulation due to a susceptibility-induced field distortion can compromise the spatial encoding, leading to a spatial mismatch of the signal in the MR image. For a frequency encoding gradient $\vec{G}_{\text{FE}}$, the spatial shift of signal from position $\vec{x}$ to position $\vec{x}'$ can be calculated as (cf. [9, 10])

$$\vec{x}' = \vec{x} + \left(\frac{\Delta B_{\text{susc}}}{G_{\text{FE}}}\right)\left(\frac{\vec{G}_{\text{FE}}}{G_{\text{FE}}}\right) \tag{2.67}$$

Due to this spatial mismatch in signal, regions of signal pile-up and respective signal loss can appear in the image. Ladd et al. found that this effect would lead to a displacement of the apparent center of the needle as deduced from the artifact in relation to its physical center [9]. As the receiver bandwidth is directly proportional to the magnitude of the frequency encoding gradient moment (see Eq. 2.34), choosing a higher bandwidth for imaging can mitigate the spatial shift effect. For non-Cartesian, e.g., radial imaging, the direction of the readout, i.e., frequency encoding gradient, usually varies during the acquisition. Due to averaging effects, a varying readout direction rather leads to blurring of the artifact than to a discrete spatial shift [38].

A third effect characterizing the artifact of a needle can be attributed to a susceptibility-induced magnetic field gradient $\vec{G}_{\text{susc}} = \vec{\nabla}(\Delta B_{\text{susc}})$ in proximity of the device. At T_{E}, the gradient will have introduced a gradient moment $\vec{m}_{0,\text{susc}} = \int_0^{T_{\text{E}}} \vec{G}_{\text{susc}}\, \mathrm{d}t$. Calculating the derivative of Eq. 2.66, we find for $\vec{m}_{0,\text{susc}}$ (cf. [11])

$$\vec{m}_{0,\text{susc}} = T_{\text{E}} B_0 R^2 \left(\frac{\chi_e - \chi_i}{2}\right) \sin^2(\theta) \left(\frac{2x(-3z^2 + x^2)}{(z^2 + x^2)^3}\vec{e}_x + \frac{-2z(z^2 - 3x^2)}{(z^2 + x^2)^3}\vec{e}_y\right). \quad (2.68)$$

For GRE sequences, this gradient moment can induce an intra-voxel phase, changing the signal according to Eq. 2.54. Depending on the chosen imaging bandwidth and the thickness of the needle, the dephasing effect can become the dominant source of the artifact in GRE-based sequences and in this thesis, all investigations are based on the assumption, that the other two effects influencing the artifact are negligable. In the following, the dephasing artifact is further elucidated for GRE, more specifically FLASH, as well as for dephased GRE imaging.

FLASH imaging

In the following, a simple model is proposed and described, modeling the dephasing FLASH image artifact for a needle as a dephased disk in 2D or, respectively, a dephased cylinder in 3D. We assume a needle, modeled as an infinite cylinder according to Ladd et al. [9], oriented in a coordinate system as described above in Section 2.3.1 and as depicted in Fig. 2.5. Figure 2.6 shows the needle piercing the zx-plane and the orientation of the induced magnetic field gradient moment, given in Eq. 2.69. We now assume image voxels of isotropic size with edge length d_{voxel} and assume the susceptibility-induced gradient moment to always act along the voxel edge, ergo we neglect the orientation dependency of the gradient and proceed using its absolute value. From Eq. 2.68, we can calculate $|\vec{m}_{0,\text{susc}}|$ as

$$|\vec{m}_{0,\text{susc}}| = T_{\text{E}} B_0 R^2 (\chi_e - \chi_i) \sin^2\theta \sqrt{\frac{1}{(x^2 + z^2)^3}}. \quad (2.69)$$

From Eq. 2.69, it can be seen that $|\vec{m}_{0,\text{susc}}|$ is radially symmetric (concentric gradient magnitude isolines) and decreases with increasing distance $\sqrt{x^2 + z^2}$ to the needle. In terms of these model simplifications and plugging Eq. 2.69 into Eq. 2.59, the voxel signal magnitude can be expressed as

$$S_{\text{voxel}} = S_{\text{SSI}} \left| \operatorname{sinc}\left(\frac{\gamma |\vec{m}_{0,\text{susc}}| d_{\text{voxel}}}{2}\right) \right|. \quad (2.70)$$

To distinguish between voxels that are considered part of the needle artifact (with voxel signal magnitude S_{artifact}) and the background, determined by the steady-state signal S_{SSI}, we set a threshold of $S_{\text{artifact}} < 0.5\, S_{\text{SSI}}$. Using Eq. 2.70, we can calculate the radius $\sqrt{x^2 + z^2}$ of the gradient magnitude isoline, where the signal decreases below the set threshold. We numerically find $\gamma |\vec{m}_{0,\text{susc}}| \approx \frac{1.21\pi}{d_{\text{voxel}}}$ to solve $|S_{\text{voxel}}| = 0.5\, S_{\text{SSI}}$. Inserting the found value for $\vec{m}_{0,\text{susc}}$ in Eq. 2.69 and solving for $\sqrt{x^2 + z^2}$, we find for the radius of the artifact in zx-plane

$$r_{\text{FLASH}} = \sqrt[3]{\frac{\sin^2(\theta) T_{\text{E}} \gamma B_0 R^2 (\chi_e - \chi_i)\, d_{\text{voxel}}}{1.21\pi}}. \quad (2.71)$$

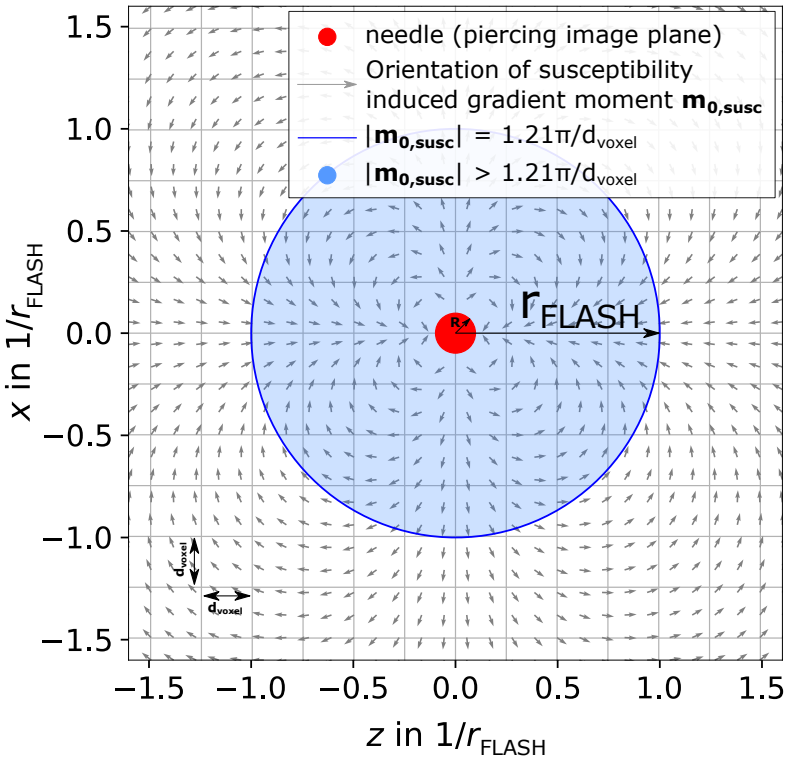

Figure 2.6: A metallic needle can introduce a local gradient moment $m_{0,\mathrm{susc}}$ at time T_{E} due to its susceptibility differing from the surrounding material. For a needle oriented along the y-direction in a right-handed coordinate system, the induced gradient field in the zx-plane is plotted with the gray arrows indicating the orientation of the local gradient moment. Within the blue disk (radius r as defined in Eq. 2.71), the gradient moment induces a dephasing of $\gamma m_0 > \frac{1.21\pi}{d_{\mathrm{voxel}}}$, corresponding to the voxel signal decreasing to $< 50\,\% S_{\mathrm{SSI}}$. Figure adapted from Faust et al. [72].

The model therefore predicts a circular hypointense dephasing needle artifact with the radius given in Eq. 2.71, which consequently constitutes a cylinder-shaped hypointense artifact in 3D, and is therefore refered to in this thesis as "dephased disk" or "dephased cylinder" model.

Dephased GRE imaging

To model the positive signal artifact for a needle imaged with dephased GRE, Ladd et al.'s infinite cylinder model was combined with the models for dephased GRE contrast from Section 2.2.3. The susceptibility-induced magnetic field gradient moment for a needle, induced locally at the time T_{E}, derived from Ladd et al.'s infinite cylinder needle model [9] was given in Eq. 2.68. Furthermore, a WM gradient moment is considered, acting on the local magnetization at T_{E} with

$$\vec{m}_{0,\mathrm{WM}} = m_{0,\mathrm{WM}} \cos(\theta)\vec{e}_y + m_{0,\mathrm{WM}} \sin(\theta)\vec{e}_z, \tag{2.72}$$

as also indicated in Fig. 2.5. As derived in Section 2.2.3, for a susceptibility-induced and WM gradient moment acting along the same axis of orientation, the maximum signal magnitude for both d-FLASH and d-SSFP contrast occurs when the susceptibility-induced and WM gradient moments are equal in magnitude but have opposite polarity. Furthermore, any component of $\vec{m}_{0,\mathrm{WM}}$ which cannot be counteracted by $\vec{m}_{0,\mathrm{susc}}$ will lead to a dephasing and, therefore, a decrease in signal. Consequently, for $m_{0,\mathrm{WM}}$ and $m_{0,\mathrm{susc}}$ as given in Eq. 2.72 and Eq. 2.68, the signal is maximized when $m_{0,\mathrm{susc},x} = 0$, because any susceptibility-induced gradient moment in the x-direction cannot be counterbalanced by Eq. 2.72, and when $m_{0,\mathrm{susc},z}$ is fully compensated by the WM gradient moment, ergo when $m_{0,\mathrm{susc},z} = -m_{0,\mathrm{WM},z}$. The y-component of $m_{0,\mathrm{WM}}$ causes a global dephasing that remains non-zero if the needle orientation includes a component parallel to B_0. For d-bSSFP contrast, maximum signal magnitude is additionally achieved when the susceptibility-induced and WM gradient moments are equal in magnitude and have the same polarity: $m_{0,\mathrm{susc},z} = m_{0,\mathrm{WM},z}$. Thus, the conditions for achieving maximum signal magnitude when imaging a needle with dephased GRE can be expressed by the following system of equations:

$$\begin{aligned} B_0 R^2 \frac{\chi_e - \chi_i}{2} \sin^2(\theta) T_{\mathrm{E}} \left(\frac{2x(-3z^2 + x^2)}{(z^2 + x^2)^3} \right) &= 0 \\ B_0 R^2 \frac{\chi_e - \chi_i}{2} \sin^2(\theta) T_{\mathrm{E}} \left(\frac{-2z(z^2 - 3x^2)}{(z^2 + x^2)^3} \right) \pm m_{0,\mathrm{WM}} \sin(\theta) &= 0 \end{aligned} \tag{2.73}$$

To determine the location of the expected signal maxima for a needle, Eq. 2.73 is now solved for a WM gradient induced phase of $\gamma m_{0,\mathrm{WM}} = \frac{2\pi}{\Delta z}$. While the condition $m_{0,\mathrm{susc},x} = 0$ holds for $z = 0x$ and $z = \pm\sqrt{3}x$, $|m_{0,\mathrm{susc}}| = m_{0,\mathrm{WM},z}$ is satisfied on a concentric circle within the zx-plane having the radius

$$r_{\text{d-GRE}} = \sqrt[3]{\frac{\sin^2(\theta) T_{\mathrm{E}} \gamma B_0 R^2 (\chi_e - \chi_i) \Delta z}{2\pi}}. \tag{2.74}$$

Combining the conditions $m_{0,\text{susc},x} = 0$ and $|m_{0,\text{susc}}| = m_{0,\text{WM},z}$, the positions of maximum signal in the zx-plane can hence be further calculated as

$$\begin{aligned}
\vec{x}_{1,2} = (z_{1,2}, x_{1,2}) &= \left(\pm \sqrt[3]{\frac{\sin(\theta) T_\text{E} \gamma B_0 R^2 (\chi_e - \chi_i) \Delta z}{2\pi}}, 0 \right) \\
\vec{x}_{3,4} = (z_{3,4}, x_{3,4}) &= (\pm \sqrt[3]{\frac{\sin(\theta) T_\text{E} \gamma B_0 R^2 (\chi_e - \chi_i) \Delta z}{16\pi}}, \\
&\qquad \sqrt{3} \sqrt[3]{\frac{\sin(\theta) T_\text{E} \gamma B_0 R^2 (\chi_e - \chi_i) \Delta z}{16\pi}}) \\
\vec{x}_{5,6} = (z_{5,6}, x_{5,6}) &= (\pm \sqrt[3]{\frac{\sin(\theta) T_\text{E} \gamma B_0 R^2 (\chi_e - \chi_i) \Delta z}{16\pi}}, \\
&\qquad - \sqrt{3} \sqrt[3]{\frac{\sin(\theta) T_\text{E} \gamma B_0 R^2 (\chi_e - \chi_i) \Delta z}{16\pi}}).
\end{aligned} \tag{2.75}$$

Figure 2.7 illustrates the local gradient field induced by a cylindrical needle within the zx-plane, overlaid with the WM gradient field. The x-component of the susceptibility-induced gradient moment becomes zero along the dashed black lines depicted in Fig. 2.7. On the solid black concentric line positioned at radius $r_{\text{d-GRE}}$, the magnitude of the susceptibility-induced gradient moment equals that of the WM gradient moment's z-component. Three intersection points ($\vec{x}_1$, $\vec{x}_4$, $\vec{x}_6$) are located where the susceptibility-induced gradient moment is opposite in polarity to the WM gradient moment, indicated by yellow triangles. At these intersections, maximum signal can be attained with d-FLASH, d-SSFP, and d-bSSFP. Additionally, three more points ($\vec{x}_2$, $\vec{x}_3$, $\vec{x}_5$) can be found where the gradient moments are characterized by the same magnitude and polarity, marked by yellow crosses. Here, additional signal maxima are anticipated in the zx-plane for d-bSSFP. Consequently, in a three-dimensional view, the WM needle artifact appears as either three or six stripes of hyperintense signal alongside the needle shaft.

Following the signal model introduced in Section 2.2.3, the anticipated ratio between the maximum signal magnitude for d-bSSFP and d-SSFP can be determined as approximately 0.64 (see Eq. A.1). As described by Eq. 2.75, the d-bSSFP needle artifact exhibits twice the number of voxels with maximum signal, resulting in a predicted cumulative signal magnitude ratio of about 1.27. Predicting either the maximum or cumulative signal magnitude ratio for d-FLASH in comparison to d-SSFP and d-bSSFP is not straightforward due to the formation of two distinct steady states, coherent steady state in the case of d-SSFP and d-bSSFP, and incoherent steady state for d-FLASH. The maximum signal magnitude for the incoherent state depends on T_1 and T_R (optimized at the Ernst angle), whereas, for the coherent steady-state, it is dependent on both T_1 and T_2 [73], rendering the signal intensity ratios between d-FLASH and d-SSFP, as well as between d-FLASH and d-bSSFP, dependent on tissue properties.

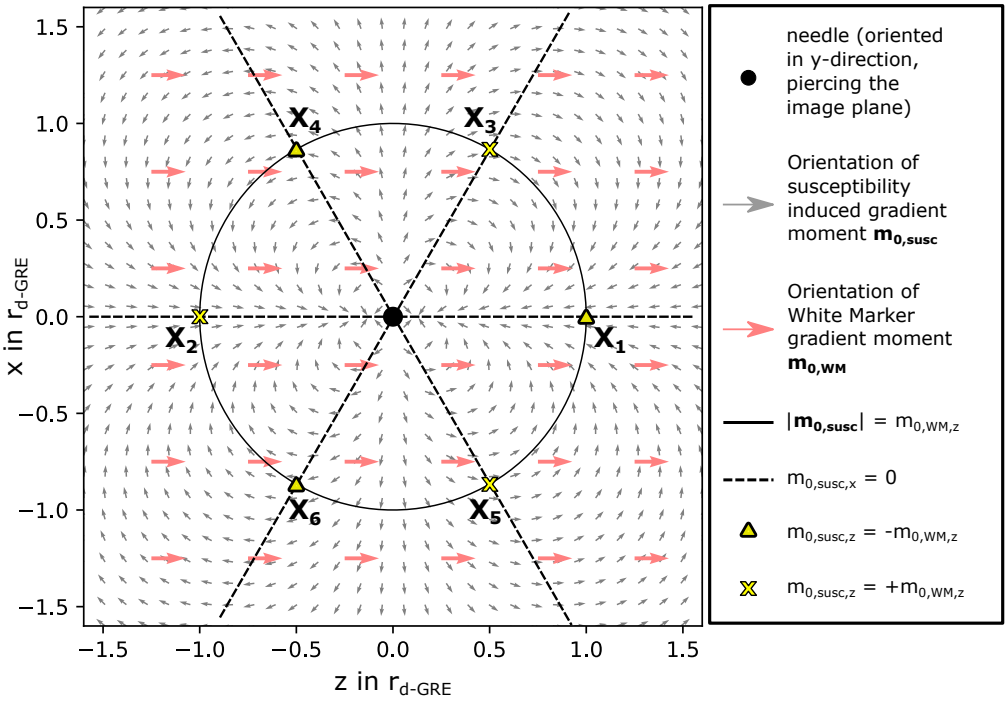

Figure 2.7: Similar to Fig. 2.6, the magnetic gradient field (zx-plane) induced by a needle (modeled as infinite metallic cylinder, orientation as defined in Fig. 2.5) is depicted schematically (gray arrows). Additionally, an overlying WM field gradient is indicated (red arrows). Three points (marked by yellow triangles) can be identified where $m_{0,\mathrm{susc,z}} = -m_{0,\mathrm{WM,z}}$. At these points, signal maxima are expected for d-FLASH, d-SSFP, and d-bSSFP. Three additional points (marked by yellow crosses) can be identified with $m_{0,\mathrm{susc,z}} = m_{0,\mathrm{WM,z}}$, where additional signal maxima are expected for d-bSSFP. Figure reproduced from Faust et al. [2].

2.3.3 Encoding of positional and orientational needle parameters in a subset of k-space

A needle, inserted into tissue, is characterized by only a limited number of degrees of freedom (insertion depth, angular orientation and insertion position, or, alternatively, entry and tip point coordinates). Due to this limited number of free parameters, it appears feasible to, for the sole purpose of localization, encode the positional and orientational information for the needle in a limited k-space acquisition, therefore without acquiring full k-space information necessary for a complete image reconstruction as described in Section 2.1.4. By extracting the needle position and orientation from only a subset of k-space can speed up the acquisition with the purpose of allowing for a rapid needle localization that can be integrated into real-time workflows.

In the past, several authors have investigated such a needle localization from only a limited number of acquired k-space lines. Kochavi et al. introduced a forward model-based needle localization method for the purpose of rapid 2D needle tip tracking [74]. For their technique, the authors acquired two sets of 2D k-space data with the needle being advanced in between. The subtraction k-space would then comprise a distinct signature of the advancing needle part, which, when transformed to image space, would closely resemble an isolated hyperintense rectangle: the isolated needle artifact of the advanced needle part with the background suppressed through the conducted subtraction. The authors then modeled the acquired subtraction k-space as a 2D sinc function, which corresponds to such an isolated rectangle if the modeled subtraction k-space was transformed to image space (the FT of a 1D sinc function correponds to a rect function, the 2D sinc function corresponds to a rectangle). By optimizing over the parameters of this 2D sinc function, the authors fitted the modeled subtraction k-space to the acquired subtraction k-space. They then mapped the 2D sinc function parameters, corresponding to the positional and orientational parameters characterizing the corresponding rectangle in image space, directly to the positional and orientational parameters of the needle artifact. Using the best fit parameters, feasibility of robust needle localization was shown in phantom experiments from an acquired subset of only six Cartesian central k-space lines. Schmidt et al. proposed a similar approach as Kochavi et al. for 3D needle tracking and evaluated the method in phantoms [15]. They acquired baseline subtracted k-space data (a few orthogonal k-space lines) for multiple parallel 2D slices. Instead of performing a model fit directly in k-space, they performed a 1D FFT on the acquired orthogonal k-space lines and fitted 1D rectangular functions to the Fourier-transformed k-space lines to determine the needle's progression through the acquired parallel slices. Their approach therefore allows for 3D localization of the needle path but requires acquisition of data for multiple slices and the prepositioning of the tracking slices. Reichert et al. investigated the localization of a passive marker attached to a needle outside the patient's body in undersampled 2D tracking slices. As the marker is positioned outside the body, it created an isolated artifact at the piercing point through the acquired 2D tracking slices. They localized the marker by matching the undersampled FLASH image to a template image of the marker. The 2D tracking image slices were herby reconstructed from only 4 radial k-space spokes. Zijlstra et al. acquired undersampled 2D d-FLASH images (inherent background suppression as described in Section 2.2.3) of needle insertions and localized the needle tip, also by matching a template to the acquired image [31].

All of the described methods aim to restrict the information encoded in acquired 2D k-space to the needle itself by suppressing the background, either by employing the subtraction of a baseline image when imaging the needle artifact, by acquiring images which only show a needle-attached marker outside the body or by employing d-FLASH imaging where the background is inherently suppressed. They then extract positional and orientational information on the needle from only a subset of k-space, which usually does not hold enough information for the reconstruction of an image with a resolution that would be sufficient for image guidance, but can hold sufficient information for needle localization. The acquisition of the limited k-space, as investigated by these methods, is therefore used solely to allow for a rapid localization of a needle that can be integrated in a real-time workflow.

The methods described above make use of one or multiple 2D image acquisitions for 2D or limited 3D needle localization using 2D tracking slices. If, in a real-time guidance workflow for a needle intervention, the needle is not visible in the 2D real-time images, a 3D localization can become necessary to automatically realign the 2D real-time images with the needle, as described in the introduction (Chapter 1). A 3D MRI acquisition for a 3D localization of the needle can hereby be particularly time-intensive and performing a full k-space acquisition for a 3D needle localization with the purpose of automatic real-time 2D slice alignment might not be practical for real-time workflows. In the following, an argument is proposed how the positional and orientational parameters of a needle could be encoded in a subset of a radial 3D k-space acquisition as described in Section 2.1.4. A prerequisite for this argument, as for the 2D methods described above, is that an image is acquired where the needle is characterized by an isolated artifact at the position of the needle, with no other information present in the image represented by the acquired k-space (therefore, some kind of image background suppression is required). We therefore assume a limited number of acquired radial k-space spokes with an employed image contrast so that, if an image were reconstructed, it would only show the needle artifact without any image background. Using the fundamental projection slice theorem, each acquired radial k-space spoke can be linked to a single 1D image projection of the imaged volume [75]. Let P_1 be a 1D projection through a 3D object $f(x, y, z)$, e.g. the isolated needle artifact in a background subtracted image). The Fourier-slice theorem then states that a radial spoke through the center of the 3D FT $\mathcal{F}_3$ of the object, characterized by the 1D slice operator S_1, corresponds to the 1D FT $\mathcal{F}_1$ of the 1D projection through the object, parallel to the slice:

$$\mathcal{F}_1\{\mathcal{P}_1\{f(x, y, z)\}\} = \mathcal{S}_1\{\mathcal{F}_3\{f(x, y, z)\}\}. \tag{2.76}$$

We can therefore represent a limited acquisition of k-space spokes as a set of 1D projections of the image volume. Figure 2.8 now schematically shows how a limited number of 1D projections of an isolated needle artifact could uniquely encode the positional and orientational information on the needle. Moving the needle inside the sampled volume will change at least one of the acquired 1D projections. This hence motivates the idea to localize a needle via a limited set of acquired k-space spokes.

In the course of this dissertation, two methods for 3D needle localization from an undersampled 3D k-space/image acquisition are investigated, that attempt a localization from only a limited number of 3D radial k-space spokes with employed image background suppression, as motivated

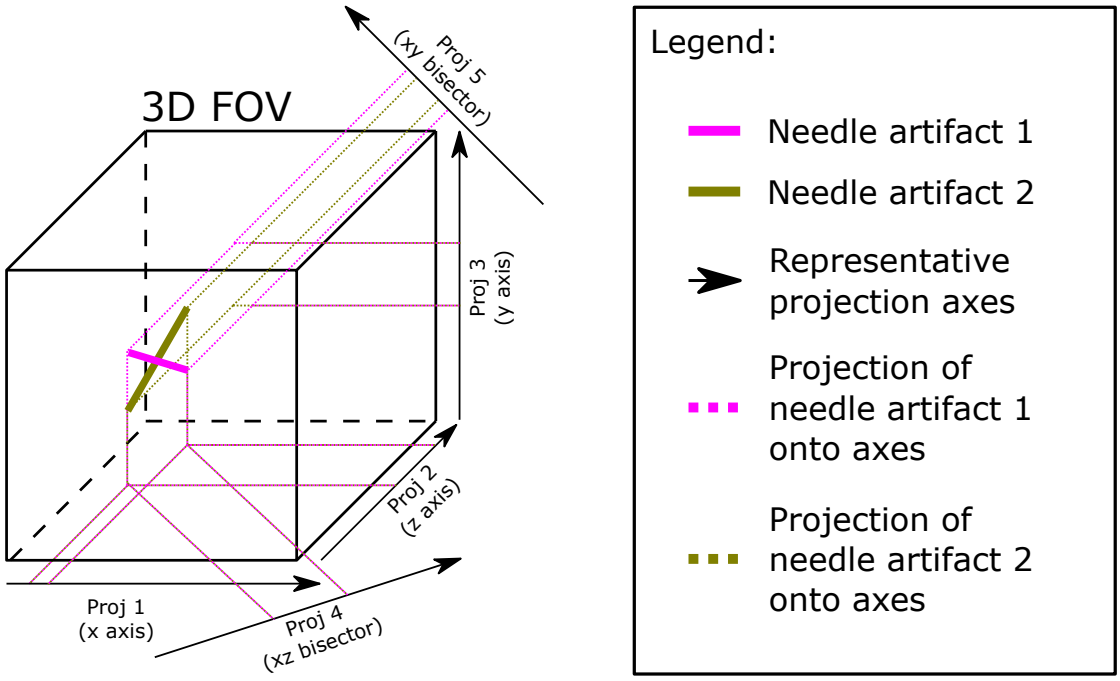

Figure 2.8: Each acquired radial k-space line corresponds to a 1D projection in image space (projection slice theorem). The schematic drawing shows two isolated needle artifacts (idealized as thin cylinder in 3D FOV) and their 1D projections onto five example projection axes. A change in artifact position, length, or orientation, e.g. transforming artifact 1 into artifact 2, will alter at least one projection. The needle's position and orientation are therefore uniquely encoded in a small subspace of k-space.

by Fig. 2.8. The first method (Section 3.2) employs modeling of a baseline-subtracted FLASH k-space acquisition, following Kochavi et al. (see above). The second investigated method employs a CNN-based localization approach, using d-FLASH to acquire images with intrinsic background suppression (Section 3.3).

3 Methods

After the characterization of the MR image artifact induced by a metallic needle for conventional (FLASH) and dephased GRE imaging (Section 3.1), two methods for rapid 3D passive needle localization were investigated. The first method used a baseline-subtracted FLASH k-space acquisition (Section 3.2) while the second method localizes the needle in d-FLASH images (Section 3.3).

3.1 Characterization of needle artifacts

The artifact induced by a needle was investigated for conventional GRE imaging (dephasing artifact), more specifically FLASH imaging (Section 3.1.1), as well as for imaging with dephased GRE contrast, comprising d-FLASH, d-SSFP and d-bSSFP (Section 3.1.2). Artifact magnitude, shape and size were characterized, using the respective signal models (see Section 2.3.2), and compared with acquired phantom images.

3.1.1 Needle artifacts in FLASH imaging

The dephasing artifact introduced by a biopsy needle for FLASH imaging was investigated. The artifact was compared with the model discussed in Section 2.3.2 for different sets of imaging parameters.

In Section 2.3.2, the needle artifact was defined as the image volume around the needle where the signal decreases below $50\,\%$ of the signal. The dephased volume was modeled as a dephased cylinder or, respectively, for an imaging plane orthogonal to the needle orientation, as a dephased disk where the radius of the disk depends on the material and imaging parameters used (Eq. 2.71). To evaluate how well this disk model can approximate the actual dephasing artifact induced by a needle in a FLASH image, images of a needle inside a water phantom, shown in Fig. 3.1, were acquired. The artifact was investigated for a 20-gauge (R = $0.040\,59\,\mathrm{cm}$) needle (Cook Medical, Bloomington, IN, USA), made of Inconel ($\chi_i = 568 \times 10^{-6}$ [76]) and placed in a water phantom ($\chi_e = -9.05e-6$ [77]), at three different field strengths $B_{0,1} = 0.55\,\mathrm{T}$, $B_{0,2} = 1.5\,\mathrm{T}$ and $B_{0,3} = 3\,\mathrm{T}$ (MAGNETOM Free.Max, MAGNETOM Sola, MAGNETOM Vida; Siemens Healthineers AG, Erlangen, Germany). The needle was inserted into the phantom at an inclination angle of $\theta = 90°$ to $\vec{B}_0$, as defined in Fig. 2.5. For each field strength, images were acquired with a conventional FLASH pulse sequence employing a Cartesian readout scheme (see Section 2.2.2 and Section 2.1.4), at three different echo times $T_{\mathrm{E},1} = 5\,\mathrm{ms}, T_{\mathrm{E},2} = 15\,\mathrm{ms}$ and $T_{\mathrm{E},3} = 25\,\mathrm{ms}$

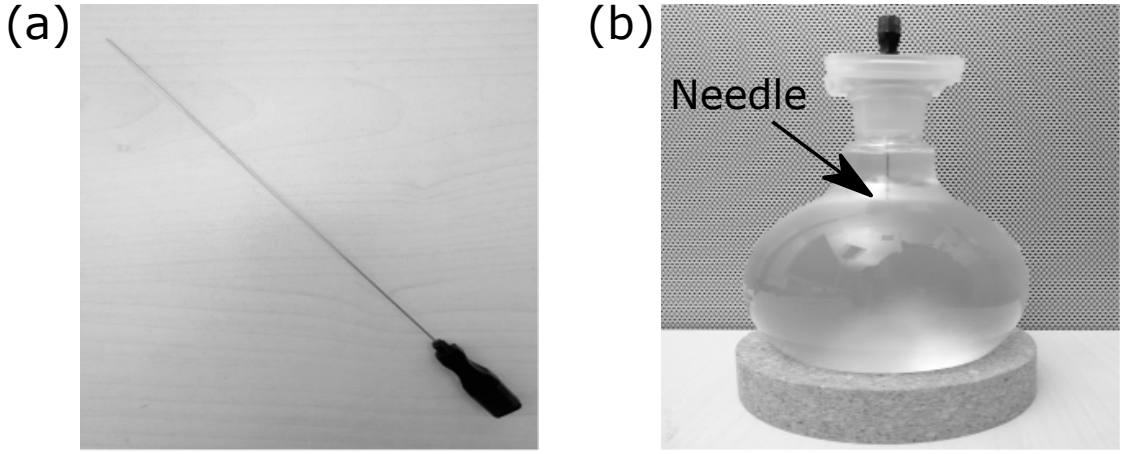

Figure 3.1: A 20-gauge (R = 0.040 59 cm) needle (Cook Medical, Bloomington, IN, USA), made of Inconel ($\chi_i = 568 \times 10^{-6}$ [76]) and shown in (a), was placed in a water phantom ($\chi_e = -9.05e - 6$ [77]) as shown in (b). Figure adapted from Faust et al. [4].

with two investigated image resolutions $\text{res}_1 = (1\,\text{mm})^3$ and $\text{res}_2 = (2\,\text{mm})^3$. Furthermore, the following set of imaging parameters was used: $T_\text{R} = 30\,\text{ms}$, fa $= 10°$, FOV $= (128\,\text{mm})^3$, bw $= 260\,\text{Hz}\,\text{px}^{-1}$. To limit this investigation of the FLASH needle artifact to dephasing effects only, and suppress any potential spatial mismatch due to the locally altered PRF in proximity of the needle according to Eq. 2.67, the frequency-encoding gradient direction was chosen parallel to the needle shaft as the magnetic field distortion only extends orthogonally to the needle shaft (Eq. 2.66). Additional to the FLASH images, reference images with SE contrast were acquired (res $= (1\,\text{mm})^3$, FOV $= (128\,\text{mm})^3$, bw $= 501\,\text{Hz}\,\text{px}^{-1}$, $T_\text{R} = 3000\,\text{ms}$, $T_\text{E} = 150\,\text{ms}$).

Two metrics were used for comparison of the measured artifact and the dephased disk model to assess the accuracy with which the model can describe the measured artifact. The Dice similarity coefficient DSC and the Hausdorff distance d_H were calculated for the measured and modeled artifact and compared for all measurements. While the DSC (defined as the number of overlapping voxels as a fraction of the average number of voxels of the measured and modeled artifact) can serve as a measure to assess the general resemblance of the model and the measured artifact, the Hausdorff distance can be interpreted as deviation of the radius of the modeled and the measured artifact (assuming the measured artifact to be approximately disk-shaped, otherwise the radius could not be defined), as it is defined as the largest of all distances between the center of a voxel of the measured to the center of the respectively closest voxel of the modeled artifact. For the evaluation of the metrics, a background and an artifact region of interest (ROI) were defined for 2D images, orthogonal to the needle orientation, in a slab of 10 slices, containing the needle inserted into the water phantom. The background signal magnitude was calculated by averaging over the background ROI (with size $(15\,\text{px})^2$ and $(7\,\text{px})^2$ for res_1 and res_2, respectively) and the artifact area was determined by masking the artifact ROI for pixels with a signal magnitude larger than $50\,\%$ of the background signal. The disk-shaped artifact model was centered at the position of the needle shaft as extracted from the spin-echo reference images for the center slice of the

evaluated slab and compared to the measured artifact, using the mentioned metrics. Average values for the two metrics and standard deviation across the evaluated 10 slices were calculated for each set of parameters described above.

3.1.2 Needle artifacts in dephased GRE imaging

The artifact of a biopsy needle was investigated for the three dephased GRE contrast types d-FLASH, d-SSFP and d-bSSFP (as were described in Section 2.2.3). For that purpose, three different research MR pulse sequences were implemented and images of a needle in a water phantom were acquired. Results were compared with the theoretically predicted artifacts (see Section 2.3.2), using the sinc model [20] for d-FLASH contrast and the introduced models for d-SSFP and d-bSSFP.

MR pulse sequence implementation

Three research MR pulse sequences were implemented (IDEA MR pulse sequence programming framework; Siemens Healthineers AG, Erlangen, Germany) for 3D imaging with d-FLASH, d-SSFP and d-bSSFP contrast (Fig. 3.2b–d).

To alleviate potential spatial misregistration of the signal near a metallic needle resulting from spatial frequency mismatches caused by altered PRF as described in Section 2.3.2 (and also in preparation for a use of the implemented d-FLASH sequence as part of the localization method presented in Section 3.3), a radial k-space trajectory (see Section 2.1.4) was selected for the image acquisition (Fig. 3.2a). As a result of the varying frequency encoding direction of the collected k-space spokes for the chosen 3D sampling scheme, a spatial frequency mismatch will result in blurring instead of causing distinct spatial shifts of signal in the image [38]. To radially sample k-space, the angular orientation of each acquired k-space spoke was varied by advancing the inclination and azimuthal angles of each spoke (see Eq. 2.47) with the so-called golden means [80]:

$$\begin{aligned} \phi_k &= \arccos(0.4656n) \\ \theta_k &= 2\pi(0.6823n). \end{aligned} \tag{3.1}$$

Here, n is the number of the sampled radial k-space spoke with $n = 0 \cdots n_{\text{spokes}}$, with n_{spokes} being the total number of sampled spokes. The golden means sampling scheme, related to the "golden angle" in 1D, allows an approximately uniform distribution of consecutively sampled spokes in radially-sampled 3D k-space. As Eq. 3.1 only encompasses angles from one hemisphere, every second k-space spokes was sampled backwards to guarantee a uniform distribution of the frequency encoding direction.

To generate d-FLASH contrast (Fig. 3.2b), the spoiling mechanism proposed by Zur et al. [58] was implemented (see Section 2.2.2). A spoiler gradient is applied in the x-direction before the end of T_{R} (orthogonal to the WM gradient direction, as the assumption of effective spoiling is only valid if the magnetization is not affected by any dephaser gradients at the readout [78]), resulting

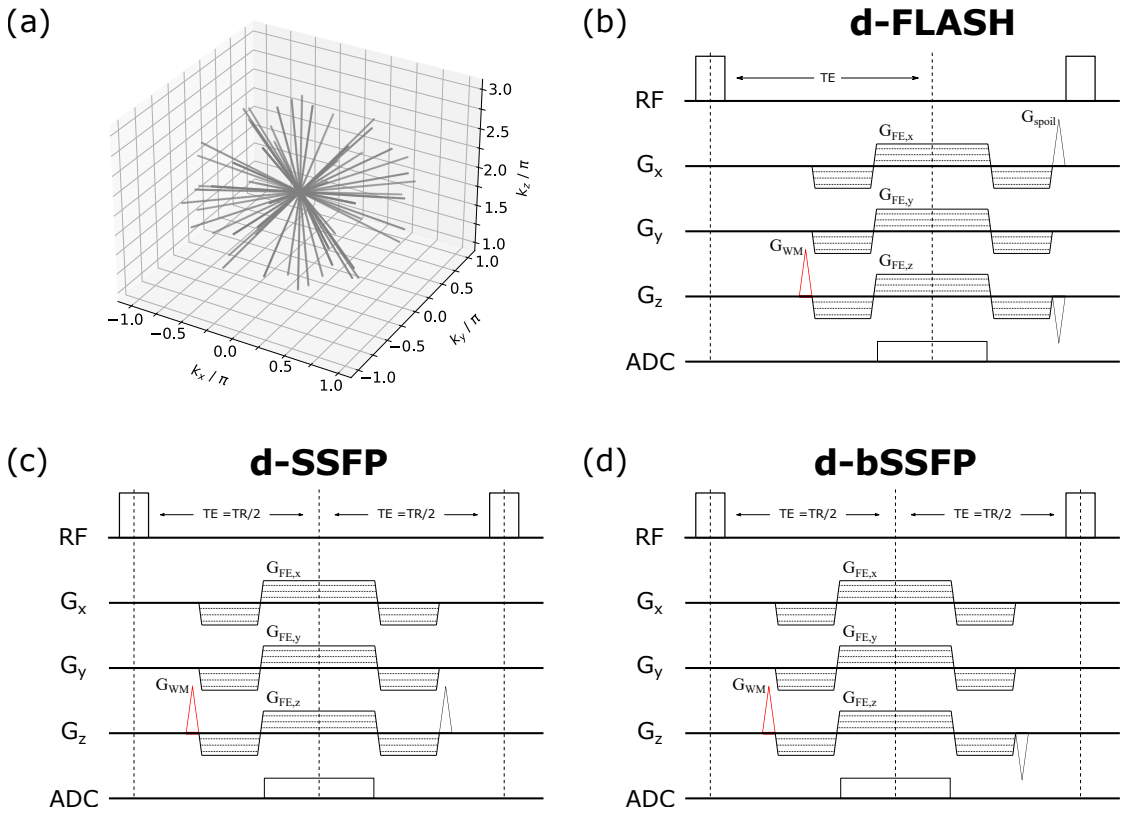

Figure 3.2: Three MR pulse sequences diagrams of the sequences that were implemented for image acquisitions with d-FLASH (b), d-SSFP (c), and d-bSSFP (d) contrast. The implemented sequences allow for the sampling of k-space along a 3D radial trajectory (a). The components $\vec{G}_{\mathrm{FE}x}$, $\vec{G}_{\mathrm{FE}y}$ and $\vec{G}_{\mathrm{FE}z}$ of the readout gradient $\vec{G}_{\mathrm{FE}}$ applied along the different orientational axes vary with the direction of the sampled k-space spokes. A WM gradient moment (depicted in red) with $\gamma m_{0,\mathrm{WM}} = \frac{2\pi}{\Delta z}$ is implemented for all three sequence types, which can be interpreted as an introduced global shift of the acquisition k-space (a) in z-direction by 2π. For d-FLASH, RF-spoiling is implemented (requires an additional spoiler gradient implemented in x-direction and reverting of all other gradient moments [78, 79]). For d-SSFP, a total gradient moment of $2m_{0,\mathrm{WM}}$ must be played out before the end of T_{R} with $T_{\mathrm{E}} = \frac{T_{\mathrm{R}}}{2}$ [21]. To generate d-bSSFP, all gradients must be balanced at the end of each T_{R}, again with $T_{\mathrm{E}} = \frac{T_{\mathrm{R}}}{2}$. Figure adapted from [2].

in a dephasing of the magnetization with an induced phase of 2π per voxel. Additionally, a quadratic RF phase cycling was implemented. In order to guarantee effective spoiling by applying the same spoiler gradient moment (concerning magnitude and orientation) to the magnetization at the end of each T_{R}, the readout gradient is reverted at the end of each T_{R} as its direction changes with each acquired spoke [79]. A WM gradient moment was implemented in the sequence before the readout (shown in red), causing a shift in the acquired k-space along the z-direction with an induced dephasing of $\gamma m_{0,\mathrm{WM}} = \frac{2\pi}{\Delta z}$.

For the generation of d-SSFP contrast (Fig. 3.2c), no spoiling of the transverse magnetization is employed at the end of T_{R}. Again, a WM gradient moment with $m_{0,\mathrm{WM}} = \frac{2\pi}{\Delta z}$ is employed before the readout. Following Patil et al. [21], an additional gradient moment, equivalent to the WM gradient moment, is implemented after T_{E}. This results in a net external gradient moment of $2m_{0,\mathrm{WM}}$ by the conclusion of T_{R}. Moreover, T_{E} is set to $T_{\mathrm{E}} = \frac{T_{\mathrm{R}}}{2}$ so that a resultant susceptibility-induced gradient moment of $2m_{0,\mathrm{susc}}$ occurs during T_{R}, ensuring that Eq. 2.62 is applicable (see Section 2.2.3). To allow for a quick transition of the magnetization to coherent steady state, an (fa$/2$ - $T_{\mathrm{R}}/2$) preparation pulse [65] was implemented before the start of the acquisition (see Section 2.2.2).

To generate d-bSSFP contrast, again no spoiling is employed. At the conclusion of T_{R}, all gradient moments are balanced, including the WM gradient, with T_{E} remaining again set as $T_{\mathrm{E}} = \frac{T_{\mathrm{R}}}{2}$. When this sequence is applied, only the external gradient moments, meaning the gradients applied by the sequence, acting on the local magnetization are balanced. A locally varying suscepibtility-induced gradient moment will remain unbalanced as described in Section 2.2.3. Again, a (fa$/2$ - $T_{\mathrm{R}}/2$) preparation pulse [65] was added.

For the implemented sequences, an offline image reconstruction pipeline was built, employing a NUFFT (see Section 2.1.4). The reconstruction was implemented in Python using the SigPy package [81].

Artifact shape, signal and radius measurements

To evaluate the proposed models for d-SSFP and d-bSSFP, as well as the well-established sinc model for d-FLASH [20], and assess the positive contrast formation for a needle imaged with the three investigated dephased GRE techniques, a 20-gauge ($R = 0.040\,59\,\mathrm{cm}$) MR-compatible aspiration needle (Cook Medical, Bloomington, IN, USA) composed of Inconel ($\chi_i = 568 \times 10^{-6}$ [76]) was positioned in a flask phantom filled with deionized water ($\chi_e = -9.05 \times 10^{-6}$ [77]), i.e., the same phantom, depicted in Fig. 3.1, as used for the investigation of FLASH needle artifacts described in Section 3.1.1. The needle was positioned at an angle of $\theta = 90°$ relative to $\vec{B}_0$ as defined in Fig. 2.5.

Images with d-FLASH, d-SSFP, and d-bSSFP contrast were acquired with the implemented sequences (see previous section). The phantom was imaged at $B_0 = 0.55\,\mathrm{T}$ (MAGNETOM Free.Max; Siemens Healthineers, Erlangen, Germany) with a 12-channel head coil (data from 4 channels used for image reconstruction). The chosen sequence parameters were: FOV $=$

$(128\,\mathrm{mm})^3$; res $= (2\,\mathrm{mm})^3$; $T_\mathrm{R} = 40\,\mathrm{ms}$; $T_\mathrm{E} = 20\,\mathrm{ms}$, bw $= 900\,\mathrm{Hz\,px^{-1}}$, fa $= 70°$ (d-SSFP, d-bSSFP) / $10°$ (d-FLASH, optimized for the Ernst angle with a parameter sweep of $2°$ increments). Additionally, a reference image of the needle phantom was obtained using an SE sequence with chosen parameters: FOV $= (128\,\mathrm{mm})^3$; res $= (1\,\mathrm{mm})^3$; $T_\mathrm{E} = 152\,\mathrm{ms}$; $T_\mathrm{R} = 3000\,\mathrm{ms}$; bw $= 501\,\mathrm{Hz\,px^{-1}}$.

For a needle (modeled as an infinite metallic cylinder [9]) imaged with dephased GRE, the models for the three investigated contrast techniques predict either 3 (for d-FLASH and d-SSFP) or 6 signal maxima in the respective zx-plane as defined in Fig. 2.5 (see Section 2.3.2). The maximum artifact signal magnitude for the needle in the water phantom (averaged for the 3 or 6 points of maximum artifact signal in the zx-plane over a slab of 10 image slices) was evaluated for the different contrast methods and the ratio between the d-bSSFP and the d-SSFP maximum artifact signal was compared to the theoretically expected value (see Section 2.3.2). Moreover, the cumulative artifact signal magnitude (the summed magnitude of the 3 or 6 points of maximum artifact signal in the zx-plane, averaged over 10 slices) for the d-SSFP and the d-bSSFP needle artifact was likewise compared with the expected theoretical ratio. To further assess model precision, d-bSSFP contrast images were acquired with different T_E times ($T_{\mathrm{E},1} = 3.4\,\mathrm{ms}$, $T_{\mathrm{E},2} = 10\,\mathrm{ms}$, $T_{\mathrm{E},3} = 20\,\mathrm{ms}$, $T_{\mathrm{E},4} = 30\,\mathrm{ms}$, $T_{\mathrm{E},5} = 40\,\mathrm{ms}$, $T_{\mathrm{E},6} = 50\,\mathrm{ms}$; $T_{\mathrm{E},1}$ was the minimum possible echo time, other imaging parameters were chosen as given above). The artifact radius (distance between needle axis and signal maxima) was measured for the images acquired at the different T_E by averaging the distance between the needle shaft position (determined from the spin-echo reference) to the position of pixels with maximum signal magnitude (distances were measured between pixel centers; a measurement accuracy of $\pm 1\,\mathrm{mm}$ was assumed, corresponding to half of the resolution). The measured artifact radius was then compared to the theoretically predicted artifact radius (Eq. 2.74) to evaluate model precision. Furthermore, Eq. 2.74 was fitted, in an additional step, to the measured radius values for the different T_E (Levenberg-Marquardt algorithm, using SciPy [82]), choosing the needle's susceptibility χ_i as the free parameter over which the algorithm performed the optimization.

3.2 Forward model-based 3D needle localization using a baseline-subtracted FLASH acquisition

A technique for rapid 3D needle localization from a baseline-subtracted radial k-space acquisition was introduced and the technique was evaluated in an ex-vivo phantom study. Feasibility of ASP, using the investigated localization technique, was retrospectively demonstrated for a sample from the ex-vivo dataset, as well as for an in-vivo proof-of-principle needle insertion.

3.2.1 Technique for needle localization

The investigated needle localization technique operates on subtraction datasets obtained from radially sampled FLASH k-space acquisitions before and after a needle insertion. The subtraction k-space contains a distinct signature of the needle. By fitting a model to the subtraction k-space,

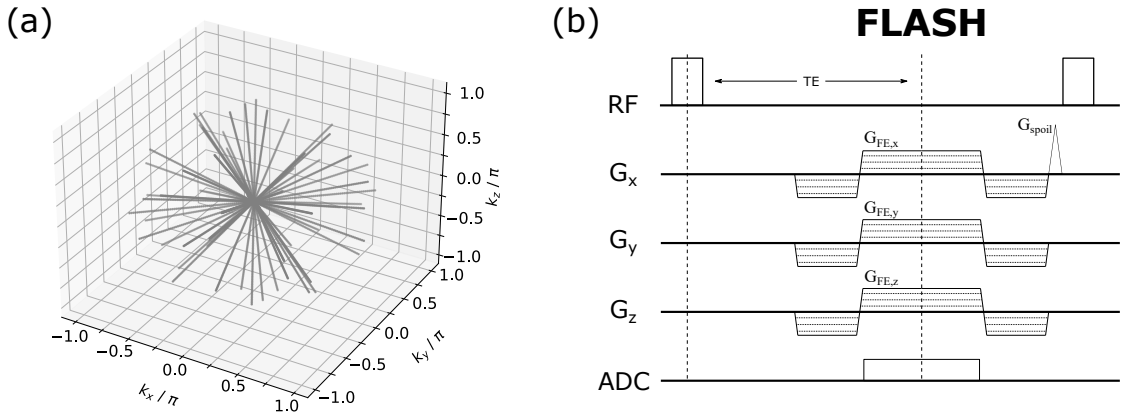

Figure 3.3: (a) Sampled k-space trajectory (30 example spokes) of implemented FLASH sequence, following a golden means sampling scheme [32]. (b) Pulse sequence diagram for implemented FLASH sequence. The components $\vec{G}_{\mathrm{FE}x}$, $\vec{G}_{\mathrm{FE}y}$ and $\vec{G}_{\mathrm{FE}z}$ of the readout gradient $\vec{G}_{\mathrm{FE}}$ applied along the different orientational axes vary with the direction of the sampled k-space spokes. At the end of T_{R}, a spoiler gradient $\vec{G}_{\mathrm{spoil}}$ (always applied in the same direction, after balancing of the readout, for effective spoiling [79]) introduces a phase of $\frac{2\pi}{\mathrm{px}}$ along the x-axis (+ implemented RF spoiling [58]).

orientational and positional parameters of the needle are determined which can then be used for ASP of a 2D real-time imaging slice.

Radial FLASH acquisition

For data acquisition, a 3D FLASH pulse sequence (Fig. 3.3b) was implemented (IDEA MR pulse sequence programming framework; Siemens Healthineers AG, Erlangen, Germany). A radial golden means k-space trajectory was chosen (Fig. 3.3a, compare implementation of dephased GRE sequences described in Section 3.1.2) to allow for retrospective cropping of the acquired data to an arbitrary number of k-space lines, while simultaneously allowing for a uniform distribution of the acquired set of spokes in 3D k-space [80]. For the proposed needle localization technique, two data acquisitions were performed: one baseline acquisition before the needle insertion and one acquisition after the (partial) insertion of the needle. From the two acquisitions, the subtraction k-space was calculated and processed by the needle localization algorithm. The following sequence parameters were used for all acquisitions: FOV $= (256\,\mathrm{mm})^3$; res $= (4\,\mathrm{mm})^3$; $T_{\mathrm{R}} = 15\,\mathrm{ms}$; $T_{\mathrm{E}} = 10\,\mathrm{ms}$; fa $= 10°$; bw $= 160\,\mathrm{Hz\,px^{-1}}$.

Needle model

As described in Section 2.3, a metallic needle can introduce an inhomogeneity of the magnetic field B_0 in its surrounding, establishing a local magnetic field gradient. For FLASH imaging, this gradient can induce a loss of local phase coherence, leading to a hypointense image artifact near

the needle. Approximating the needle as an (infinite) metallic cylinder [9], the FLASH needle artifact was modeled as a dephased disk in 2D images, consequently forming a dephased cylinder in 3D (see Section 2.3.2). In other words, the region where signal magnitude decreases below a certain threshold compared to the signal in the magnetically undisturbed background is cylindrical, leading to a cylindrical hypointense image artifact (according to the model, neglecting the artifact region near the needle tip) in an acquired 3D image, with the axis of the artifact coinciding with the axis of the needle. Therefore, a baseline-subtracted image of a needle inserted into tissue or a phantom, reconstructed from a baseline-subtracted k-space acquisition, would be expected to show a hyperintense cylindrical artifact on an otherwise suppressed background, assuming the background signal remains the same before and after the needle insertion and is nullified by the subtraction. The acquired subtraction k-space itself, similar to the reconstructed subtraction image, would equally be characterized by a distinct signature, which would correspond to the hyperintense cylinder artifact expected for the reconstructed subtraction image space.

The 3D subtraction k-space of a needle insertion was modeled with an analytic function with the parameters of the function corresponding to the needle's positional and orientational parameters. For that purpose, a 3D sinc function was used as modeling function (derivated from Kochavi et al.'s idea to use a 2D sinc function to model a subtraction 2D k-space for 2D needle tracking [74], see also Section 2.3.3). Transformed to image space, the proposed 3D sinc function model does not correspond to a cylinder but to a cuboid (as a 1D sinc corresponds to a rect pulse, and a 2D sinc function corresponds to a rectangle), which is, however, used to approximate the expected cylindrical artifact (see discussion in Section 5.2.1). The proposed k-space signal model is given by

$$\begin{aligned} S(\vec{k}, (x_{\text{ac}}, y_{\text{ac}}, z_{\text{ac}}, \theta, \phi, l_c, w_c)) = &\operatorname{sinc}\left(\frac{w_c}{2\pi}(k_x v_{c,1,x}(\theta,\phi) + k_y v_{c,1,y}(\theta,\phi) + k_z v_{c,1,z}(\theta,\phi))\right) \\ &\cdot \operatorname{sinc}\left(\frac{w_c}{2\pi}(k_x v_{c,2,x}(\theta,\phi) + k_y v_{c,2,y}(\theta,\phi) + k_z v_{c,2,z}(\theta,\phi))\right) \\ &\cdot \operatorname{sinc}\left(\frac{l_c}{2\pi}(k_x v_{c,0,x}(\theta,\phi) + k_y v_{c,0,y}(\theta,\phi) + k_z v_{c,0,z}(\theta,\phi))\right) \\ &\cdot \exp(k_x x_{\text{ac}} + k_y y_{\text{ac}} + k_z z_{\text{ac}}), \end{aligned} \tag{3.2}$$

with the wave vector-encoded signal S, the k-space coordinates (k_x, k_y, k_z), the cuboid width and length (l_c, w_c), the unit vector along the long axis of the cuboid $\hat{\vec{v}}_{c,0}$ = ($v_{c,0,x}$,$v_{c,0,y}$,$v_{c,0,z}$), the unit vectors along the short axes of the cuboid $\hat{\vec{v}}_{c,1}$ = ($v_{c,1,x}$,$v_{c,1,y}$,$v_{c,1,z}$) and $\hat{\vec{v}}_{c,2}$ = ($v_{c,2,x}$,$v_{c,2,y}$,$v_{c,2,z}$), and the cuboid center coordinates (x_{ac},y_{ac},z_{ac}). The orientation of $\hat{\vec{v}}_{c,0}$ can be characterized by two angles (θ, ϕ). The two vectors $\hat{\vec{v}}_{c,1}$ and $\hat{\vec{v}}_{c,2}$ (short axes of cuboid) are, by definition, orthonormal to $\hat{\vec{v}}_{c,0}$ (long axis of cuboid) and can be determined from $\hat{\vec{v}}_{c,0}$ using the well-known Gram-Schmidt process (see Appendix A.2).

As described above, Eq. 3.2 was used to model the needle artifact signature in k-space and the parameters (x_{ac},y_{ac},z_{ac},θ,ϕ) are therefore identified with the center of the needle artifact and the needle's orientation. Figure 3.4 schematically shows how the angles θ and ϕ characterize the needle orientation in 3D. θ hereby describes the inclination of the needle to the B_0 field, with an inclination of 0° indicating a needle orientation parallel to $\vec{B}_0$ (same convention as used in Fig. 2.5 for the investigation of needle artifacts in conventional and dephased GRE imaging). ϕ is the corresponding azimuthal angle of the needle axis.

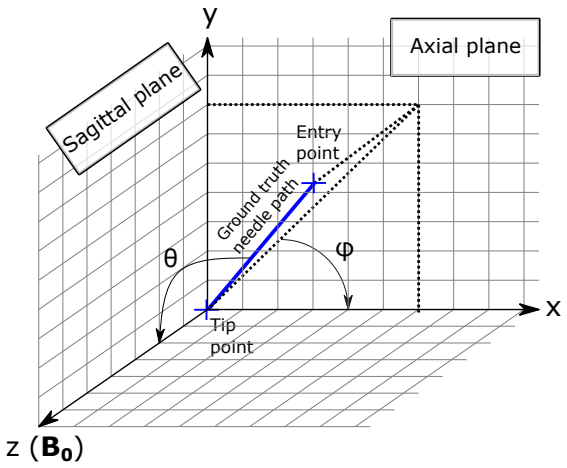

Figure 3.4: The orientation of the needle artifact is defined by the angle θ, the inclination angle enclosed with $\vec{B}_0$, and the angle ϕ, which is the respective azimuthal angle, defined as depicted. The "upright" position of the needle (orthogonal to $\vec{B}_0$) is, therefore, characterized by $(\theta, \phi = (90°, 90°))$.

In Fig. 3.5, the proposed modeling approach is illustrated for explanatory purposes. For an example needle insertion into a tissue phantom, a baseline image acquired before the needle insertion and an image after the needle insertion are depicted together with the subtraction image, reconstructed from the respective k-space data (FLASH sequence implementation as described in Section 3.2.1). A hyperintense, cylinder-shaped needle artifact is visible in the baseline-subtracted image. The respective k-space is modeled using Eq. 3.2 and also reconstructed with the image showing the expected cuboid model artifact. The modeling approach was illustrated for a fully-sampled and undersampled k-space acquisition.

Localization algorithm

Based on the 3D sinc model used to describe the needle artifact in a baseline-subtracted k-space acquisition of a needle insertion, an algorithm for 3D needle artifact localization is proposed (schematically illustrated in Fig. 3.6):

1. Baseline-subtracted k-space acquisition
   To localize the needle after a needle insertion, a k-space acquisition is performed using a radial sampling scheme (see above). An additional baseline acquisition is performed before the needle insertion and the subtraction k-space is calculated.

2. Preprocessing
   In a second step, the acquired baseline-subtracted k-space data is preprocessed. First, the magnitude of the acquired k-space data is normalized. As the introduced 3D sinc k-space model, corresponding to a cuboid in image space as described above, is only designed to approximate the magnitude information of the acquired subtraction image

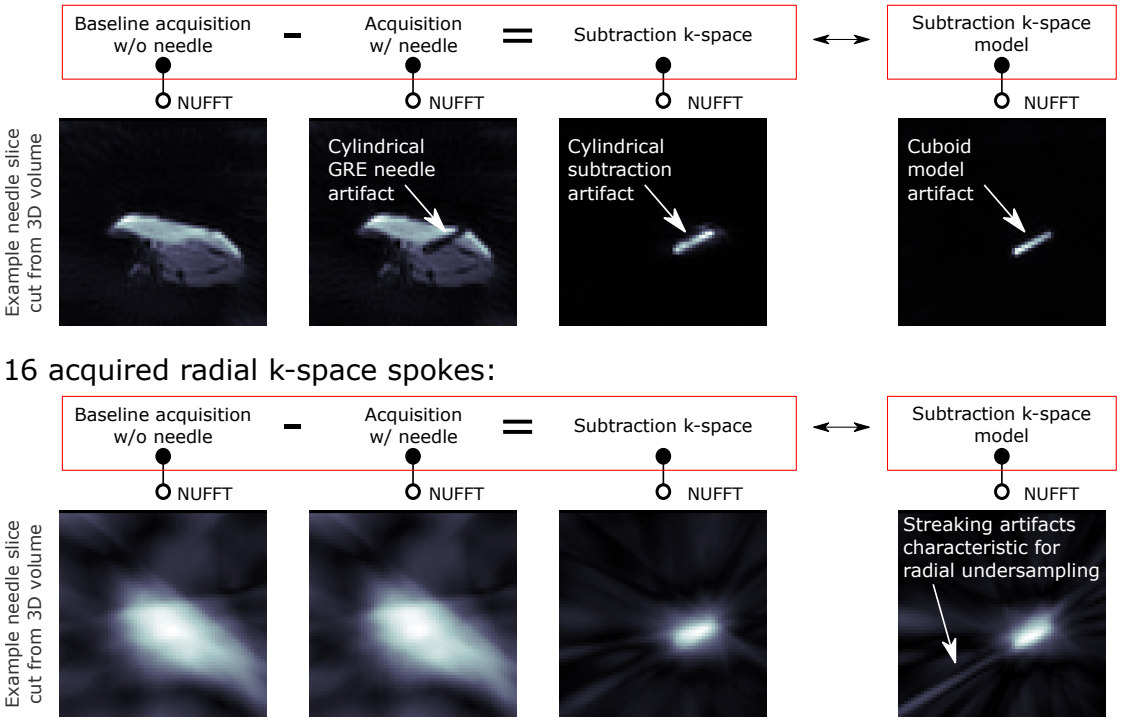

Figure 3.5: Proposed modeling approach for a baseline-subtracted k-space acquisition of an example needle insertion into a porcine tissue phantom (FLASH contrast with radial sequence implementation as described in Section 3.2.1) for an example sampling of 6434 (fully sampled) and 16 radial k-space spokes. From a baseline acquisition and an acquisition during the needle insertion, a subtraction k-space is calculated that contains a distinct signature of the needle corresponding to a cylindrical hyperintense needle artifact in image space (according to the model described in Section 2.3.2). The subtraction k-space is modeled using a 3D sinc function, serving as an approximation to the acquired subtraction k-space (for demonstration purposes, positional and orientational parameters of the needle insertion were extracted manually from the acquired image and used for the model). Images reconstructed from the acquisition and model k-space (using a NUFFT) are shown for illustration purposes only and not required for the k-space-based localization algorithm. Undersampling artifacts (streaking, i.e. aliasing) can be seen for the image reconstruction from 16 k-space spokes.

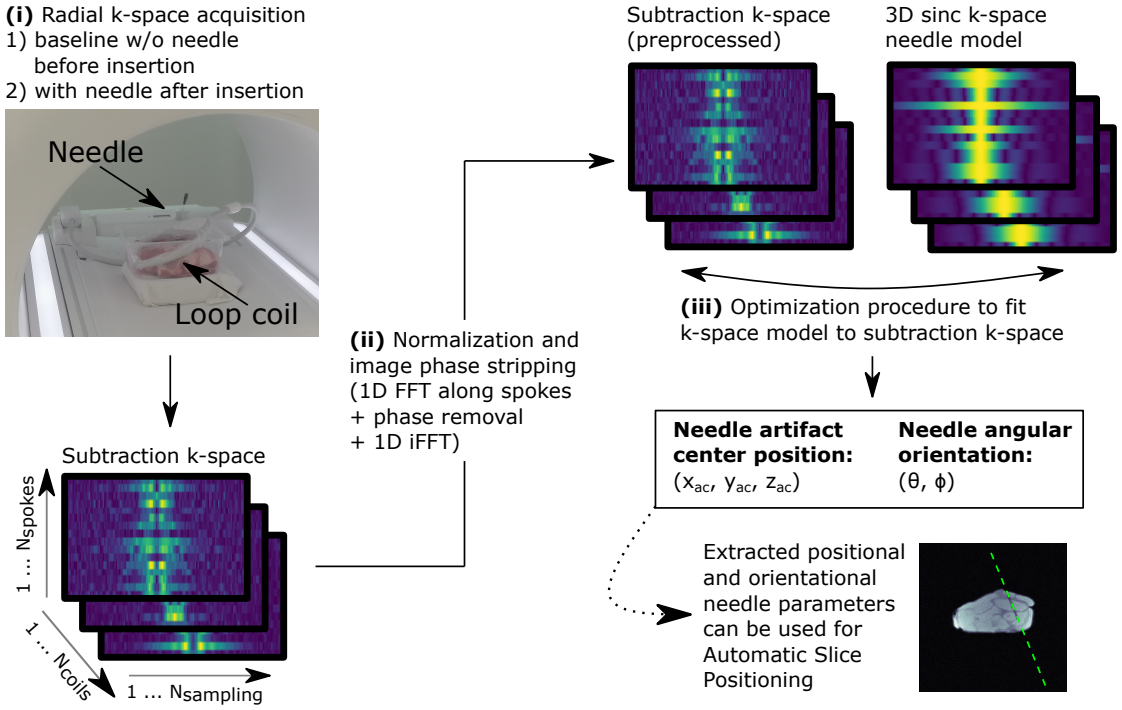

Figure 3.6: Algorithm for rapid 3D needle localization. After a baseline-subtracted k-space acquisition for a needle insertion (i), here shown for an example needle insertion into a porcine tissue phantom, the data is first preprocessed (ii) and then the proposed k-space model (Eq. 3.2) is fitted to the data (iii). The model parameters $(x_{\text{ac}}, y_{\text{ac}}, z_{\text{ac}}, \theta, \phi)$ are directly identified with the needle artifact center and orientation and the best fit parameters issued by the algorithm can be used to automatically align an imaging slice with the fitted needle orientation (green dashed line).

space (i.e., the hyperintense needle artifact) and cannot represent a varying image phase across different acquired coil channels for data acquired with multichannel receiver coils, an image phase stripping step is performed. The image phase is nullified for each coil channel by performing a 1D FFT along each k-space spoke (computationally cheaper compared to a full 3D NUFFT of the complete acquired k-space) and the phase is set to zero. The data is then transformed back into k-space using an inverse 1D FFT.

3. Model fit procedure
   After the preprocessing of the baseline-subtracted k-space acquisition, the proposed 3D sinc model (Eq. 3.2) is fitted to the subtraction k-space using a downhill-simplex method [82, 83], mimimizing the L^2 norm between the model and the acquired data. To make use of all available data for acquisitions with multichannel coils, the optimization problem is formulated in such a way that acquired k-space data from each channel is treated independently and the model's parameters are optimized for the summed loss function across all channels to be minimized. As described above, the model parameters can be directly identified with the position and orientation of the needle artifact. The phase term of the model hereby encodes the centroid coordinates of the needle artifact (x_{ac},y_{ac},z_{ac}). The needle orientation, characterized by the angles ϕ and θ, is encoded by the magnitude of Eq. 3.2, as well as the length l_c of the cuboid modeling the artifact (the width of the cuboid w_c is treated as fixed and an an empirical value was used for the optimization, see below). Following Kochavi et al. [74], magnitude and phase of the model Eq. 3.2 were optimized individually to fit to the acquired subtraction k-space data instead of a more complex joint optimization over all variables at once.

The determined position and orientation of the needle, as found by the performed model fit, can then be used to align a 2D imaging slice with the fitted needle trajectory to allow for ASP. The proposed localization algorithm was implemented in Python (Python Software Foundation, Wilmington, DE, US).

3.2.2 Study on localization performance

To evaluate the proposed needle localization technique, needle insertions were performed in a tissue phantom with different orientational and positional parameters. A set of metrics was defined to characterize the accuracy of the performed needle localizations. Performance of the proposed needle localization technique was evaluated retrospectively with the acquired dataset, using the defined accuracy metrics, and ASP was demonstrated retrospectively for an example needle insertion from the ex-vivo dataset, as well as an in-vivo proof-of-principle case.

Datasets

An ex-vivo dataset of needle insertions into a tissue phantom was acquired. Additionally, a needle insertion from an animal experiment is reported to demonstrate an in-vivo needle localization as a proof-of-principle. Acquisition parameters are summarized in Table 3.1.

Table 3.1: Description of needle insertion datasets (sampled needle trajectories): (a) ex-vivo study and (b) in-vivo proof-of-principle experiment.

	(a) Ex-vivo evaluation	**(b) In-vivo proof-of-principle experiment**
Phantom type	Porcine thigh tissue phantom w/ muscle and fat tissue	In-vivo porcine animal model – needle inserted into thigh
Number of needle insertions	n = 14	n = 1
Needle type	22-gauge aspiration needle	20-gauge aspiration needle
Inclination angle (θ)*	$\theta \in [54°, 88°]$	$\theta = 80.2°$
Azimuthal angle (φ)*	$\varphi \in [22°, 88°]$	$\varphi = 86.2°$
Insertion depth (l)	l = 5 cm	l = 8 cm
Coil set-up	Spine coil + loop coil	Spine coil + flex coil

* Due to symmetry, angles $\theta > 90°$ and $\varphi > 90°$ were mapped to the interval [0°, 90°] by deriving 180° - θ and 180° - φ, respectively.

For the ex-vivo study, k-space data for 14 needle insertions with baseline acquisitions was acquired with a prototype interventional loop coil (iLoop Interventional Coil 0.55T, NORAS MRI products GmbH, Hoechberg, Germany) and a spine coil at $B_0 = 0.55\,\mathrm{T}$ (MAGNETOM Free.Max; Siemens Healthineers AG, Erlangen, Germany). The needle (22-gauge aspiration needle, Cook Medical LLC, Bloomington, IN, USA) was repeatedly inserted randomly in a porcine phantom (thigh tissue) with a varying insertion angle (with inclinations of $\theta \in [54°, 88°]$, see Table 3.1).

For the in-vivo proof-of-principle demonstration, data was acquired using a flex coil and and a spine coil with an analogous system as used for the acquisition of the ex-vivo data. A 20-gauge aspiration needle was used (Cook Medical LLC, Bloomington, IN, USA).

For all data acquisitions, 6434 radial k-space spokes were acquired, corresponding to a fully sampled k-space with the chosen resolution and FOV size as reported in Table 3.1 (see Eq. 2.52 for calculation of the number of required spokes for full sampling). The number of k-space spokes was then retrospectively cropped to evaluate the localization performance depending on the number of acquired k-space lines (see below).

To determine the ground truth of the needle position and orientation, an additional 3D FLASH reference image for each needle insertion was acquired for the ex-vivo scans (FOV = $(256\,\mathrm{mm})^3$; res = $(2\,\mathrm{mm})^3$; T_R = $4.5\,\mathrm{ms}$; T_E = $3.21\,\mathrm{ms}$; fa = $6°$; bw = $1300\,\mathrm{Hz\,px^{-1}}$) and a 3D bSSFP reference image for the in-vivo scan (FOV = $(256\,\mathrm{mm})^3$; res = $(2\,\mathrm{mm})^3$; T_R = $5.56\,\mathrm{ms}$; T_E = $2.78\,\mathrm{ms}$; fa = 706°; bw = $558\,\mathrm{Hz\,px^{-1}}$). A low T_E was chosen to create a concise needle artifact. The needle position and orientation were determined by manually annotating the tip and the entry point of the needle in the 3D reference images. The tip and entry locations were hereby estimated from the visual artifact impression in the reference image (corresponding to the largest extension of the needle image artifact).

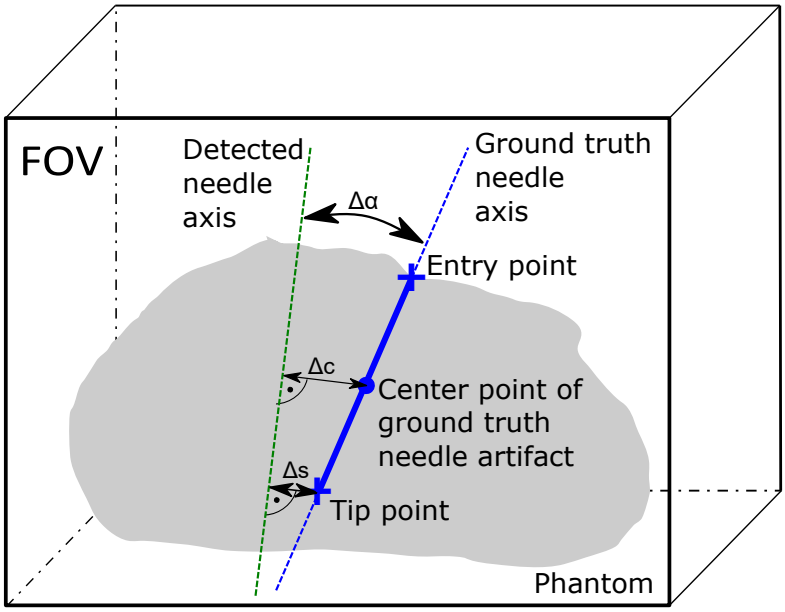

Figure 3.7: Three metrics to analyze the accuracy of the needle localization. $\Delta\alpha$ describes the angular deviation between the ground truth needle orientation. Δc describes the distance between the center point of the ground truth needle artifact and the detected needle axis. Δs describes the distance between the annotated ground truth needle artifact tip and the detected needle axis.

Accuracy metrics

To evaluate the accuracy of the needle localization, the three metrics $\Delta\alpha$, Δc and Δs were defined (Fig. 3.7). $\Delta\alpha$ is a common metric for needle localization accuracy evaluation and describes the angular deviation between the ground truth and the detected needle orientation [32, 33]. As described above, the proposed localization algorithm uses two independent optimization procedures to fit the needle orientation (magnitude of Eq. 3.2) and position (phase of Eq. 3.2). To determine the performance of the positional fit, a second metric was introduced Δc, which describes the distance between the ground truth center of the annotated needle artifact in the reference image and the axis of the optimized model after the localization fit. In MR-guided interventions, visibility of the needle artifact tip is of importance to the interventionalist to successfully hit the target tissue. To account for this, Δs is introduced to identify the maximum distance between the annotated needle artifact tip and the found needle trajectory based on the optimized model parameters after the localization fit. Thus, this metric can be interpreted as the maximum distance of the needle artifact's annotated tip to an arbitrarily oriented slice positioned along the localized needle trajectory.

Performance evaluation and demonstration of automatic slice alignment

For every needle insertion from the ex-vivo dataset, 6434 k-space spokes were acquired (see above). The implemented radial acquisition scheme, as described in Section 3.2.1, allowed a retrospective cropping of the number of acquired k-space spokes (any continuously acquired subset of k-space spokes is approximately uniformly distributed across the radial dimension of k-space due to the implemented golden means acquisition scheme [80]) to investigate a needle localization from a reduced number of sampled k-space lines. In Section 2.3.3, the feasibility of a 3D needle localization from a limited number of k-space spokes was discussed (minimum of 5 k-space lines required to extract positional and orientational parameters as schematically illustrated in Fig. 2.8). For the acquired ex-vivo dataset and the in-vivo proof-of-principle, the localization performance was analyzed depending on the number of k-space spokes utilized by retrospectively cropping the number of used lines for the localization to $n_{\text{spokes},1} = 5$, $n_{\text{spokes},2} = 16$, $n_{\text{spokes},3} = 32$ and $n_{\text{spokes},4} = 64$. The corresponding acquisition times were $t_{\text{acq}}(n_{\text{spokes},1}) = 0.0625\,\text{s}$, $t_{\text{acq}}(n_{\text{spokes},2}) = 0.2\,\text{s}$, $t_{\text{acq}}(n_{\text{spokes},3}) = 0.4\,\text{s}$ and $t_{\text{acq}}(n_{\text{spokes},4}) = 0.8\,\text{s}$.

Three sets of initial optimization parameters were defined and used for the localization algorithm. These can be seen as orientational and positional parameters of an initially more or less severe misaligned 2D imaging slice which could serve as a starting point from which an automatic slice alignment could be triggered. To analyze the localization from different sets of initial parameters, a shift was applied to the ground truth artifact center coordinates $(x_{\text{ac}}, y_{\text{ac}}, z_{\text{ac}})_{\text{true}}$ and needle angles $(\phi, \theta)_{\text{true}}$ (as extracted from the annotated reference images) for each needle insertion to calculate the initial optimization parameters.

1. Initial parameters set (1):
   $(x_{\text{ac}}, y_{\text{ac}}, z_{\text{ac}})_{\text{true}}$ each shifted by an absolute distance of $3.2\,\text{cm}$;
   $(\phi, \theta)_{\text{true}}$ each shifted by an absolute angle of $15°$.
   $\rightarrow$ slight misalignment

2. Initial parameters set (2):
   $(x_{\text{ac}}, y_{\text{ac}}, z_{\text{ac}})_{\text{true}}$ each shifted by an absolute distance of $6.4\,\text{cm}$;
   $(\phi, \theta)_{\text{true}}$ each shifted by an absolute angle of $30°$.
   $\rightarrow$ medium misalignment

3. Initial parameters set (3):
   $(x_{\text{ac}}, y_{\text{ac}}, z_{\text{ac}})_{\text{true}}$ each shifted by an absolute distance of $12.8\,\text{cm}$;
   $(\phi, \theta)_{\text{true}}$ each shifted by an absolute angle of $60°$.
   $\rightarrow$ severe misalignment

The initial parameter for the cuboid model length was kept fixed at $l_c = 6\,\text{cm}$ for all investigations.

For the ex-vivo dataset, the localization quality was evaluated with the introduced metrics and the medians $\widetilde{\Delta\alpha}$, $\widetilde{\Delta c}$ and $\widetilde{\Delta s}$ for the different initial parameter sets and number of used k-space spokes (fixed cuboid width $w_c = 0.8\,\text{cm}$ used for optimization) were calculated. The median was chosen to characterize the ex-vivo dataset as it is robust to outliers produced by failed localization

attempts (see discussion in Section 5.2.3). The mean localization time ($\bar{t}_{\text{loc}}$) was also calculated (data preprocessing + optimization run time).

For the in-vivo demonstration case, the localization accuracy was equally evaluated with respect to the number of acquired k-space spokes and for initial parameter sets 1 and 2 (fixed cuboid width set to $w_c = 1.2\,\text{cm}$ for optimization as a slightly larger needle was used, see Table 3.1b).

To further investigate the optimization procedure, an image reconstruction of the acquired subtraction k-space was performed for one example localization from the ex-vivo dataset (image reconstruction was performed only for evaluation, not used for localization), together with an image reconstruction for the optimized k-space model. Additionally, the cost function of the angular optimization was evaluated for this chosen example from the ex-vivo dataset and the optimization procedure was compared for the initial parameter sets 1 and 3.

The feasibility of ASP was additionally retrospectively investigated for the selected example from the ex-vivo dataset and the in-vivo demonstration case, using the conducted needle localization to reformat a 2D imaging slice along the detected needle axis from the acquired 3D reference image (chosen slice thickness of $8\,\text{mm}$).

3.3 3D needle localization using dephased FLASH contrast and CNN-based postprocessing

A second method for rapid 3D passive needle localization was investigated. Instead of localizing the needle using a baseline-subtracted FLASH k-space acquisition as described in Section 3.2, the needle is localized in (undersampled) d-FLASH images, which are inherently background-suppressed, using a CNN-based postprocessing algorithm.

3.3.1 Technique for needle localization

The proposed needle localization approach utilizes (undersampled) 3D d-FLASH images of a needle insertion. In the images, the position and orientation of the needle were determined with a localization algorithm employing a CNN.

3D radial d-FLASH image acquisition

Compared to the approach proposed in Section 3.2 where a baseline was subtracted from a FLASH acquisition to generate a subtraction k-space which only contained the signature of the needle (background suppression through the subtraction of the baseline), a d-FLASH image acquisition was now employed to generate images with a hyperintense needle artifact and intrinsic background suppression. The same d-FLASH sequence as described and investigated in Section 3.1.2 was used for data acquisition. The utilized radial sampling technique, employing a golden means sampling scheme (same sampling scheme as implemented for conventional FLASH imaging in

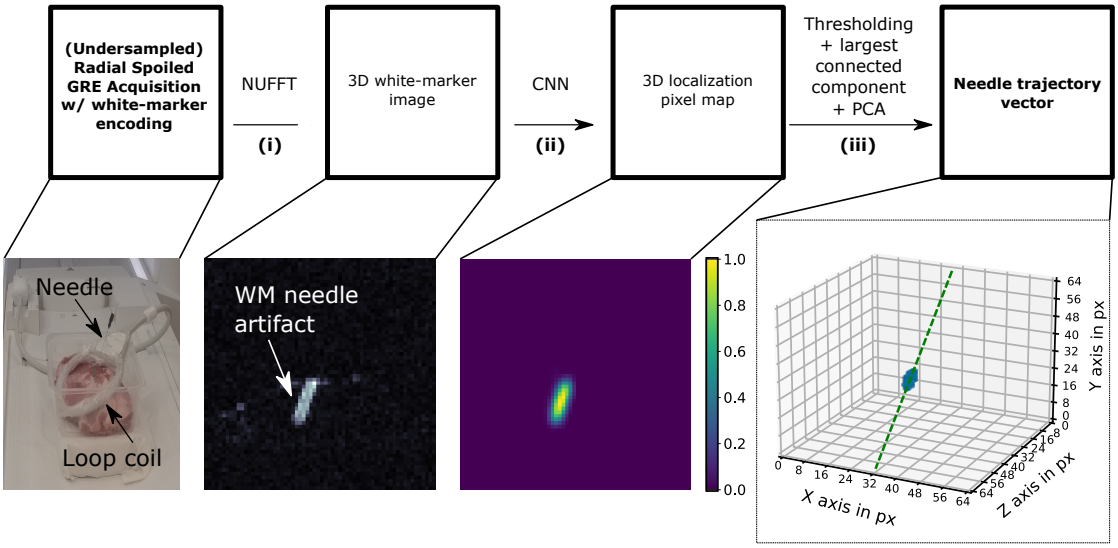

Figure 3.8: Proposed algorithm for 3D needle localization from an (undersampled) 3D d-FLASH acquisition. The algorithm comprises the following steps: (i) Image reconstruction of an (undersampled) 3D d-FLASH acquisition after needle insertion (shown here for example ex-vivo porcine tissue phantom with inserted aspiration needle). (ii) Processing of the image by a trained CNN to perform regression towards the needle path. (iii) Extraction of the needle position and orientation from the CNN's output heatmap (thresholded + largest connected component search) by performing a principal component analysis (PCA) (orientation of the first principle axis is interpreted as the needle's orientation). Figure adapted from Faust et al. [4].

Section 3.2.1), enabled retrospective undersampling while maintaining an approximately uniform k-space coverage [80].

Algorithm for needle localization

An algorithm for 3D needle localization, employing a CNN, was implemented using Python (Python Software Foundation, Wilmington, DE, US). Figure 3.8 illustrates how the implemented localization pipeline processes a d-FLASH acquisition for a sample needle insertion in a porcine tissue phantom to determine the needle position and orientation. The algorithm encloses the following steps:

1. Image reconstruction of an (undersampled) 3D d-FLASH acquisition after needle insertion
2. Processing of the acquired image by trained CNN
3. Extraction of the needle localization parameters from the CNN's output heatmap

After k-space data was captured with the implemented 3D radial d-FLASH MR pulse sequence (see above and Section 3.1.2), it was subsequently reconstructed using a NUFFT method (incor-

porating density correction [53], gridding, and, ultimately, an FFT as described in Section 2.1.4) using the SigPy package [81].

The reconstructed magnitude image is then fed into a CNN for processing. The CNN is employed to map the input image to a heatmap (same resolution as the input d-FLASH image) that represents the needle path. CNNs are a class of models that can represent complex relationships between data [84–86]. The data is processed by applying a number of filters to the data in a specific manner (forming the so-called architecture of the network). By changing the parameters characterizing the network, the CNN can be optimized to represent a specific relationship between input (feature) and output (label) data. CNNs were hereby specifically designed to perform well on data which holds interrelated information, such as images. A CNN is typically arranged in layers, through which the data is passed in one direction (feed-forward network), and consists of different building blocks, which commonly include convolutional layers, activation functions and down-/upsampling layers. Convolutional layers consist of filters (also referred to as kernels), matrices of a distinct size and characterized by their values (weights). The input data is multiplied with the filters by sliding them across it (convolution operation) with a certain stride length. Applying a certain number of filters to the input data will create an according number of output (feature) maps which can be passed to the next layer of the network. Each filter interacts with certain features in the input data. Convolution layers are often applied together with a non-linear activation function, e.g. a rectifier, which is defined as $\mathrm{ReLU}(x) = \max(0, x)$ [87]. Another type of commonly employed building blocks are down-/upsampling layers. These layers allow to reduce or increase the size of a feature map. This can be achieved by, e.g., employing a so-called max-pooling operation by sliding a maximum filter of a certain size across the feature map or by locally duplicating the feature map's elements. The reasoning behind scaling the feature maps' size with down-/upsampling layers is that a convolutional filter with a certain size which is applied to differently sized feature maps acts on varying scales, due to the varying size of receptive field, and can therefore take into account correlations of different scales in the input data. Due to the multitude of variable parameters characterizing a CNN, it can serve as a mapping or function approximater which is customized by optimizing over the parameters of the model to approximate a specific relation. In contrast to a handcrafted approach where a mapping function is predefined, a machine learning (ML) approach as employed with CNNs uses a set of pairs of corresponding input and output data (so-called training data) to approximate the mapping by optimizing over the parameters of the employed net (supervised learning), aiming to increase the resemblence of the net's output and the ground truth output data. This resemblance is hereby measured by a loss function. An employed loss function for regression tasks is the mean squared error (MSE)- or L^2 loss [88]. Trained models can often outperform handcrafted models, as they are capable of capturing relevant relations between the input and output data. Common optimization algorithms are used for the training of the network, with a stochastic gradient descent (SGD) algorithm being used in this work. CNNs have been employed in the past to localize a needle from acquired MR images by various authors [32, 33, 89]. Due to their ability to efficiently capture spatial correlation, they are often used for image segmentation or regression tasks ([88, 90]). A commonly used architecture is the so-called U-Net [91, 92]. Applying a series of down- and consequent upsampling operations, together with so-called skip connections directly linking different layers of the network, it is able to capture relations of different scales as common in image data. For the localization algorithm implemented

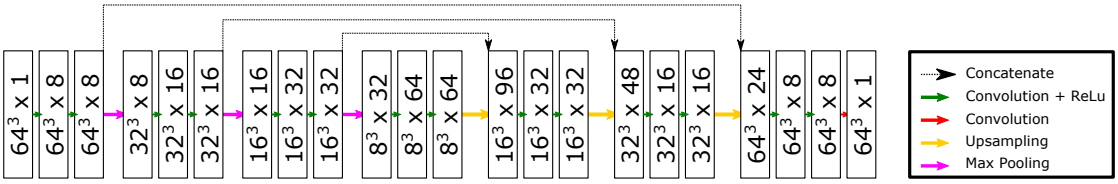

Figure 3.9: Construction of the implemented CNN (3D U-Net architecture [92]) for the proposed rapid 3D needle localization method. A 3D image is fed into and consequently processed by the net. The boxes represent the layers of the net and are labeled with the image matrix size and the number of the respective feature maps (image matrix $\times$ number of feature maps). Figure reproduced from Faust et al. [4].

in this work, a U-Net was used to model the mapping from the acquired d-FLASH image of the needle insertion to a heatmap, indicating the needle path. A 3D U-Net architecture [92] was implemented with Tensorflow (Google Brain, Mountain View, CA, USA) and is depicted schematically in Fig. 3.9. The implemented network comprises a contracting and expanding path. Each contracting step involves two $3 \times 3 \times 3$ convolutions (zero-padded, stride of 1), each succeeded by a ReLU activation, followed by a $2 \times 2 \times 2$ downsampling operation (max-pooling) with a stride of 2. After the final downsampling step, a bottleneck step follows with another two $3 \times 3 \times 3$ convolutions (zero-padded, stride of 1), each with a ReLU activation, before the data is fed to the expanding path. Here, each step includes a $2 \times 2 \times 2$ upsampling with stride 1, followed by two $3 \times 3 \times 3$ convolutions (zero-padded, stride of 1), each with ReLU activation. The number of feature maps doubles after each downsampling step and is halved after each upsampling step. Skip connections link steps in the contracting path to their expanding counterparts, concatenating the respective feature maps. Ultimately, a linear activation convolution layer reduces the number of feature maps to a single one at the end.

From the CNN output heatmap, the position and orientation of the needle path were determined by first applying a threshold ($> 50\,\%$ of the heatmap maximum value). If the thresholded heatmap comprises multiple connected segments, i.e. multiple regions are presumed by the network to potentially contain a needle, the largest segment is chosen (as only one needle is inserted at a time into the tissue). To determine the needle orientation from this preprocessed heatmap, a PCA is performed. This technique, as previously employed for determining object orientation in MR scans from CNN-based segmentation by Zhao et al. [93], essentially fits an ellipsoid to the data. The primary principal axis derived is interpreted as the needle axis. The centroid of the CNN heatmap is interpreted as the center point of the needle path.

3.3.2 Study on localization performance

To investigate the proposed algorithm for 3D needle localization, the implemented CNN was first trained using data acquired from ex-vivo needle insertions in porcine tissue phantoms. To evaluate achievable localization accuracy with the proposed method, an ex-vivo study was conducted

using similar phantoms. The method was additionally applied to needle insertions in two different porcine animal models to provide an in-vivo proof-of-principle.

Due to the intrinsic background suppression with dephased GRE imaging, the acquired images of a needle insertion were expected to contain an isolated positive contrast needle artifact, characterized by the positional and orientational parameters of the inserted needle, as investigated in Section 3.1.2. In Section 2.3.3, feasibility of a needle localization from a limited k-space acquisition, considering the limited number of degrees of freedom characterizing the needle insertion, was discussed. Following this argument, a fit of the investigated needle model to only a few acquired subtraction k-space lines was evaluated for the localization method described in Section 3.2. For the CNN-based needle localization algorithm employing an intrinsically background-suppressed d-FLASH acquisition as introduced here, needle localization in an image reconstructed from a similarly undersampled k-space acquisition was equally investigated to accelerate the needle localization for real-time applicability.

Datasets

To train the CNN and evaluate the needle localization technique, three datasets were collected as described in Table 3.2. Each dataset was obtained at a magnetic field strength of B_0 = 0.55 T (MAGNETOM Free.Max; Siemens Healthineers AG, Erlangen, Germany).

Training Dataset To create a dataset of corresponding input (d-FLASH images of needle insertions) and output data (heatmaps showing the respective needle path) for the training of the CNN, a 22-gauge MR-compatible aspiration needle (Cook Medical, Bloomington, IN, USA) was repeatedly inserted into seven porcine tissue phantoms (muscle tissue, permeated with fatty tissue). In total, d-FLASH image data was acquired for 274 needle paths in the selected angular range (refer to Table 3.2 for details on the dataset acquisition). A 4-fold data data augmentation was conducted by randomly shifting the FOV reconstructed from the acquired d-FLASH k-space data (care was taken to ensure that the needle path still remained entirely within the FOV after shifting). In addition to the d-FLASH acquisition, a conventional RF-spoiled FLASH image was acquired for each needle insertion (FOV $= (256\,\mathrm{mm})^3$; res $= (2\,\mathrm{mm})^3$; $T_\mathrm{R} = 4.5\,\mathrm{ms}$; $T_\mathrm{E} = 2.31\,\mathrm{ms}$; fa $= 6°$; bw $= 1600\,\mathrm{Hz\,px^{-1}}$). From the FLASH image, the ground truth needle path was determined by manually annotating the entry and tip point of the needle in the tissue sample. From the manually annotated needle entry and tip positions, label images were created by drawing a Gaussian filter-blurred line (standard deviation of $6\,\mathrm{mm}$) between the points (Gaussian heatmaps for CNN-based regression were previously used in [88]). Annotation and label creation are shown for an example needle insertion in Fig. 3.10. For the acquisition of the training data, the phantom was rotated for each insertion to increase variation in the image data as some signal in the image, unrelated to the needle (e.g., due to partial volume effects [24], also see discussion in Section 5.2.2), was expected to persist despite the intrinsic background suppression with the d-FLASH acquisition technique. By rotating the phantom, any artifacts unrelated to the needle would be expected to present differently in the images, decreasing the risk of the CNN learning any image characteristics unrelated to the needle, but specific to a particular phantom used in

Table 3.2: Description of datasets used for training of the implemented CNN, in the ex-vivo localization study and in the in-vivo proof-of-principle experiments investigating the proposed CNN-based rapid 3D needle localization technique. d-FLASH imaging sequence parameters and sampled needle trajectories are provided. Table adapted from Faust et al. [4] (angle definition adjusted to match Fig. 3.4).

	Ex vivo training set	**Ex vivo test set**	**In vivo proof-of-principle experiments**
Number of phantoms/in vivo models	7	4	2
Number of images	$n_{total} = 257$ ($n_1 = 36, n_2 = 49, n_3 = 36, n_4 = 40, n_5 = 19, n_6 = 36, n_7 = 41$); $n_{total\,(aug)} = 1028$ with four-fold augmentation; split into training/validation set: 90%/10%)	$n_{total} = 109$ ($n_1 = 40, n_1 = 21, n_3 = 19, n_4 = 29$)	$n_{total} = 3$ ($n_1 = 1, n_2 = 2$)
Needle type	22-gauge aspiration needle	22-gauge aspiration needle	20-gauge (animal 1) and 22-gauge aspiration needle (animal 2)
Inclination (ϑ)*	$\vartheta \in [73°, 90°]$	$\vartheta \in [78°, 90°]$	$\vartheta_1 = 87.7°; \vartheta_2 = 88.8°; \vartheta_3 = 77.6°$
Azimuthal angle (φ)*	$\varphi \in [60°, 90°]$	$\varphi \in [60°, 90°]$	$\varphi_1 = 89.7°; \varphi_2 = 74.3°; \varphi_3 = 72.7°$
Insertion depth (I)	$I \in \{4\,cm, 5\,cm\}$	$I \in \{4\,cm, 5\,cm\}$	$I_1 = 11\,cm; I_2 = 8\,cm; I_3 = 8\,cm$
Echo time (TE)	TE = 10 ms	TE = 10 ms	TE = 10 ms
Repetition time (TR)	TR = 12.5 ms	TR = 12.5 ms	TR = 15 ms
Field of view	$(256\,cm)^3$	$(256\,cm)^3$	$(256\,cm)^3$
Resolution	$(4\,mm)^3$	$(4\,mm)^3$	$(4\,mm)^3$
Flip angle	10°	10°	10°
Bandwidth	900 Hz/px	900 Hz/px	160 Hz/px
Coil set-up	Head coil	Spine coil + loop coil	Spine coil + loop coil (animal 1 & 2) / Spine coil + flex coil (animal 2)

* Due to symmetry, angles $\theta > 90°$ and $\varphi > 90°$ were mapped to the interval [0°, 90°] by deriving 180° - θ and 180° - φ, respectively.

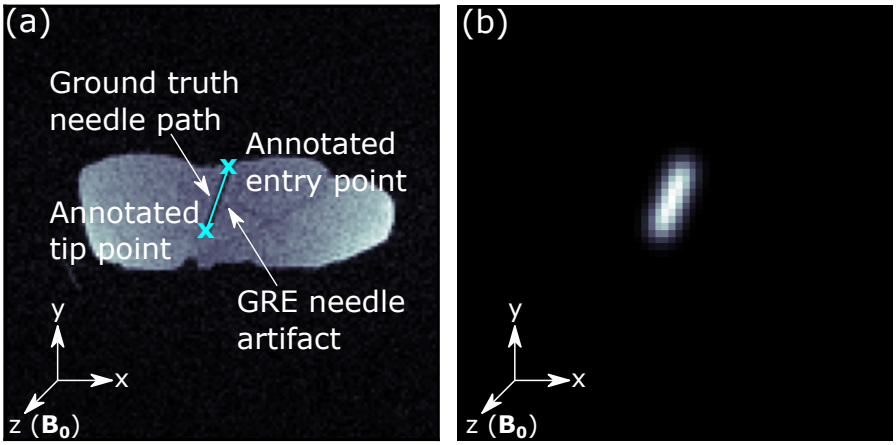

Figure 3.10: (a) Annotation of the acquired ex-vivo data for training of the implemented CNN and evaluation of the proposed CNN-based rapid 3D needle localization method. Needle entry and tip point were marked in reference 3D FLASH images acquired together with the d-FLASH images used for localization. Here, a 2D plane containing the needle artifact was reformatted from an acquired 3D reference image of the training dataset to illustratively show the annotation. (b) Label creation for training of the implemented CNN. The label images were created automatically from the annotation data by connecting the marked entry and tip point of the needle with a gaussian-blurred line (standard deviation $= 6\,\mathrm{mm}$). Figure adapted from Faust et al. [4].

the training dataset. For the acquisition of the training data, the phantoms were placed in a head coil to simplify repositioning of the phantoms without altering the coil set-up. Orientations of the needle insertions were sampled randomly, characterized by the angles θ and ϕ defined in Fig. 3.4 as also used to characterize needle orientation for the localization method described in Section 3.2. θ was sampled from $\theta \in [73°, 90°]$ and ϕ was sampled from $\phi \in [60°, 90°]$ (due to symmetry, angles $\theta > 90°$ and $\phi > 90°$ were mapped to the interval $[0°, 90°]$ by deriving $180° - \theta$ and $180° - \phi$, respectively). Insertion depths were set manually and ranged from $4\,\mathrm{cm}$ to $5\,\mathrm{cm}$.

Ex-vivo test dataset To evaluate the achievable localization precision for needle localizations using the implemented method, the same 22-gauge needle as used to create the training data for the CNN was inserted into four additional ex-vivo porcine tissue models, generating a test dataset of d-FLASH images. Again, additional reference FLASH images were acquired for each needle insertion (same sequence parameters used as for the training dataset) to extract the ground truth needle tip and entry points. A total of 109 needle insertions were sampled (see Table 3.2 for details on the dataset). The needle orientations were randomly sampled, manually inserting the needle within an angular range of $\theta \in [78°, 90°]$ and $\phi \in [60°, 90°]$, again adjusting the depth of insertion between $4\,\mathrm{cm}$ and $5\,\mathrm{cm}$. The sampled insertion angles and depths were selected to lie within the range sampled for the acquisition of the training dataset. The data was acquired using the spine coil of the used MRI system and a loop coil (iLoop Interventional Coil 0.55T;

NORAS MRI products GmbH, Höchberg, Germany), dedicated for interventional MRI (depicted in Fig. 3.8).

In-vivo proof-of-concept experiment A 20-gauge and 22-gauge needle (Cook Medical, Bloomington, IN, USA) were inserted into the thigh muscle of two pigs (details found in Table 3.2) in a proof-of-concept in-vivo experiment. Similar to the acquisition of the ex-vivo test dataset, d-FLASH and reference FLASH images (same sequence parameters for FLASH as given above) were obtained for the needle insertion in the first pig, while d-FLASH and bSSFP images were collected for the insertions in the second pig. bSSFP imaging was used here as an alternative contrast technique for reference image acquisition due to a favorable signal-to-noise ratio (SNR), using the following sequence parameters: FOV $= (256\,\mathrm{mm})^3$; res $= (2\,\mathrm{mm})^3$; $T_\mathrm{R} = 5.56\,\mathrm{ms}$; $T_\mathrm{E} = 2.78\,\mathrm{ms}$; fa $= 70°$; bw $= 558\,\mathrm{Hz\,px^{-1}}$.

Training of the CNN

For the evaluation of the proposed localization technique, the implemented CNN was first trained, utilizing the aforementioned training dataset. In order to evaluate the needle localization from an undersampled k-space acquisition, d-FLASH images were reconstructed from various numbers of k-space spokes by retrospectively cropping the collected k-space data: $n_{\text{spokes},1} = 6434$ (corresponds to a fully sampled image acquisition according to the Nyquist theorem for uniform radial k-space coverage [54] as described in Section 2.1.4), $n_{\text{spokes},2} = 256$, $n_{\text{spokes},3} = 128$, $n_{\text{spokes},4} = 64$, $n_{\text{spokes},5} = 32$, $n_{\text{spokes},6} = 16$. For each number of employed k-space spokes for image reconstruction ($n_{\text{spokes},1}$ to $n_{\text{spokes},6}$), a separate CNN model was trained. The CNN was optimized to regress from the (undersampled) d-FLASH image to the needle path (label image) using an L^2 loss function and a SGD optimizer (number of epochs = 200; learning rate = 0.1; learning rate decay = 1×10^{-6}; Nesterov momentum = 0.9; batch size = 8). Therefore, a total of six models were created. Training was performed on a DGX-1 cluster with 8 Tesla V100 32 GB GPUs (Nvidia Corporation, Santa Clara, CA, USA).

Accuracy Metrics and Performance Evaluation

To evaluate the localization accuracy, the same metrics as introduced in Section 3.2 and defined in Fig. 3.7 were used, without Δc. $\Delta\alpha$ refers to the angle between the ground truth needle axis and the axis as detected by the localization algorithm. If the localization technique were to be used for ASP, $\Delta\alpha$ would indicate the greatest angular discrepancy between an automatically chosen imaging plane and the actual needle orientation. As also described in Section 3.2, $\Delta\alpha$ serves as a standard metric for assessing the orientation accuracy of needle localization and has been reported in the literature for other needle localization techniques [32, 33]. Δs was defined as the distance between the ground truth needle tip location and the detected needle axis, therefore describing the largest possible distance from the tip to a selected imaging plane aligned with the detected needle axis. A large Δs hence indicates that the tip will likely not be visible in an

automatically aligned 2D image plane. In contrast to the evaluation of the method investigated in Section 3.2, Δc, which was introduced as a metric describing the distance of the ground truth needle path center to the detected needle axis, was not evaluated here. In Section 3.2, Δc was introduced to individually assess the separate optimization over the magnitude and phase of the introduced complex k-space model. As the phase of the model was independent of the orientation, but dependent on the position of the needle artifact, Δc was introduced as a metric in order to take this into account (not applicable to the CNN approach). Therefore, for the introduced CNN-based needle locliazation, the ex-vivo test dataset, as well as the samples from the in-vivo proof-of-principle experiment were assessed for $\Delta\alpha$ and Δs only.

In the implemented d-FLASH imaging sequence (see Section 3.1.2), the WM gradient $\vec{G}_{\text{WM}}$ is applied in the same direction as $\vec{B}_0$. The needle therefore encloses the angle θ with the WM gradient, as well as also with the $\vec{B}_0$ field. In Section 2.3.2, it was described how a WM gradient moment, acting at an angle θ to a needle, can only be partially counteracted by the needle-related susceptibility-induced gradient moment, as the susceptibility-induced gradient always acts orthogonal to the needle axis for the infinite cylinder model [9]. The component of $\vec{G}_{\text{WM}}$ acting orthogonal to the needle will therefore always introduce a global dephasing, reducing the overall signal magnitude of the artifact. In order to evaluate how the angle of the needle in relation to the $\vec{B}_0$ and $\vec{G}_{\text{WM}}$ direction affects the quality of the localization, considering an expected decrease of signal magnitude for needle orientations increasingly parallel to $\vec{B}_0$ and $\vec{G}_{\text{WM}}$, the samples from the ex-vivo test dataset were categorized into three groups based on different inclination angle ranges: $\theta \in (86°, 90°]$; $\theta \in (82°, 86°]$; $\theta \in (78°, 82°]$. For each subset, the medians $\widetilde{\Delta\alpha}$ and $\widetilde{\Delta s}$ along with the median absolute deviation were computed for the evaluated metrics. All localizations were performed retrospectively on PC hardware (Core i7-10850H CPU with 2.70 GHz base frequency, Intel, Santa Clara, CA, USA; Quadro T2000 GPU, Nvidia, Santa Clara, CA, USA). Reconstructions were computed on the CPU (non-parallelized), while the GPU was employed for the CNN predictions.

The localization accuracy required to align a 2D imaging plane with a needle so that the needle is visible in the 2D image, depends on the thickness of the imaging slice chosen, as well as the dimensions of both the needle and the induced artifact. Ensuring the needle tip is visible in the selected slice is particularly critical during interventions to verify accurate targeting, e.g., of suspicious lesions. Thus, the defined metric Δs holds significant clinical value for interventionalist. A successful ASP demands a minimal Δs value. For the conducted ex-vivo study, the number of acceptable localizations was hence assessed by setting a threshold below which the value Δs must lie for the localization to be considered successful. The localization success rate (number of samples with Δs < threshold / total number of samples) was investigated for the three angular bins described above and three distinct thresholds: $\Delta s < 4\,\text{mm}$; $\Delta s < 8\,\text{mm}$; $\Delta s < 12\,\text{mm}$.

Additionally to the evaluation of the defined metrics for the investigated needle insertions, for the in-vivo proof-of-principle and two example needle insertions from the ex-vivo dataset, the feasibility of ASP was investigated by retrospectively reformatting a 2D imaging slice from the 3D reference image acquired with each d-FLASH image, utilizing the position and orientation

of the needle as detected with the proposed localization algorithm (chosen slice thickness = $4\,\mathrm{mm}$).

4 Results

Findings for the conducted characterization of needle artifacts with conventional and dephased GRE (see Section 3.1) were reported in Section 4.1. Evaluation results for the investigated forward model-based needle localization approach (see Section 3.2) were reported in Section 4.2 and results for the investigated CNN-based localization approach (see Section 3.3) were reported in Section 4.3.

4.1 Characterization of needle artifacts

In Section 4.1.1, evaluation results for the conducted investigation of needle dephasing artifacts for FLASH imaging (see Section 3.1.1) were reported. In Section 4.1.2, evaluation results for the conducted investigation of positive susceptibility-based contrast imaging of needles with dephased GRE (see Section 3.1.2) were reported.

4.1.1 Needle artifacts in FLASH imaging

In Fig. 4.1, three example 2D images slices are shown, depicting the artifact of the investigated needle in a water phantom (xy-plane and zx-plane, as well as zx-plane image masked at $50\,\%$ of the background signal evaluated in an ROI), which were selected from the set of 3D FLASH images acquired with different imaging parameters (as described in Section 3.1.1). The proposed dephased disk model (see Section 2.3.2) is indicated in the image by a circle with the predicted artifact radius (Eq. 2.71) for the respective imaging parameters and according to the model.

As described in Section 3.1.1, the two metrics DSC and d_H were evaluated for all sampled imaging parameters in a slab of 10 slices (indicated by white dotted lines for example images in Fig. 4.1) with mean values and standard deviation reported in Table 4.1. Found DSC values were above $86\,\%$ for all investigated imaging parameters. The found maximum values for d_H, interpreted as the deviation of of the measured and modeled artifact radius, were approximately 1.5 times the chosen voxel size for the investigated cases (e.g., $d_H = 2.8\,\mathrm{mm}$ for the artifact at $B_0 = 1.5\,\mathrm{T}$, $T_\mathrm{E} = 25\,\mathrm{ms}$ and res $= (2\,\mathrm{mm}^3)$).

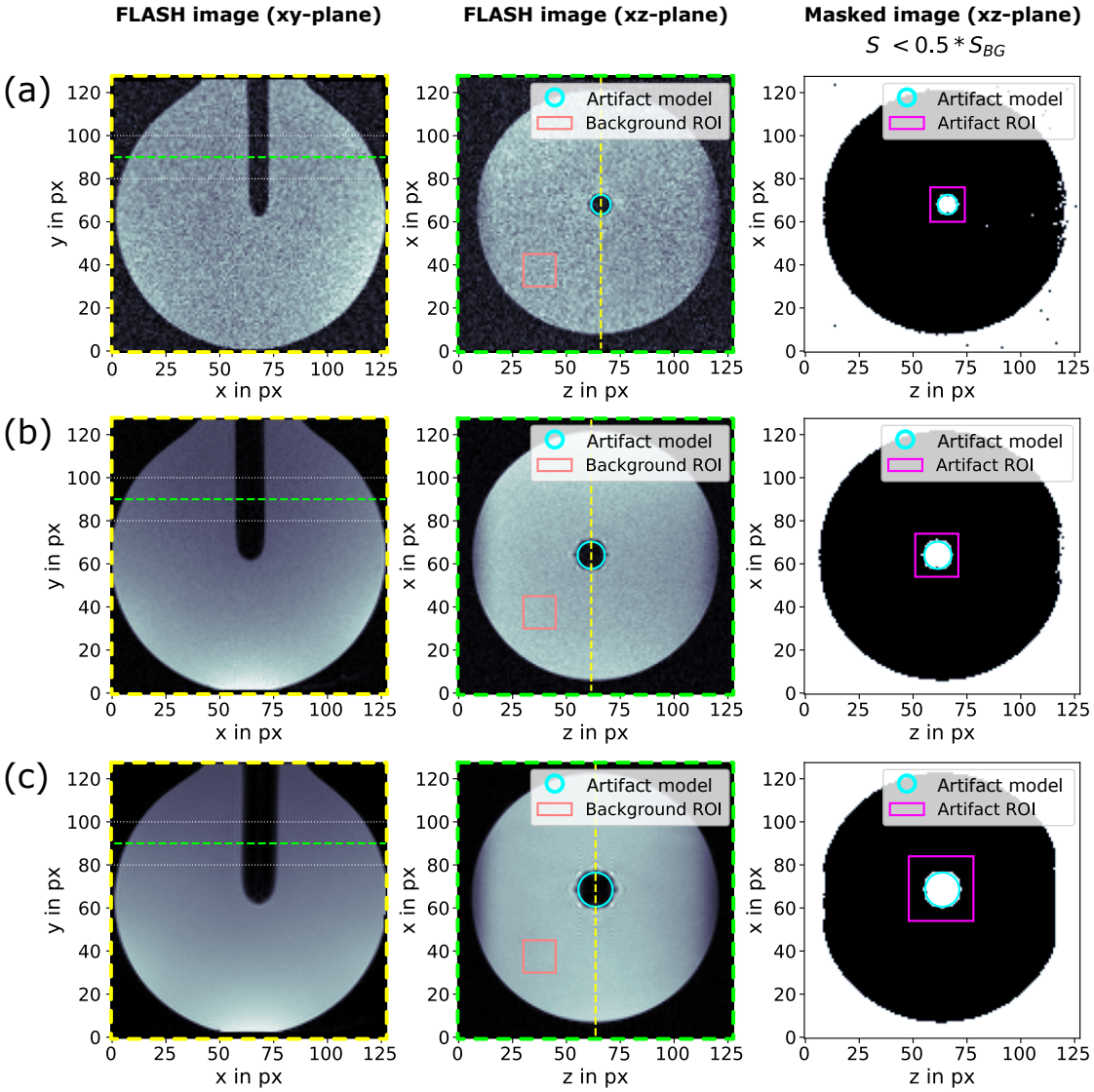

Figure 4.1: Needle (diameter: 20-gauge, material: Inconel) placed in a water phantom orthogonal to B_0, imaged at 0.55 T (a), 1.5 T (b) and 3 T (c) using a FLASH sequence with $T_{\mathrm{E}} = 25\,\mathrm{ms}$. Following the description in Fig. 2.5, the FLASH needle artifact is depicted in the xy-plane (first column) and the zx-plane (second column). Additionally, the image showing the needle in the zx-plane was masked ($S < 0.5 S_{\mathrm{BG}}$; background signal S_{BG} averaged over indicated ROI) and the masked image is depicted in the third column. The artifact model as described by Eq. 2.71 is indicated by the blue circle. DSC and d_H were evaluated (see Table 4.1) for the modeled and the measured artifact within a defined artifact ROI and for a slab of 10 slices, indicated by the white dotted lines in the xy-plane view. Figure reproduced from Faust et al. [1].

Table 4.1: Results of the comparison of the needle artifact in acquired FLASH images to the proposed artifact model for various sequence parameters, using DSC and d_H. The artifact radius r_{FLASH}, as calculated from Eq. 2.71, is also given. Maximum and minimum found DSC values are highlighted in green and red, respectively. A zero standard deviation indicates no found differences for the respective metric across the slices of the evaluated slab. Table adapted from Faust et al. [1].

	TE_1 = 5 ms	TE_2 = 15 ms	TE_3 = 25 ms
B0 = 0.55T			
res = $(1\ \text{mm})^3$	r_{FLASH} = 2.6 mm DSC = 0.892 ± 0.025 d_H = (1.0 ± 0.1) mm	r_{FLASH} = 3.8 mm DSC = 0.933 ± 0.017 d_H = (1.2 ± 0.4) mm	r_{FLASH} = 4.5 mm DSC = 0.933 ± 0.016 d_H = (1.1 ± 0.3) mm
res = $(2\ \text{mm})^3$	r_{FLASH} = 3.3 mm DSC = 0.905 ± 0.023 d_H = (2.0 ± 0.0) mm	r_{FLASH} = 4.8 mm DSC = 0.872 ± 0.011 d_H = (2.0 ± 0.0) mm	r_{FLASH} = 5.7 mm DSC = 0.952 ± 0.010 d_H = (2.0 ± 0.0) mm
B0 = 1.5T			
res = $(1\ \text{mm})^3$	r_{FLASH} = 3.7 mm DSC = 0.882 ± 0.006 d_H = (1.0 ± 0.0) mm	r_{FLASH} = 5.3 mm DSC = 0.901 ± 0.003 d_H = (2.0 ± 0.0) mm	r_{FLASH} = 6.3 mm DSC = 0.917 ± 0.004 d_H = (2.0 ± 0.0) mm
res = $(2\ \text{mm})^3$	r_{FLASH} = 4.6 mm DSC = 0.865 ± 0.000 d_H = (2.0 ± 0.0) mm	r_{FLASH} = 6.7 mm DSC = 0.887 ± 0.005 d_H = (2.8 ± 0.0) mm	r_{FLASH} = 7.9 mm DSC = 0.883 ± 0.006 d_H = (2.8 ± 0.0) mm
B0 = 3T			
res = $(1\ \text{mm})^3$	r_{FLASH} = 4.6 mm DSC = 0.919 ± 0.006 d_H = (1.0 ± 0.0) mm	r_{FLASH} = 6.7 mm DSC = 0.923 ± 0.003 d_H = (1.0 ± 0.0) mm	r_{FLASH} = 7.9 mm DSC = 0.930 ± 0.002 d_H = (1.0 ± 0.0) mm
res = $(2\ \text{mm})^3$	r_{FLASH} = 5.9 mm DSC = 0.895 ± 0.017 d_H = (2.0 ± 0.0) mm	r_{FLASH} = 8.4 mm DSC = 0.909 ± 0.012 d_H = (2.2 ± 0.4) mm	r_{FLASH} = 10.0 mm DSC = 0.912 ± 0.007 d_H = (2.0 ± 0.0) mm

4.1.2 Needle artifacts in dephased GRE imaging

Dephased GRE contrast imaging of a needle in a water phantom was evaluated as described in Section 3.1.2. In Fig. 4.2, a reference SE image of the needle phantom is shown, as well as images acquired with the implemented d-FLASH, d-SSFP, and d-bSSFP sequences. In both the d-FLASH and d-SSFP contrast images, three signal maxima are observed within the zx-plane, forming three stripes alongside the needle shaft. The formed positive contrast artifact is axisymmetric with the axis of symmetry running through the needle shaft in z-direction. For d-bSSFP contrast, six signal maxima are present in the depicted zx-plane image, constituting a point-symmetric artifact. While the d-FLASH and d-bSSFP images exhibit a spatially uniform positive contrast needle artifact, the artifact in the d-SSFP image is interrupted by multiple dark bands (see discussion in Section 5.1.2).

The maximum artifact magnitude observed for d-bSSFP and d-FLASH, relative to d-SSFP, was found to be 0.56 ± 0.09 and 0.19 ± 0.04. The theoretically expected signal ratio between d-bSSFP and d-SSFP (approximately 0.64, see Section 2.3.2) was thus found to lie within one standard deviation of the experimental measurement. The measured cumulative signal magnitude for d-bSSFP and d-FLASH, again evaluated relative to the d-SSFP cumulative magnitude, was found to be 1.13 ± 0.07 and 0.19 ± 0.01. Therefore, the theoretical cumulative signal ratio for d-bSSFP and d-SSFP (approximately 1.27, see again Section 2.3.2) lies within two standard deviations of the value observed experimentally. When directly contrasting d-bSSFP with d-FLASH, d-bSSFP shows a maximum artifact signal and cumulative signal magnitude that are 2.9 ± 0.5 and 5.9 ± 0.4 times higher, respectively, than those of d-FLASH.

Figure 4.3 illustrates how the needle artifact for d-bSSFP imaging varies for different T_{E}. d-bSSFP images corresponding to four example T_{E} are depicted in Fig. 4.3a. The radius of the needle WM artifact increased with increasing T_{E}. Some stripe-like artifacts that appear in the water phantom can be noticed, seemingly unrelated to the needle (potentially eddy current-induced effects that can appear when employing a radial image acquisition for bSSFP contrast [94]; see dicussion in Section 5.1.2). The position of the needle shaft was extracted from the reference spin-echo image and indicated in the depicted d-bSSFP images (marked with a white dot). Dashed and solid lines indicate the estimated location where $m_{0,\mathrm{susc},x}$ vanishes and $|m_{0,\mathrm{susc}}| = m_{0,\mathrm{WM},z}$, following the investigated model for the d-bSSFP needle artifact (see Section 2.3.2) and as shown schematically in Fig. 2.7. The position of the pixels with the highest signal intensity, predicted by the model to lie on the dashed lines, deviate by no more than one pixel from the dashed lines. In Fig. 4.3b, the radius of the artifact, as measured in the acquired images, is plotted against T_{E}. The plot also includes the predicted artifact radius derived from the model. The measurements of the artifact radius from the experiment were found to be in accordance with the model's predictions, remaining within the measurement uncertainty margin, across all examined T_{E}. Performing a fit of the artifact radius model Eq. 2.74 to the acquired radius measurements (not depicted in the image), choosing the needle susceptibility χ_i as a free parameter, resulted in a found value of $\chi_{i,\mathrm{exp}} = (8 \pm 2) \times 10^{-4}$ for which the literature value of $\chi_i = 568 \times 10^{-6}$ (value for Inconel [76]) lies within the range of two standard deviations.

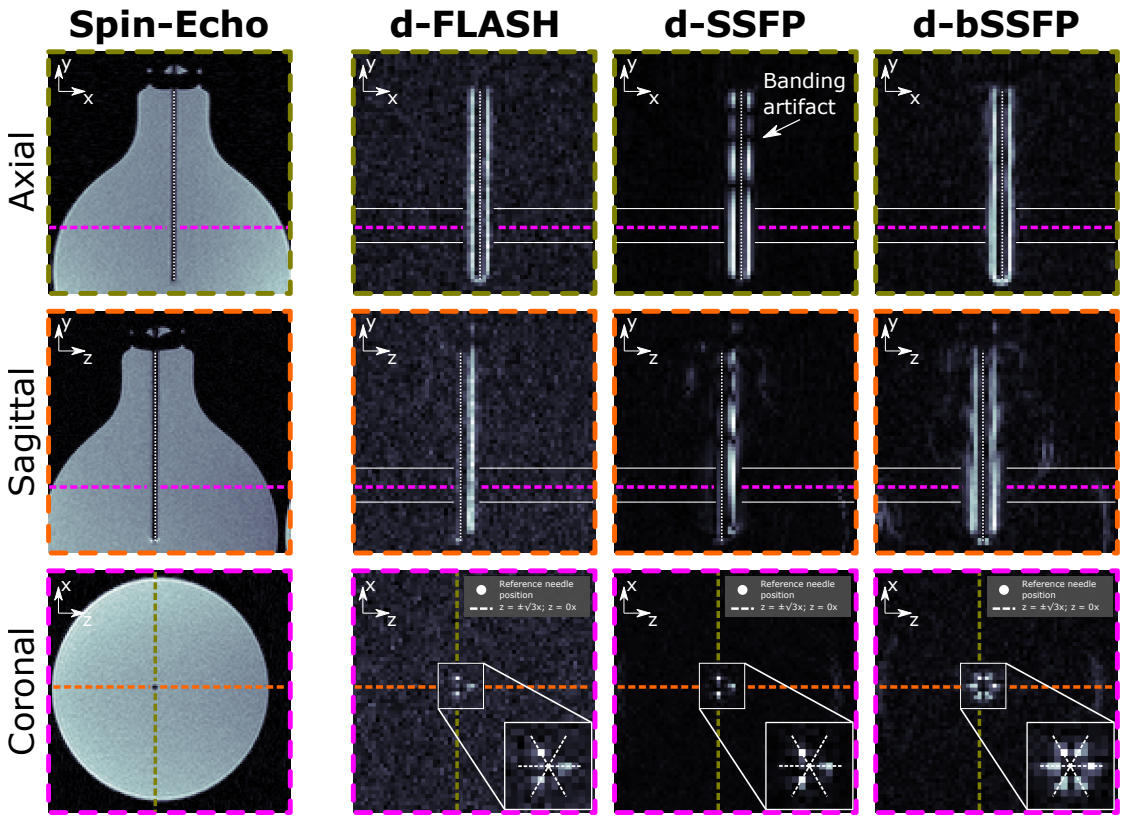

Figure 4.2: Images with d-FLASH, d-SSFP, and d-bSSFP contrast show a needle (diameter: 20-gauge, material: Inconel), placed in a water phantom orthogonal to $\vec{B}_0$. Additionally, a reference spin-echo image is shown. The needle artifact is shown in the xy-plane, zy-plane, and zx-plane as defined in Fig. 2.5. The needle axis (extracted from the SE reference) is indicated by the dotted white line. For the zx-plane, an additional zoomed view is shown for the dephased GRE images. To depict the positive needle artifact in the dephased GRE images, the xy-plane view is slightly shifted in z-direction compared to the reference image. White solid lines in the xy-plane and zy-plane images indicate a slab of 10 slices for which the average artifact signal was calculated (see Table 4.2). Figure reproduced from Faust et al. [2].

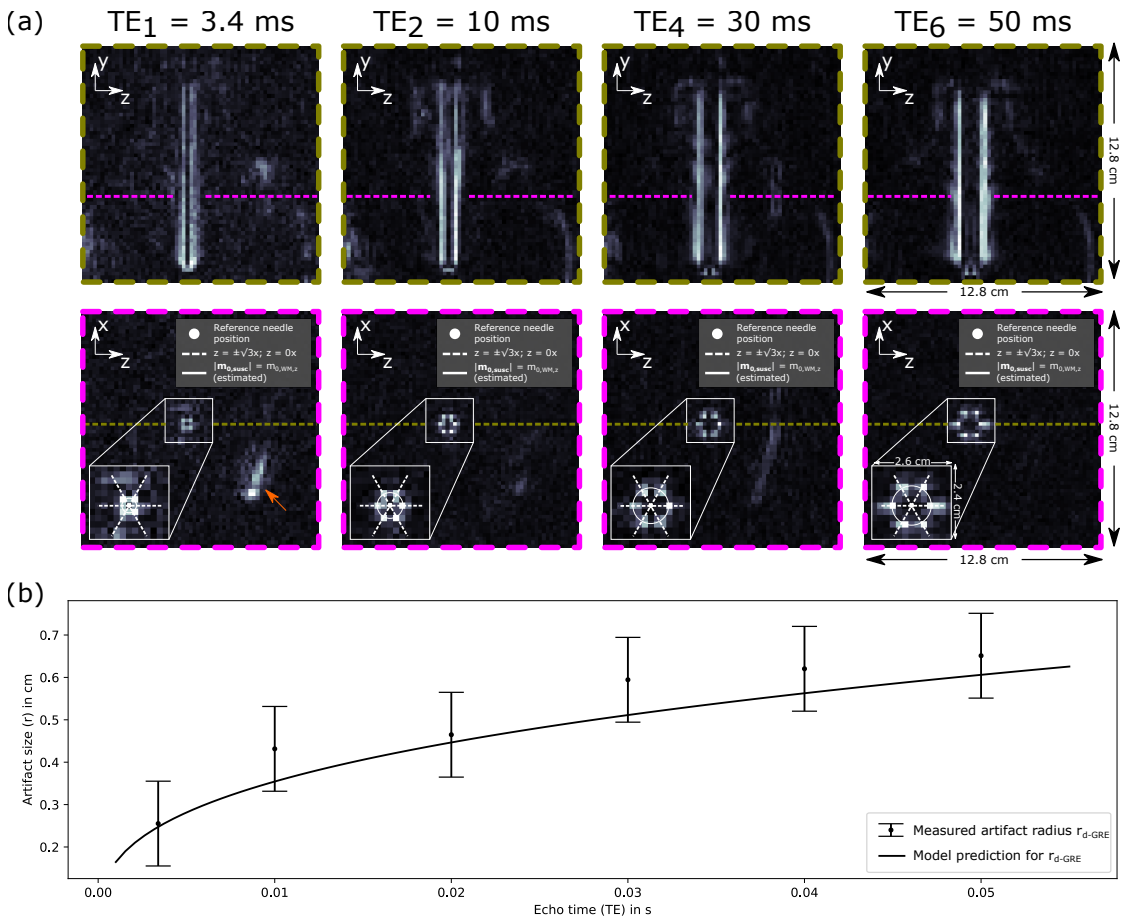

Figure 4.3: Investigation of the d-bSSFP positive contrast artifact generated by a needle in a water phantom for six different echo times T_{E}: $T_{\mathrm{E},1} = 3.4\,\mathrm{ms}$, $T_{\mathrm{E},2} = 10\,\mathrm{ms}$, $T_{\mathrm{E},3} = 20\,\mathrm{ms}$, $T_{\mathrm{E},4} = 30\,\mathrm{ms}$, $T_{\mathrm{E},5} = 40\,\mathrm{ms}$, and $T_{\mathrm{E},6} = 50\,\mathrm{ms}$. (a) For $T_{\mathrm{E},1}$, $T_{\mathrm{E},2}$, $T_{\mathrm{E},4}$ and $T_{\mathrm{E},6}$, the needle artifact is shown in the yz-plane and zx-plane as defined in Fig. 2.5, with an additional zoomed view on the artifact for the zx-plane view. While the background signal in the water phantom appears largely suppressed, some stripe-like artifacts emerge that seem unrelated to the needle (orange arrow). (b) For each investigated T_{E}, the radius of the needle artifact $r_{\text{d-GRE}}$ is measured (average distance between the reference needle position and pixels of maximum signal, assumed measurement uncertainty of half a pixel) and plotted together with the modeled radius from Eq. 2.74. Figure adapted from Faust et al. [2].

Table 4.2: Comparative overview of the investigated dephased GRE imaging techniques (d-FLASH, d-SSFP, and d-bSSFP). The different techniques were compared regarding the exhibited positive artifact symmetry, the sensitivity to banding artifacts, and the maximum as well as the cumulated artifact signal magnitude (normalized to d-SSFP magnitude, given with standard deviation). The different steady-state magnetizations (coherent steady-state for d-SSFP and incoherent steady-state for d-FLASH) make the signal magnitude ratio tissue-dependent when comparing d-FLASH with d-SSFP, rendering a general prediction of the signal magnitude ratio not feasible (see Section 2.3.2). Table reproduced from Faust et al. [4].

	d-FLASH	**d-SSFP**	**d-bSSFP**
Symmetry	Axial	Axial	Point
Sensitive to banding artifacts	No	Yes	No
Maximum artifact magnitude (normalized to d-SSFP)	Model: n.a.	Model: 1	Model: 0.64
	Exp.: 0.19 ± 0.04	Exp.: 1.0 ± 0.1	Exp.: 0.56 ± 0.09
Cumulated artifact magnitude (normalized to d-SSFP)	Model: n.a.	Model: 1	Model: 1.27
	Exp.: 0.19 ± 0.01	Exp.: 1.00 ± 0.04	Exp.: 1.13 ± 0.07

In Table 4.2, the findings comparing the three investigated contrast types (concerning artifact symmetry, sensitivity to banding artifacts, as well as the theoretically anticipated versus measured signal magnitude) are again presented in summary.

4.2 Forward model-based 3D needle localization using a baseline-subtracted FLASH acquisition

The proposed forward model-based 3D needle localization method was investigated according to Section 3.2. In Section 4.2.1, needle localization results for the evaluated ex-vivo study and the in-vivo demonstration case are reported. The result of the retrospective demonstration of ASP is described in Section 4.2.2.

4.2.1 Needle localization

In Fig. 4.4, the accuracy of the localization in terms of the defined metrics for the conducted ex-vivo study is displayed as boxplots. Medians ($\pm$ median absolute deviation) for the localization are presented in Table 4.3a for the ex-vivo study. For better interpretability, accuracy values worse than a set performance threshold of $\widetilde{\Delta s} > 1.0\,\mathrm{cm}$ were marked gray in the table. For initial parameter set 1, a median tip localization accuracy of $\widetilde{\Delta s} \leq 0.8\,\mathrm{cm}$ could be reached for as few as 5 acquired k-space spokes, allowing for a combined acquisition and localization time of $t_{\mathrm{acq}} + t_{\mathrm{loc}} < 0.2\,\mathrm{s}$. For initial parameter set 2, a similar accuracy for $\widetilde{\Delta s}$ could be reached for 16 ($t_{\mathrm{acq}} + t_{\mathrm{loc}} < 0.4\,\mathrm{s}$), 32 ($t_{\mathrm{acq}} + t_{\mathrm{loc}} < 0.8\,\mathrm{s}$) and 64 ($t_{\mathrm{acq}} + t_{\mathrm{loc}} < 1.4\,\mathrm{s}$) acquired k-space spokes. For 5 k-space spokes, median tip localization accuracy decreased below the set performance

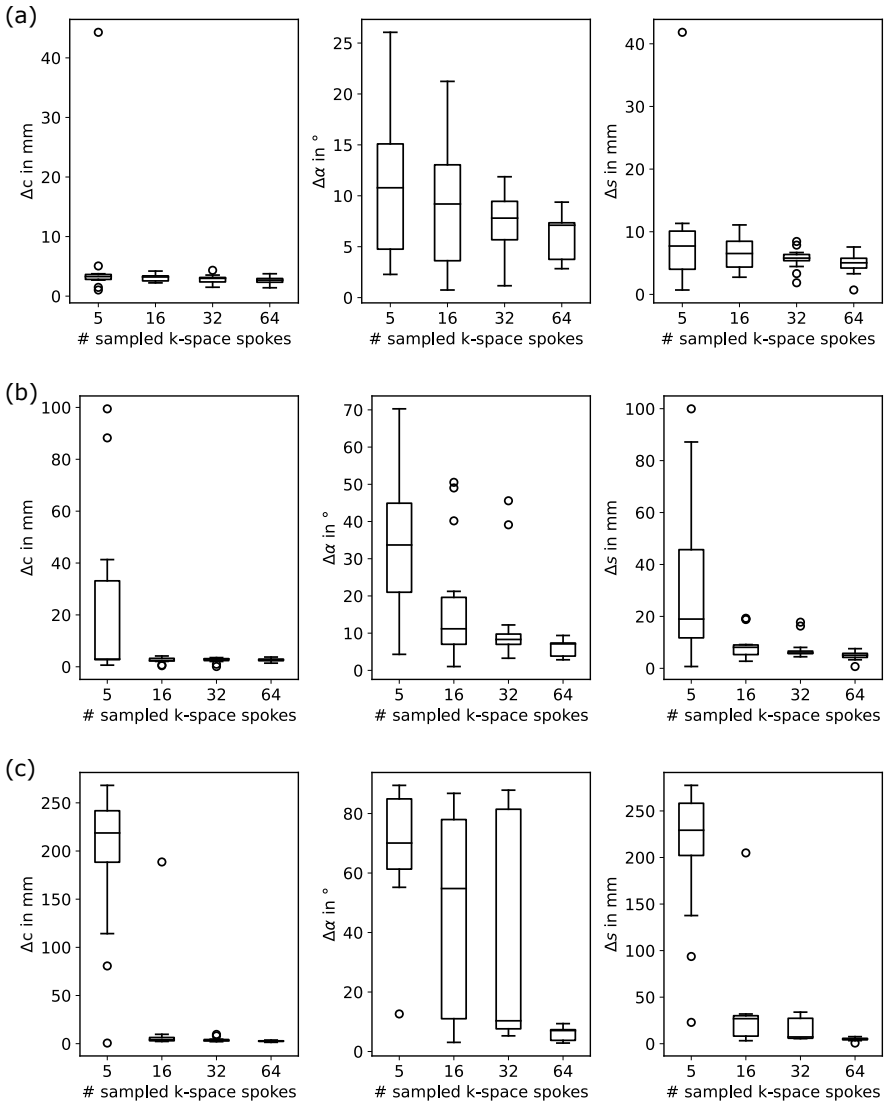

Figure 4.4: Performance (metrics Δc, $\Delta \alpha$, Δs) of the proposed needle localization algorithm for the conducted ex-vivo study with different sets of initial parameters for the model optimization: (a) Initial parameter set 1 – angles shifted by $15°$, centroid shifted by $3.2\,\mathrm{cm}$; (b) Initial parameter set 2 – angles shifted by $30°$, centroid shifted by $6.4\,\mathrm{cm}$; (c) Initial parameter set 3 – angles shifted by $60°$, centroid shifted by $12.8\,\mathrm{cm}$ (= FOV/2). Each metric was evaluated for a localization from 5, 16, 32 and 64 radial k-space spokes. The boxes represent the interquartal range (IQR), with whiskers extending to 1.5 times the IQR. Outliers are shown as circles, and medians are marked by black crosslines. Note the different vertical scales in (a), (b) and (c).

Table 4.3: Accuracy of needle localization with the investigated method from 5, 16, 32 and 64 acquired k-space spokes, depending on the initial set of optimization parameters. For each defined set of initial optimization parameters, the median ($\pm$ the median absolute deviation) of the achieved accuracy was calculated for the introduced metrics ($\widetilde{\Delta c}$), ($\widetilde{\Delta \alpha}$) and ($\widetilde{\Delta s}$) and the mean runtime of the localization algorithm ($\bar{t}_{\mathrm{loc}}$) was determined. For localizations with an achieved accuracy worse than a threshold of $\widetilde{\Delta s} > 1.0\,\mathrm{cm}$, cells are marked in gray.

Number of spokes / **Initial optimization parameters**	*5 spokes*	*16 spokes*	*32 spokes*	*64 spokes*
(a) Ex-vivo study (n = 14)				
Initial parameter set 1	$\widetilde{\Delta c}$ = (0.33 ± 0.04) cm $\widetilde{\Delta \alpha}$ = (10.79 ± 5.81)° $\widetilde{\Delta s}$ = (0.77 ± 0.35) cm $\overline{t_{loc}}$ = (0.08 ± 0.01) s	$\widetilde{\Delta c}$ = (0.32 ± 0.03) cm $\widetilde{\Delta \alpha}$ = (9.19 ± 4.95)° $\widetilde{\Delta s}$ = (0.65 ± 0.21) cm $\overline{t_{loc}}$ = (0.12 ± 0.01) s	$\widetilde{\Delta c}$ = (0.30 ± 0.03) cm $\widetilde{\Delta \alpha}$ = (7.81 ± 1.93)° $\widetilde{\Delta s}$ = (0.58 ± 0.06) cm $\overline{t_{loc}}$ = (0.22 ± 0.02) s	$\widetilde{\Delta c}$ = (0.27 ± 0.03) cm $\widetilde{\Delta \alpha}$ = (7.11 ± 1.77)° $\widetilde{\Delta s}$ = (0.50 ± 0.09) cm $\overline{t_{loc}}$ = (0.34 ± 0.02) s
Initial parameter set 2	$\widetilde{\Delta c}$ = (0.30 ± 0.11) cm $\widetilde{\Delta \alpha}$ = (33.7 ± 12.87)° $\widetilde{\Delta s}$ = (1.90 ± 0.81) cm $\overline{t_{loc}}$ = (0.08 ± 0.01) s	$\widetilde{\Delta c}$ = (0.24 ± 0.06) cm $\widetilde{\Delta \alpha}$ = (11.17 ± 6.41)° $\widetilde{\Delta s}$ = (0.81 ± 0.26) cm $\overline{t_{loc}}$ = (0.14 ± 0.02) s	$\widetilde{\Delta c}$ = (0.30 ± 0.03) cm $\widetilde{\Delta \alpha}$ = (8.31 ± 1.43)° $\widetilde{\Delta s}$ = (0.59 ± 0.05) cm $\overline{t_{loc}}$ = (0.27 ± 0.04) s	$\widetilde{\Delta c}$ = (0.27 ± 0.03) cm $\widetilde{\Delta \alpha}$ = (7.11 ± 1.77)° $\widetilde{\Delta s}$ = (0.50 ± 0.09) cm $\overline{t_{loc}}$ = (0.41 ± 0.06) s
Initial parameter set 3	$\widetilde{\Delta c}$ = (21.87 ± 2.93) cm $\widetilde{\Delta \alpha}$ = (70.08 ± 9.67)° $\widetilde{\Delta s}$ = (22.93 ± 3.01) cm $\overline{t_{loc}}$ = (0.08 ± 0.01) s	$\widetilde{\Delta c}$ = (0.42 ± 0.15) cm $\widetilde{\Delta \alpha}$ = (54.79 ± 31.27)° $\widetilde{\Delta s}$ = (2.69 ± 1.00) cm $\overline{t_{loc}}$ = (0.21 ± 0.04) s	$\widetilde{\Delta c}$ = (0.31 ± 0.05) cm $\widetilde{\Delta \alpha}$ = (10.33 ± 3.29)° $\widetilde{\Delta s}$ = (0.73 ± 0.17) cm $\overline{t_{loc}}$ = (0.39 ± 0.06) s	$\widetilde{\Delta c}$ = (0.27 ± 0.03) cm $\widetilde{\Delta \alpha}$ = (7.05 ± 1.77)° $\widetilde{\Delta s}$ = (0.50 ± 0.09) cm $\overline{t_{loc}}$ = (0.58 ± 0.08) s
(b) In-vivo proof-of-principle experiment				
Initial parameter set 1	Δc = 0.9 cm Δα = 7.2° Δs = 1.2 cm t_{loc} = 0.06 s	Δc = 0.8 cm Δα = 4.5° Δs = 0.9 cm t_{loc} = 0.11 s	Δc = 0.7 cm Δα = 3.6° Δs = 0.8 cm t_{loc} = 0.15 s	Δc = 0.5 cm Δα = 10.2° Δs = 0.9 cm t_{loc} = 0.3 s
Initial parameter set 2	Δc = 5.1 cm Δα = 42.4° Δs = 6.9 cm t_{loc} = 0.05 s	Δc = 0.7 cm Δα = 49.5° Δs = 3.8 cm t_{loc} = 0.11 s	Δc = 0.6 cm Δα = 44.0° Δs = 3.4 cm t_{loc} = 0.25 s	Δc = 0.5 cm Δα = 10.2° Δs = 0.9 cm t_{loc} = 0.3 s

threshold with $\widetilde{\Delta s} = 1.9\,\mathrm{cm}$. For initial parameters set 3, a localization above the set threshold was possible from 32 and 64 k-space spokes (with $\widetilde{\Delta s} < 0.8\,\mathrm{cm}$). The achieved localization accuracy, broken down by the angular orientation of the respective needle orientation for the individual samples in the ex-vivo study dataset is provided in Fig. A.1.

Figure 4.5 shows an example localization from the ex-vivo dataset from 5, 16, 32 and 64 acquired k-space spokes using (a) set 1 and (b) set 3 of initial optimization parameters. The image columns show localizations from different numbers of acquired k-space lines (n_{spokes} = 5; 16; 32; 64). The first row shows the image-reconstructed acquired subtraction k-space as maximum intensity projection (MIP). The needle axes according to the ground truth annotation (blue dashed line), initial k-space model parameters (red dashed line) and the optimized parameters (green dashed line) are shown. The second row shows the image-reconstructed modeled k-space with the optimized k-space model parameters. The image reconstructions serve visualization purposes only as no image reconstruction is required for the investigated k-space-based localization. For initial parameter set 1, an accuracy of $\Delta s \leq 0.5\,\mathrm{cm}$ was reached for localizations from all investigated numbers of k-space spokes. For the initial parameter set 3, reconstructed images of the k-space model show the increased misalignment of the initial artifact model axis and the true artifact axis compared to the initial parameter set 1. The best localization accuracy of $\Delta s = 0.3\,\mathrm{cm}$ was achieved for the optimization using 64 k-space spokes. While the accuracy of the positional fit was in the same order of magnitude for all numbers of used k-space lines ($\Delta c \leq 0.3\,\mathrm{cm}$), the performance of the angular optimization decreased for less than 64 k-space spokes ($\Delta\alpha \geq 70°$), consequently leading to a large discrepancy for the tip distance ($\Delta s \geq 2.3\,\mathrm{cm}$).

In Fig. 4.6, the cost function of the angular fit for the example needle insertion from Fig. 4.5 is displayed for the localization from all investigated numbers of acquired k-space lines. Corresponding to Fig. 4.5, optimization paths are shown for the initial parameter sets 1 and 3. Global minima of the optimization surfaces are indicated, as well as the initial and final angular optimization parameters and the ground truth (annotated) angular orientation. Optimization starting from initial parameter set 1 successfully reaches the angular global minimum for all investigated numbers of k-space lines. Optimization with set 2 seemingly gets stuck in local minima for 5, 16 and 32 k-space spokes and cannot reach the global minimum, which appears close to the true angular parameters. It is only for 64 spokes that the angular cost function appears convex enough for the optimization to find the global minimum with the initial parameter set 3.

The calculated metrics for the in-vivo proof-of-principle demonstration case are given in Table 4.3b. For initial parameter set 1, localization accuracy was assessed to be within the set performance threshold for 16, 32 and 64 k-space spokes ($\Delta s \leq 0.9\,\mathrm{cm}$) and below the set threshold (with $\Delta s = 1.2\,\mathrm{cm}$) for the 5 spoke case (grayed-out cell). $\Delta\alpha$ is largest ($\Delta\alpha = 10.2°$) for the localization from 64 spokes (see discussion). For the initial parameter set 2, localization within the performance threshold was only possible from 64 spokes ($\Delta s = 0.9\,\mathrm{cm}$).

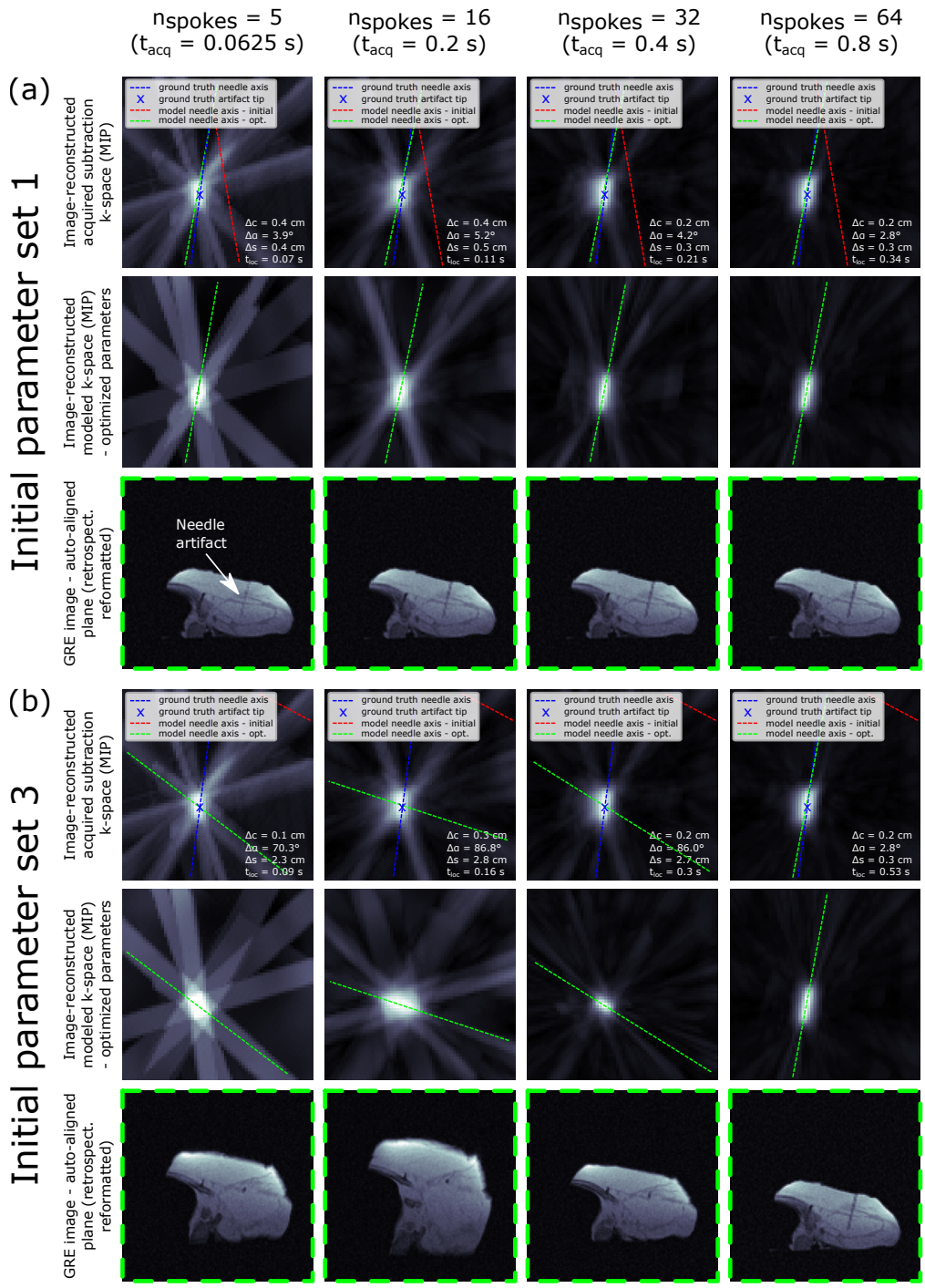

Figure 4.5: Example localization (with $\theta = 96.4°$ and $\phi = 103.8°$) from the acquired ex-vivo dataset with two sets of initial model optimization parameters: (a) angles shifted by $15°$, centroid shifted by $3.2\,\mathrm{cm}$ (set 1); (b) angles shifted by $60°$, centroid shifted by $12.8\,\mathrm{cm}$ (set 3).

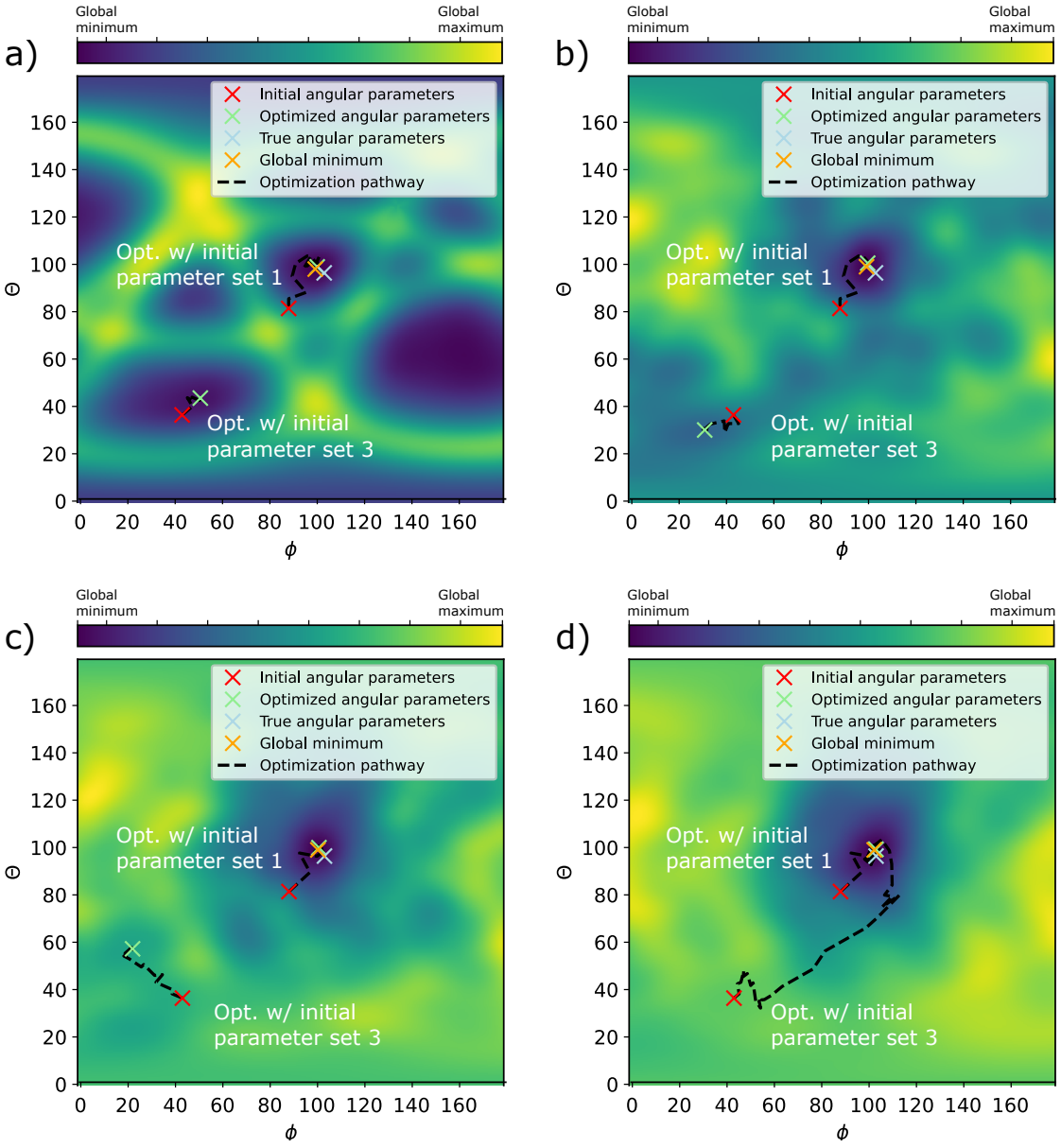

Figure 4.6: Visualization of the cost function for the performed angular optimization in the example of Fig. 4.5 (fixed artifact model length l_c at ground truth value for needle insertion depth l) with the two angles ϕ and θ. For a localization from (a) 5, (b) 16, (c) 32 and (d) 64 k-space lines, the optimization pathways are shown with the initial optimization parameter sets 1 and 3.

4.2.2 Automatic slice alignment

The third row of the two subfigures in Fig. 4.5 respectively displays reformatted 2D slices (slice thickness = $8\,\mathrm{mm}$) from the acquired 3D reference scan with the imaging plane aligned with the fitted needle trajectory (retrospective ASP). For localizations with the initial parameters set 1 from all investigated n_{spokes}, the needle artifact was visible for the full needle insertion depth in the realigned image plane. For localizations with the initial parameters set 3, the needle artifact is only fully visible in the automatically aligned slice for the localization from 64 k-space spokes (the needle only "punctures" the slice for the localizations from less spokes).

Figure 4.7 displays the proof-of-principle demonstration of an in-vivo needle localization in the porcine animal model. The image-reconstructed acquired subtraction k-space with an overlay of the true artifact axis, the initial and the fitted modeled artifact axes are shown. Some areas of hyperintense signal that appear unrelated to the needle artifact are visible in the reconstructed subtraction images (see discussion). Reformatted slices from a 3D reference scan show an imaging plane aligned with the initial and the fitted model. While the needle artifact is not visible in the initially misaligned slice, it is fully visible in the realigned image plane for the localization from all investigated numbers of k-space spokes, including the 5 spoke case.

4.3 3D needle localization using dephased FLASH contrast and CNN-based postprocessing

The proposed CNN-based 3D needle localization method was evaluated according to Section 3.3. In Section 4.3.1, needle localization results for the evaluated ex-vivo study and in-vivo proof-of-principle experiment are reported. The results of the retrospective demonstration of ASP are described in Section 4.3.2.

4.3.1 Needle localization

In Fig. 4.8, the results for the metrics $\Delta\alpha$ and Δs, calculated for the investigated ex-vivo test dataset, are depicted as boxplots (for localization from 6434, 256, 64, and 32 spokes; binned for the inclination angle). The medians $\widetilde{\Delta\alpha}$ and $\widetilde{\Delta s}$ of the employed metrics, calculated for the investigated ex-vivo test dataset, are presented in Table 4.4. Medians ($\pm$ the median absolute deviation) are reported for localizations from images reconstructed with all evaluated undersampling factors and samples binned based on the needle inclination angle θ. On the employed PC hardware, the performed retrospective localizations with the investigated algorithm took between $2\,\mathrm{s}$ and $41\,\mathrm{s}$ per acquisition. Reconstruction times for 3 reconstructed coil channels were $t_{\text{recon}} = 39.4\,\mathrm{s}$ for 6434 spokes, $t_{\text{recon}} = 1.9\,\mathrm{s}$ for 256 spokes, $t_{\text{recon}} = 1.2\,\mathrm{s}$ for 128 spokes, $t_{\text{recon}} = 0.8\,\mathrm{s}$ for 64 spokes, $t_{\text{recon}} = 0.6\,\mathrm{s}$ for 32 spokes and $t_{\text{recon}} = 0.5\,\mathrm{s}$ for 16 spokes. The processing time of the needle localization algorithm was below $1\,\mathrm{s}$. Acquisition times t_{acq} for the samples from the ex-vivo study (n_{spokes} times T_{R}) ranged from $t_{\text{acq}}(n_{\text{spokes}} = 6434) = 80.43\,\mathrm{s}$

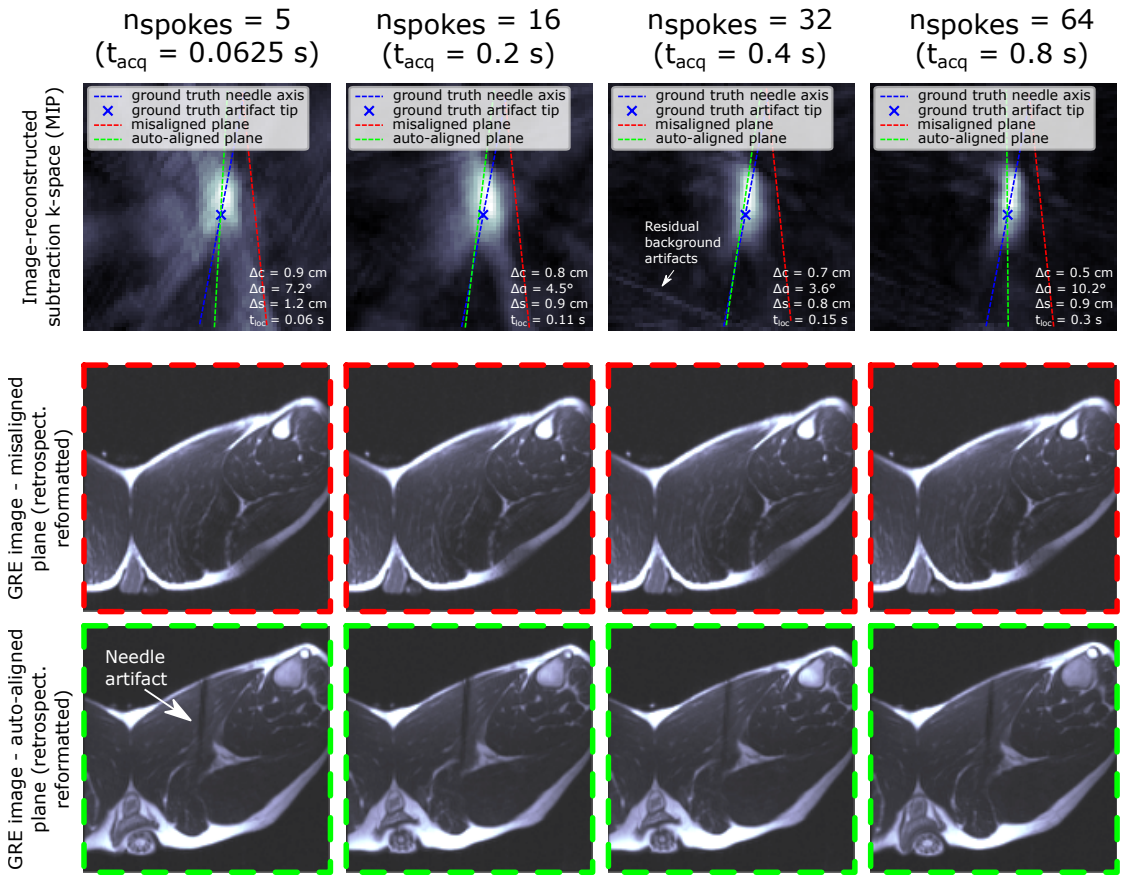

Figure 4.7: In-vivo proof-of-principle demonstration of automatic slice alignment using the investigated forward model-based localization algorithm. The first row of the image shows the reconstructed subtraction k-space (only for demonstration purposes, not part of the localization) for 5, 16, 32 and 64 acquired k-space spokes. Ground truth needle orientation and needle artifact tip, as extracted from the reference scan, are indicated with a blue line and cross. The needle trajectory as determined using the proposed localization algorithm is indicated by the green line and the initially misaligned axis with a red line. The second and third row show the initially misaligned as well as an automatically positioned 2D image slice (thickness = $8\,\mathrm{mm}$) based on the performed needle localization (auto-reformatted from 3D reference scan).

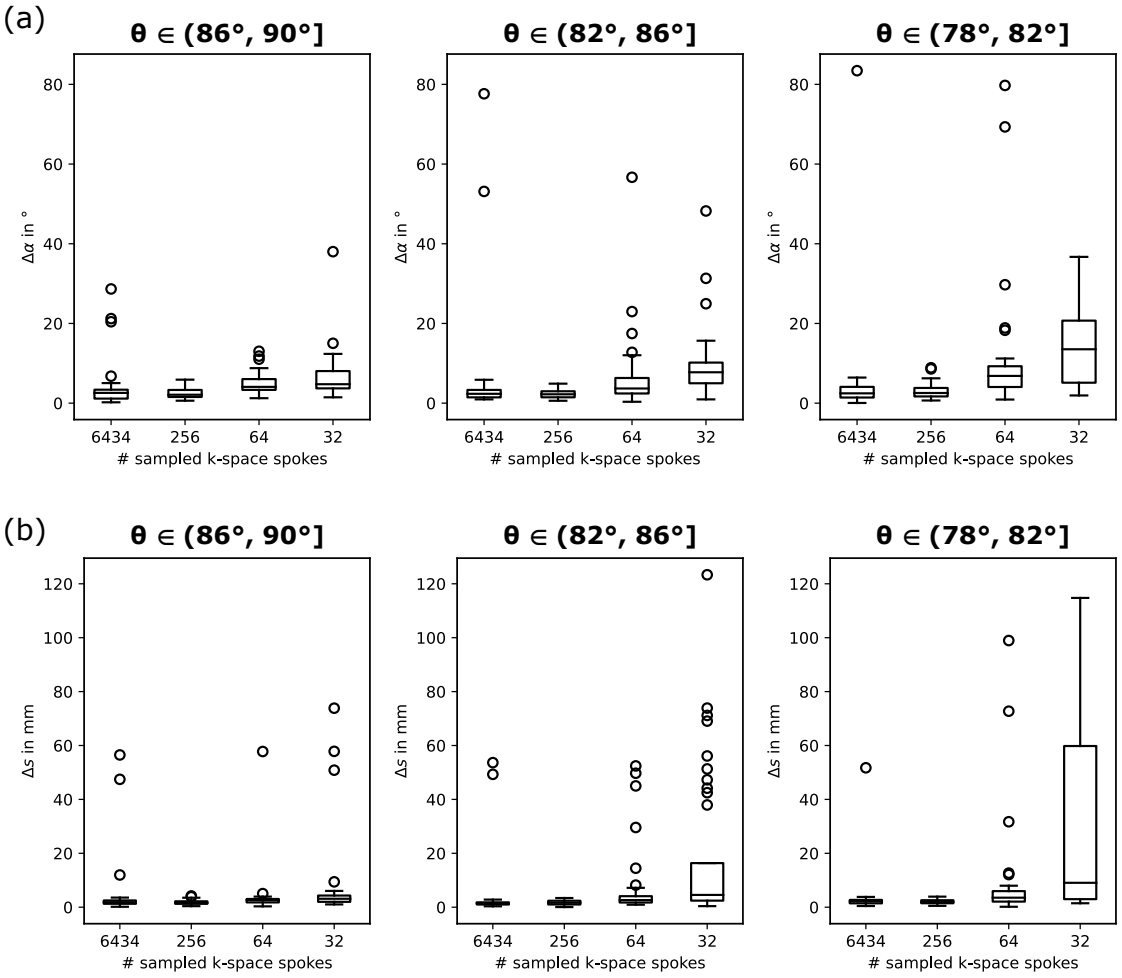

Figure 4.8: Performance evaluation investigating the proposed CNN-based rapid 3D needle localization technique for the conducted ex-vivo study. Samples in the test set were binned into three subsets of different needle inclination angles θ and the measured values for $\Delta\alpha$ and Δs are presented as boxplots for localizations from images reconstructed from different numbers of sampled k-space spokes. The boxes represent the IQR, with whiskers extending to 1.5 times the IQR. Outliers are shown as circles, and medians are marked by black crosslines. Figure reproduced from Faust et al. [4].

Table 4.4: Accuracy evaluation for the performed ex-vivo study analyzing the proposed CNN-based rapid 3D needle localization. Samples from the test set were binned into 3 subsets of different needle inclination angles θ, each containing a different number n of samples. Medians ($\pm$ the median absolute deviation) for the introduced metrics $\widetilde{\Delta\alpha}$ and $\widetilde{\Delta s}$ are provided for each subset and localizations from different numbers of acquired k-space spokes. The cells of the table were colored to highlight differences in $\widetilde{\Delta s}$: white $\widehat{=}\ (4\,\mathrm{mm} > \widetilde{\Delta s})$; light grey $\widehat{=}\ (8\,\mathrm{mm} > \widetilde{\Delta s} \geq 4\,\mathrm{mm})$; dark grey $\widehat{=}\ (\widetilde{\Delta s} \geq 8\,\mathrm{mm})$. Table adapted from Faust et al. (2024) [4].

	6434 spokes (fully sampled) $t_{acq} + t_{loc} \approx 121$ s	**256 spokes** $t_{acq} + t_{loc} \approx 6$ s	**128 spokes** $t_{acq} + t_{loc} \approx 4$ s	**64 spokes** $t_{acq} + t_{loc} \approx 3$ s	**32 spokes** $t_{acq} + t_{loc} \approx 2$ s	**16 spokes** $t_{acq} + t_{loc} \approx 2$ s
$n = 36$ $\theta \in (86°,90°]$	$\widetilde{\Delta\alpha} = (2.6 \pm 1.4)°$ $\widetilde{\Delta s} = (1.9 \pm 0.6)$ mm	$\widetilde{\Delta\alpha} = (2.1 \pm 0.8)°$ $\widetilde{\Delta s} = (1.6 \pm 0.5)$ mm	$\widetilde{\Delta\alpha} = (2.8 \pm 0.7)°$ $\widetilde{\Delta s} = (1.9 \pm 0.5)$ mm	$\widetilde{\Delta\alpha} = (4.1 \pm 1.4)°$ $\widetilde{\Delta s} = (2.6 \pm 0.7)$ mm	$\widetilde{\Delta\alpha} = (4.7 \pm 2.1)°$ $\widetilde{\Delta s} = (3.1 \pm 1.2)$ mm	$\widetilde{\Delta\alpha} = (9.5 \pm 4.7)°$ $\widetilde{\Delta s} = (4.7 \pm 3.0)$ mm
$n = 40$ $\theta \in (82°,86°]$	$\widetilde{\Delta\alpha} = (2.3 \pm 0.9)°$ $\widetilde{\Delta s} = (1.5 \pm 0.5)$ mm	$\widetilde{\Delta\alpha} = (2.2 \pm 0.8)$ mm $\widetilde{\Delta s} = (1.7 \pm 0.7)°$	$\widetilde{\Delta\alpha} = (3.0 \pm 1.4)°$ $\widetilde{\Delta s} = (1.8 \pm 0.8)$ mm	$\widetilde{\Delta\alpha} = (3.7 \pm 1.6)°$ $\widetilde{\Delta s} = (2.6 \pm 1.1)$ mm	$\widetilde{\Delta\alpha} = (7.7 \pm 2.6)°$ $\widetilde{\Delta s} = (4.6 \pm 2.5)$ mm	$\widetilde{\Delta\alpha} = (15.6 \pm 9.3)°$ $\widetilde{\Delta s} = (13.7 \pm 12.7)$ mm
$n = 33$ $\theta \in (78°,82°]$	$\widetilde{\Delta\alpha} = (2.5 \pm 1.1)°$ $\widetilde{\Delta s} = (2.2 \pm 0.7)$ mm	$\widetilde{\Delta\alpha} = (2.5 \pm 1.1)°$ $\widetilde{\Delta s} = (1.9 \pm 0.5)$ mm	$\widetilde{\Delta\alpha} = (5.2 \pm 3.0)°$ $\widetilde{\Delta s} = (2.6 \pm 1.1)$ mm	$\widetilde{\Delta\alpha} = (6.8 \pm 2.7)°$ $\widetilde{\Delta s} = (3.5 \pm 1.5)$ mm	$\widetilde{\Delta\alpha} = (13.5 \pm 7.7)°$ $\widetilde{\Delta s} = (9.1 \pm 7.2)$ mm	$\widetilde{\Delta\alpha} = (30.8 \pm 9.0)°$ $\widetilde{\Delta s} = (53.0 \pm 17.9)$ mm

to $t_{\mathrm{acq}}(n_{\mathrm{spokes}} = 16) = 0.2\,\mathrm{s}$. The median accuracy of the binned samples decreases as the number of spokes is reduced and the needle trajectories become more aligned with $\vec{B}_0$, and, therefore, also with $\vec{G}_{\mathrm{WM}}$. For inclination angles $\theta = (86°, 90°]$, values of $\widetilde{\Delta\alpha} = (2.6 \pm 1.4)°$ and $\widetilde{\Delta s} = (1.9 \pm 0.6)\,\mathrm{mm}$ were found for localizations using 6434 k-space spokes, as well as $\widetilde{\Delta\alpha} = (9.5 \pm 4.7)°$ and $\widetilde{\Delta s} = (4.7 \pm 3.0)\,\mathrm{mm}$ for localizations using 16 spokes. For, e.g., localizations from 64 spokes, the computed median accuracy decreased from $\widetilde{\Delta\alpha} = (4.1 \pm 1.4)°$ and $\widetilde{\Delta s} = (2.6 \pm 0.7)\,\mathrm{mm}$ for insertion angles $\theta = (86°, 90°]$ to $\widetilde{\Delta\alpha} = (6.8 \pm 2.7)°$ and $\widetilde{\Delta s} = (3.5 \pm 1.5)\,\mathrm{mm}$ for insertion angles $\theta = (78°, 82°]$.

In Figure 4.9, two localizations from the assessed ex-vivo test dataset are depicted, using 6434, 256, 64, and 32 sampled k-space spokes. The first row of the images displays a manually selected slice from the acquired (undersampled) 3D WM image, showing the WM needle artifact. The second row presents the 3D d-FLASH image as MIP with the CNN localization overlay. In the example of Fig. 4.9a, the needle was inserted at an inclination angle of $\theta = 88.1°$, nearly orthogonal to $\vec{B}_0$. Despite the higher noise level, the WM needle artifact remains discernible even in the images reconstructed from fewer k-space spokes. With as few as 32 k-space spokes, localization accuracies of $\Delta\alpha \leq 3.4°$ and $\Delta s \leq 2.5\,\mathrm{mm}$ could be achieved. In the example of Fig. 4.9b, the needle was inserted with an inclination angle of $\theta = 78.2°$ with $\vec{B}_0$. The visibility of the WM needle artifact diminishes for lower numbers of sampled k-space spokes. At 32 spokes, the needle artifact becomes visually nearly indistinguishable from the background noise in the d-FLASH image. While the needle was localized with accuracies of $\Delta\alpha \leq 3.8°$ and $\Delta s \leq 2.2\,\mathrm{mm}$ for image reconstructions from 6434, 256, and 64 sampled spokes, localization accuracy was diminished for the 32 spokes reconstruction, with $\Delta\alpha = 13.9°$ and $\Delta s = 8.3\,\mathrm{mm}$.

In Table 4.5, the localization success rate (a successful localization was characterized by Δs being below a specified threshold, refer to Section 3.3.2) is reported for the ex-vivo test dataset. A lower success rate was found for localizations using a lower number of sampled k-space spokes, as well as for needle insertions increasingly parallel to the direction of $\vec{B}_0$ and G_{WM}. For needle inclination angles $\theta \in (86°, 90°]$, a success rate of $\geq 72\,\%$ was reached with a set

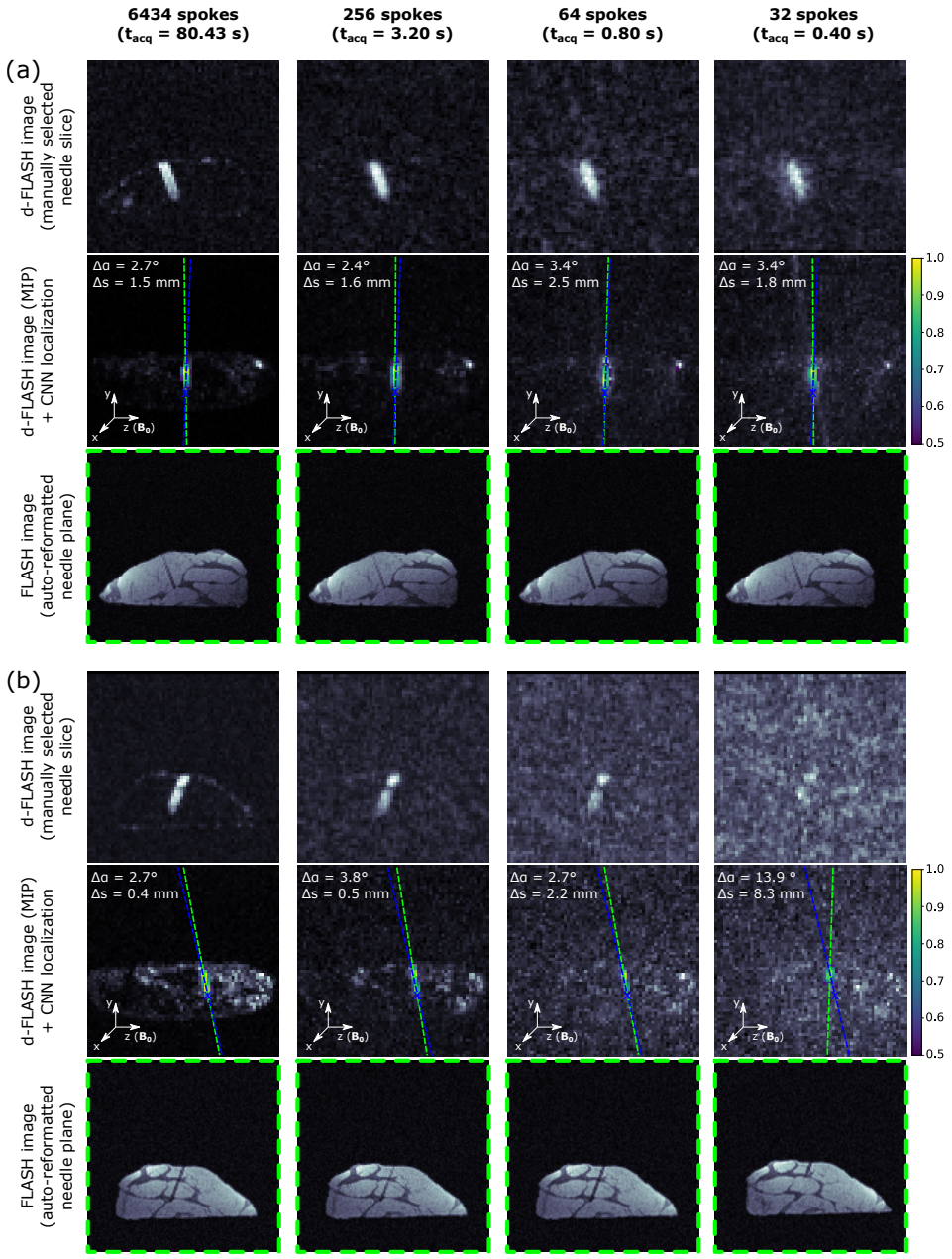

Figure 4.9: Performance evaluation for two example needle insertions from the ex-vivo test dataset with needle inclination angles of $\theta = 88.1°$ (a) and $\theta = 78.2°$ (b) relative to $\vec{B}_0$, investigating the proposed CNN-based rapid 3D needle localization technique. Blue cross corresponds to ground truth needle tip, blue dashed line corresponds to ground truth needle axis, green dashed line corresponds to predicted needle axis. Figure adapted from Faust et al. [4].

Table 4.5: Evaluation of the calculated success rate (number of samples with $\Delta s < 4\,\mathrm{mm}$, $\Delta s < 8\,\mathrm{mm}$ or $\Delta s < 12\,\mathrm{mm}$) for the performed ex-vivo study analyzing the proposed CNN-based rapid 3D needle localization. Samples from the test set were binned into 3 subsets of different needle inclination angles θ and success rates were calculated for localizations from different numbers of acquired k-space spokes. The cells of the table were colored to highlight differences in the achieved success rate: white $\widehat{=}$ (success rate $\geq 75\,\%$); light grey $\widehat{=}$ ($75\,\%$ > success rate $\geq 50\,\%$); dark grey $\widehat{=}$ (success rate < $50\,\%$). Table reproduced from Faust et al. [4].

	$\Theta \in [86°, 90°]$					
	Fully sampled	**256 spokes**	**128 spokes**	**64 spokes**	**32 spokes**	**16 spokes**
No. of samples with ($\Delta s < 4$ mm) / total no. of samples	33/36 = 92%	35/36 = 97%	36/36 = 100%	34/36 = 94%	26/36 = 72%	17/36 = 47%
No. of samples with ($\Delta s < 8$ mm) / total no. of samples	33/36 = 92%	36/36 = 100%	36/36 = 100%	35/36 = 97%	32/36 = 89%	24/36 = 67%
No. of samples with ($\Delta s < 12$ mm) / total no. of samples	34/36 = 94%	36/36 = 100%	36/36 = 100%	35/36 = 97%	33/36 = 92%	28/36 = 78%
	$\vartheta \in [82°, 86°]$					
	Fully sampled	**256 spokes**	**128 spokes**	**64 spokes**	**32 spokes**	**16 spokes**
No. of samples with ($\Delta s < 4$ mm) / total no. of samples	38/40 = 95%	40/40 = 100%	35/40 = 88%	29/40 = 72%	18/40 = 45%	12/40 = 30%
No. of samples with ($\Delta s < 8$ mm) / total no. of samples	38/40 = 95%	40/40 = 100%	38/40 = 95%	34/40 = 85%	29/40 = 72%	16/40 = 40%
No. of samples with ($\Delta s < 12$ mm) / total no. of samples	38/40 = 95%	40/40 = 100%	38/40 = 95%	35/40 = 88%	30/40 = 75%	19/40 = 48%
	$\vartheta \in [78°, 82°]$					
	Fully sampled	**256 spokes**	**128 spokes**	**64 spokes**	**32 spokes**	**16 spokes**
No. of samples with ($\Delta s < 4$ mm) / total no. of samples	32/33 = 97%	33/33 = 100%	21/33 = 64%	19/33 = 58%	11/33 = 33%	3/33 = 9%
No. of samples with ($\Delta s < 8$ mm) / total no. of samples	32/33 = 97%	33/33 = 100%	27/33 = 82%	28/33 = 85%	15/33 = 45%	4/33 = 12%
No. of samples with ($\Delta s < 12$ mm) / total no. of samples	32/33 = 97%	33/33 = 100%	28/33 = 85%	28/33 = 85%	18/33 = 55%	6/33 = 18%

threshold of $\Delta s = 4\,\mathrm{mm}$ for localizations from all assessed numbers of sampled k-space spokes ($n_{\mathrm{spokes}1} = 6434$ to $n_{\mathrm{spokes}5} = 32$). For needles inserted at an angle $\theta \in (78°, 82°]$, a success rate of $\geq 82\,\%$ was achieved, setting a threshold of $\Delta s = 8\,\mathrm{mm}$ for localizations from as few as 64 spokes.

In Fig. 4.10, localization results for the in-vivo proof-of-concept needle insertions are depticted. A 20-gauge needle (a) and a 22-gauge needle (b,c) were inserted into the thighs of two pigs, with images captured using a spine and loop coil (a,c) and a spine and flex coil (b). The needles were positioned at angles to $\vec{B}_0$ of $\theta_1 = 87.7°$ (a), $\theta_2 = 88.8°$ (b), and $\theta_3 = 77.6°$ (c). The first row of each subfigure displays a manually chosen slice from the (undersampled) 3D d-FLASH image, showing the needle WM artifact and residual tissue WM artifacts (see discussion in Section 5.2.2). The second row presents the CNN prediction overlaid on a MIP of the d-FLASH image. The third row features a reformatted slice (slice thickness $= 4\,\mathrm{mm}$) from a 3D FLASH/bSSFP reference dataset, selected based on the CNN-based needle localization. Localizations were evaluated from $n_{\mathrm{spokes}1} = 6434$ to $n_{\mathrm{spokes}5} = 32$ k-space spokes. For needles inserted nearly parallel to the transversal plane, localization accuracy from just 32 sampled k-space spokes reached $\Delta\alpha = 3.4°$ and $\Delta s = 1.4\,\mathrm{mm}$ for the insertion shown in Fig. 4.10a, and $\Delta\alpha = 4.1°$ and $\Delta s = 6.9\,\mathrm{mm}$ for the insertion shown in Fig. 4.10b. For the insertion evaluated in Fig. 4.10c, where the needle was angled further away from the transversal plane, an accuracy of $\Delta\alpha = 6.8°$ and $\Delta s = 5.3\,\mathrm{mm}$ was measured for a localization from only 128 sampled spokes. For the localization attempts with 64 and 32 sampled spokes, the algorithm failed to identify the needle correctly.

4.3.2 Automatic slice alignment

For both ex-vivo cases depicted in Fig. 4.9, a 2D slice (slice thickness $= 4\,\mathrm{mm}$) was reformatted from the acquired 3D reference FLASH image, which was aligned with the identified needle axis from the respective localization result to retrospectively evaluate the feasibility of automatic slice alignment following the proposed localization algorithm (picture in third row of the two figure parts). For the example depicted in Fig. 4.9a, the needle artifact is visible for the entire insertion depth of the needle in the automatically chosen slice for localizations from all investigated numbers of sampled k-space spokes. In the example shown in Fig. 4.9b, although the entire needle artifact is visible for localizations from 6434 to 64 k-space spokes, the detected needle axis was too oblique to the ground truth needle needle path for localization from investigated numbers of k-space spokes below 64, causing the needle artifact to be located partially out of the reformatted plane. In particular, the needle artifact is not visible for the needle tip.

For the in-vivo proof-of-principle case depicted in Fig. 4.10a, the needle trajectory was entirely visible in the reformatted d-FLASH 2D image slice for localizations from 6434 down to 64 k-space spokes ($\Delta\alpha \leq 2.2°$; $\Delta s \leq 2.4\,\mathrm{mm}$). The needle axis, as detected by the localization algorithm, had an increased obliqueness to the true needle axis for the localization from 32 k-space spokes, causing the needle artifact to not be visible for part of insertion depth of the needle in the automatically reformatted 2D image plane ($\Delta\alpha = 3.4°$; $\Delta s = 1.4\,\mathrm{mm}$). The artifact at the tip, nevertheless, remained visible in the aligned plane. For the case shown in Fig. 4.10b, the needle artifact is partly visible in all reformatted 2D bSSFP slices. However, the

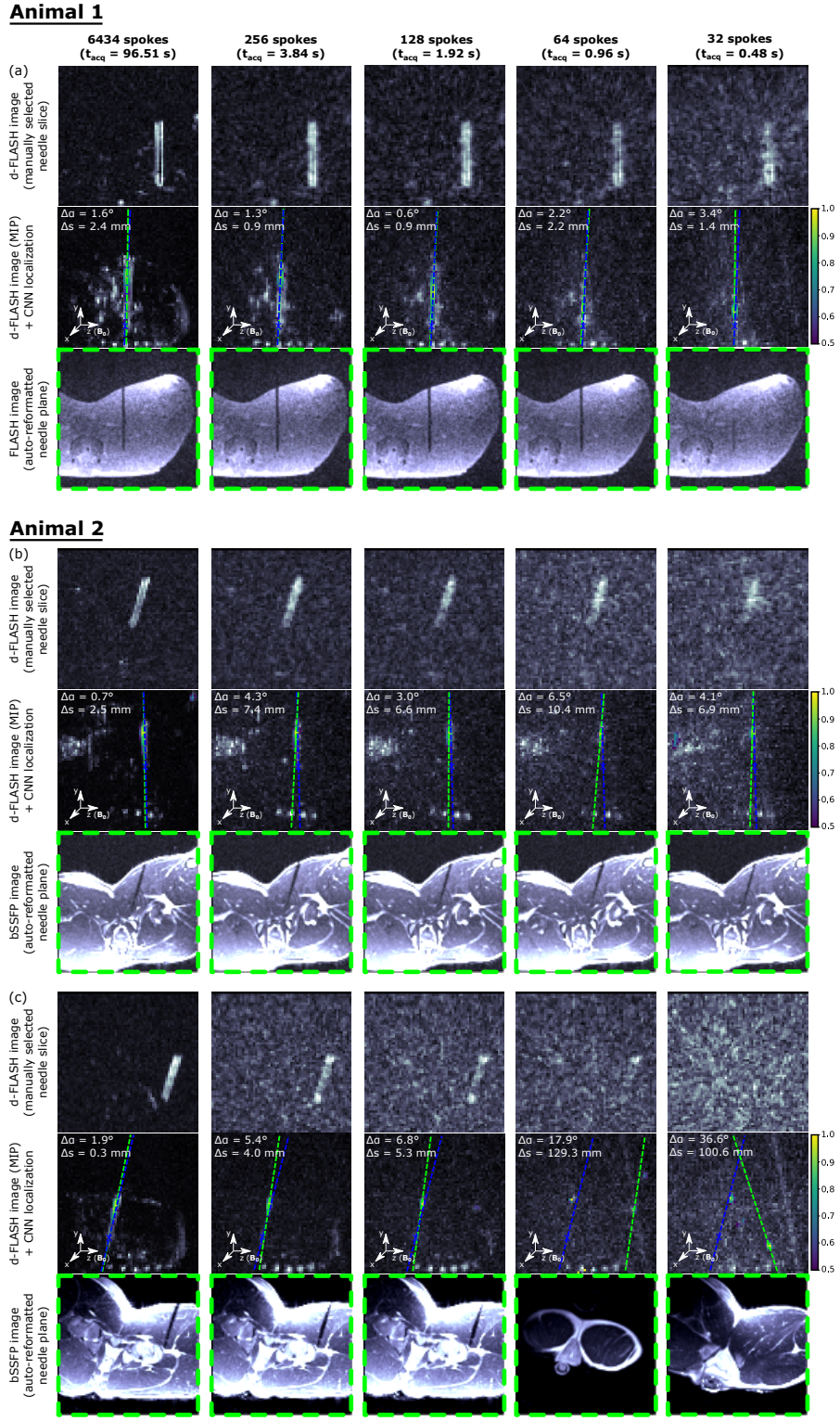

Figure 4.10: Investigation of the proposed CNN-based rapid 3D needle localization technique in proof-of-principle in-vivo experiments with needles inserted at $\theta_1 = 87.7°$ (a), $\theta_2 = 88.8°$ (b), and $\theta_3 = 77.6°$ (c). Coloring of needle axes as in Fig. 4.9. Figure adapted from Faust et al. [4].

visibility of the artifact is restricted at the tip for localizations from all investigated n_{spokes} except for $n_{\text{spokes}} = 6434$. For the localizations from fewer k-space spokes, Δs is noticeably larger then the chosen slice thickness of $4\,\text{mm}$. For the case depicted in Fig. 4.10c, the needle artifact is fully visible in the aligned planes for localizations from 6434 ($\Delta\alpha = 1.9°$; $\Delta s = 0.3\,\text{mm}$) down to 128 spokes ($\Delta\alpha = 6.8°$; $\Delta s = 5.3\,\text{mm}$). For localizations from fewer sampled spokes (64 & 32 spokes), needle localization did not succeed, resulting in failing ASP for these cases (needle not visible in reformatted slice).

5 Discussion

Automatic slice alignment of 2D real-time imaging planes with the needle during MR-guided needle interventions can support the interventionalist by simplifying and accelerating the workflow of the procedure. 3D needle localization is required to allow for automatic slice alignment with the needle. Passive localization techniques only use the effect of the metallic needle itself on the MR image. In this dissertation, the needle artifact was first characterized for conventional FLASH imaging, as well as for dephased GRE. Two methods for rapid passive 3D needle localization were then investigated with the purpose of enabling automatic slice alignment during MR-guided in-bore interventions. While the first method made use of a baseline-subtracted FLASH acquisition, the second method employed positive contrast imaging with dephased FLASH to localize the needle from a limited acquisition of radial k-space lines.

5.1 Delineation of needles in MRI

Needle artifacts were characterized and evaluated for conventional FLASH imaging, as well as for susceptibility-based positive contrast imaging using dephased GRE. For FLASH, measured needle artifacts were compared to a simple dephasing model. To evaluate dephased GRE contrast, three different research MR pulse sequences were implemented to enable d-FLASH, d-SSFP and d-bSSFP imaging. Signal models for d-SSFP and d-bSSFP contrast were proposed and compared with the well-known d-FLASH signal model [20]. The artifact of a cylindrical biopsy needle was theoretically investigated with the introduced signal models and evaluated in phantom experiments.

5.1.1 Needle artifacts in FLASH imaging

A simple analytical model was investigated to predict the shape and size of the dephasing artifact introduced by a needle in FLASH imaging. Dice similarity coefficient (DSC) and Hausdorff distance (d_H) were used to assess the quality of the model. Comparing the measured artifact with the model at different field strengths, echo times and image resolutions, good correspondence between the modeled and measured needle artifact was observed ($DSC \geq 86\,\%$ and $d_H \leq 2\,\mathrm{px}$ for all investigated cases).

The artifact was hereby defined to include pixels with a signal intensity reduced by $50\,\%$ compared to the background signal intensity. Other authors have measured the size of needle artifacts in MR images by determining the width of the artifact through visual inspection [12, 13]. The chosen

threshold of $S_{\text{artifact}} < 50\,\%S_{\text{BG}}$ in this work, which was evaluated within a manually positioned artifact ROI, was found to fit well to the visual impression of the artifact (see Fig. 4.1).

The measurements performed in this study were subject to several limitations. The dephased disk/cylinder model as investigated in this thesis was derived from the description of a biopsy needle as a metallic cylinder of infinite length by Ladd et al. [9]. This condition is violated at the tip of the needle. Müller-Bierl et al. [16] proposed a numerical investigation of the field inhomogeneity at the needle tip to investigate the emerging artifact, describing the tip artifact as "ball-shaped" (depending on the tip geometry and the needle orientation to the main magnetic field). The investigated dephased disk/cylinder model is therefore only intended to describe the artifact at a certain distance from the needle tip, which is also expected to depend on needle orientation, imaging parameters, and tip geometry. Furthermore, the artifact model was investigated for conditions that might not necessarily be matched in an MR-guided intervention, and that should be addressed in future work. The images used in the study were acquired with an isotropic image resolution. The model, as introduced in Section 2.3.2, neglects the orientation of the local susceptibility-introduced magnetic field gradient and assumes the gradient to always act along the voxel edge. In addition, the gradient is assumed to be approximately linear across one voxel. Switching to an anisotropic voxel grid or larger voxels, the increasing violation of these modeling conditions could increase the deviation of the observed artifact from the investigated dephased cylinder/disk model. Therefore, if an anisotropic resolution is chosen for imaging, a more complex analytical or numerical treatment might become necessary to satisfactorily model the needle artifact. Furthermore, to suppress any potential positional signal mismatch due to local changes of the PRF in proximity of the needle, a frequency encoding direction along the needle shaft was chosen for the conducted measurements, as no magnetic field distortion is expected in this direction (see Section 2.3). If the frequency-encoding direction is not aligned with the needle shaft, signal shifts due to spatial frequency mismatch, that can distort the observed artifact, must additionally be considered. For high receiver bandwidths, the dephasing artifact is, however, expected to dominate over local image distortions (see Section 2.3.2).

5.1.2 Needle artifacts in dephased GRE imaging

After the investigation of needle-induced dephasing artifacts for conventional GRE contrast, more specifically spoiled FLASH contrast (see discussion in previous section Section 5.1.1), needle-induced positive signal artifacts were investigated for dephased GRE contrast, more specifically d-FLASH, d-SSFP and d-bSSFP contrast. Signal models were introduced for d-SSFP and d-bSSFP and, together with a well-established model for d-FLASH [20], the predictions of the models on the shape, size, and magnitude of the artifacts were evaluated in phantom measurements.

The d-bSSFP signal model predicted a point-symmetric positive signal artifact for a needle modeled as an infinite cylinder, while for d-FLASH and d-SSFP, an axisymmetric artifact was expected. Consistent with the theoretical prediction, phantom measurements verified the predicted artifact symmetries, which can be attributed to the combination of discrete and continuous phase evolutions induced by different types of WM and susceptibility-induced gradients (spoiled or

balanced vs. unspoiled/unbalanced), as illustrated in Fig. 2.4. While the d-bSSFP signal model was studied for the example of a cylindrical needle in the context of this dissertation, a point-symmetric artifact would also be anticipated for spherical objects such as fiducial markers, as these, similar to the cylindrical geometry, also evoke a symmetric field distortion [10].

Using the described models for the three investigated types of dephased GRE contrast, theoretical signal magnitude ratios were derived for d-SSFP and d-bSSFP, comparing the maximum artifact signal as well as the cumulated artifact signal. The different steady-state magnetizations (coherent steady-state for d-SSFP and d-bSSFP, or incoherent steady-state for d-FLASH) make the signal magnitude ratios tissue-dependent when comparing d-FLASH with d-SSFP and d-bSSFP, rendering a general prediction of the respective signal magnitude ratio not feasible (see Section 2.3.2). In general, a higher signal magnitude can be reached with coherent steady-state imaging techniques than with incoherent steady-state imaging [64, 73]. The experimental analysis of the three contrast methods matched the anticipation of higher maximum signal magnitudes for d-SSFP and d-bSSFP imaging compared to d-FLASH (see Table 4.2). Comparing the d-bSSFP with the d-SSFP signal magnitude, a slightly lower maximum signal ratio (within one standard deviation) and cumulative signal ratio (within two standard deviations) were found as would have been expected from the theoretical prediction. Discrepancy between the models' predictions and measured signal magnitude ratios may be a consequence of the simplifications made by the signal models. An assumption made by the models was that the gradients acting on the local magnetization were spatially constant within a voxel. Due to the susceptibility-induced spatially varying field distortion, this is only an approximation (first-order Taylor approximation of the magnetic field inhomogeneity). In addition, the models assumed the coherent steady-state signal magnitude to be constant across individual voxels (following Lebel et al. [69]). As described in Section 2.2.2, the coherent steady-state signal magnitude depends on the locally-induced phase advance during T_{R}. Another simplification that the model makes is that it also presupposes a constant VSF. However, as described in Section 2.1.4, the sampled imaged magnitude does not uniformly represent the distribution of transverse magnetization within the voxel, but is modified by the VSF given in Eq. 2.46 [46]. All these simplifications could result in measurements diverging from the models' prediction, as the observed signal might not accurately reflect the phase coherence established by the gradients acting throughout the voxels. Nevertheless, the highest cumulative artifact signal was found for d-bSSFP experimentally, as expected.

To further assess the accuracy of the introduced signal model, the radius of the d-bSSFP needle artifact was examined for six distinct T_{E}. The model for the artifact radius was fitted to the measured radius for the evaluated T_{E}, choosing χ_i as a free parameter and finding its value to lie within two standard deviations of the literature value. Deviations of the measured value from the expected value might not only be attributed to the shortcomings of the model as described above. The needle material's susceptibility is known from literature, however its true value might be different depending, e.g., on the manufacturing process of the material [76]. Also, the assumed magnetic field strength of the scanner might locally differ due to distortions induced by the phantom susceptibility and geometry. However, as can be seen in Fig. 4.3b, for each T_{E} analyzed, the predicted artifact radius was found to be within the margins of error of the respective measurement, supporting the relationship found for the artifact radius in Eq. 2.74 and indicating good applicability of the model.

Some of the d-bSSFP images depicted in Fig. 4.3a were found to contain stripe-like artifacts within the water phantom. These artifacts, seemingly unrelated to the needle artifact due to their spatial separation in the image, may originate from eddy currents caused by the radial readout trajectory used for image acquisition. Scheffler et al. described how rapid changes in the orientation of the k-space trajectory can lead to changing eddy currents across multiple T_R which then again evoke residual unbalanced net gradient moments in bSSFP imaging [94]. A similar effect might occur in d-bSSFP imaging, evoking phase flips in certain voxels. Partial phase coherence could then be reestablished by the WM gradient in these voxels, leading to the observed hyperintensities. It is anticipated that adopting a Cartesian readout trajectory would mitigate the occurrence of these artifacts.

As was shown in Fig. 4.2, the d-FLASH and d-bSSFP positive contrast artifacts appear homogeneous along the needle shaft while the d-SSFP artifact is disturbed by dark banding artifact as are known from bSSFP imaging. In conventional bSSFP imaging, all external gradient moments are balanced at the end of T_R (see Section 2.2.2). An underlying unbalanced gradient moment (e.g. due to a field inhomogeneity) can however evoke a phase flip in certain voxels (as modeled by Eq. 2.62). This can lead to a decrease in signal, as partial magnetization with opposite phase interferes destructively. d-SSFP contrast is sensitive to banding due to the same mechanism. As outlined in Section 2.3.2, the susceptibility-induced gradient is locally balanced in d-SSFP by a compensating external WM gradient. Where gradients are fully compensated, no net gradient exists and the signal mimics conventional bSSFP contrast [21, 95]. Therefore, for full gradient compensation, the local signal consequently becomes inherently prone to banding artifacts typical for bSSFP. In contrast, d-bSSFP imaging avoids banding issues. Here, at points of maximum signal compensation, the susceptibility-induced gradient deliberately introduces a phase flip with partial constructive interference reestablished by the overlying linear phase due to the WM gradient. Minor background gradients, e.g. from imperfect shimming, will only cause insubstantial changes to the deliberately unbalanced gradient.

To investigate and compare the different types of dephased GRE, the proposed signal models for d-SSFP and d-bSSFP were evaluated together with the well-established sinc model for d-FLASH [20]. As described in Section 2.2.3, these models allow for the prediction of the average signal magnitude for a susceptibility-induced gradient moment, acting together with the external WM gradient on the local magnetization, with the acting gradient moments being either spoiled or balanced or unspoiled/unbalanced at the end of T_R. For the application of unspoiled/unbalanced gradient moments, the local phase introduced takes discrete values (Eq. 2.62). This makes the voxel-integrated d-SSFP and d-bSSFP signals dependent on a local discrete phase offset, which does not affect the integrated signal magnitude for a continuous phase evolution as in d-FLASH. By averaging over a varying phase offset, the mean voxel signal magnitudes $\bar{S}_{\text{d-SSFP}}$ and $\bar{S}_{\text{d-bSSFP}}$ were calculated in Eq. 2.63. For a small, spatially uniform, unspoiled/unbalanced gradient moment (induced dephasing $< \frac{2\pi}{\mathrm{pixel}}$) acting on magnetization, a modulation in signal magnitude across voxels, based on the local phase offset, could potentially result in bright bands in d-bSSFP that are spaced closer together for higher gradient compensation, similar to conventional bSSFP imaging where a constant weak background gradient moment can introduce phase flips in regular spatial intervals (depending on the local phase offset), which manifest as dark banding artifacts in the image. Nevertheless, such discrete effects were not observed in the conducted experiments.

For the investigated needle-induced field distortion, the magnitude of the susceptibility-induced gradient rapidly decreases (with $\frac{1}{r^3}$ as can be derived from Eq. 2.68) as the distance from the device increases, likely preventing band formation.

The three research pulse sequences, implemented in this work to acquire images with d-FLASH, d-SSFP, and d-bSSFP contrast, sample the k-space following a radial acquisition method. In radial sampling, an altered PRF near a magnetic disturber will result in a signal blurring rather than in discrete spatial signal shifts (see Section 3.1.2). However, if a Cartesian approach were considered to acquire images with dephased GRE contrast, increasing the receiver bandwidth would similarly be expected to mitigate any potential artifact distortions (cf. Section 2.3.2). In the implemented pulse sequences, the WM gradient moment was played out along the B_0 axis. Alternatively, the gradient moment could be oriented in a different direction, with the artifact signal maxima positions being derivable from a modified Eq. 2.73 in a way similar to the calculations performed. While changing the gradient direction might alter the artifact's orientation, its basic appearance and symmetry would likely remain unchanged, due to the independence of the signal models Eq. 2.63 from the WM orientation.

In the first part of this dissertation, conventional (FLASH) and dephased GRE (d-FLASH, d-SSFP, d-bSSFP) contrast techniques were investigated as negative and positive contrast imaging methods for needles. Both contrast regimes allow for a delineation of the needle in the MR image, producing either distinct hypo- or hyperintense artifacts which were investigated by evaluating respective signal models in phantoms. For FLASH imaging, the dephasing artifact in the image was well described by a simple dephased disk model (corresponding to a dephased cylinder along the needle shaft in 3D). MR-guided needle interventions can benefit from prior knowledge of needle artifact size and shape, as the artifact is important for instrument visualization and localization [12]. The investigated model allows a prediction of needle dephasing artifacts for a given set of imaging parameters. The analysis, therefore, provides an understanding of the artifact formation and could, e.g., be used to guide needle intervention planning (e.g., choice of needle type and imaging parameters at a given field strength). In the context of this dissertation, it was used to motivate the proposed 3D sinc approach to model a needle artifact in a baseline-subtracted k-space as described in Section 3.2.1, which corresponds to a cuboid in image space, approximating the cylinder-shaped artifact. In addition to needle artifacts for conventional FLASH imaging, the positive signal artifacts for three types of positive susceptibility-based contrast imaging with dephased GRE were investigated and compared. Signal models were developed for d-SSFP and d-bSSFP to predict, together with the well-known signal model for d-FLASH [20], the positive signal artifact produced by a cylindrical aspiration needle. The evaluation showed that, in contrast to d-FLASH and d-SSFP, the d-bSSFP needle artifacts exhibited greater symmetry and increased overall artifact signal. Furthermore, the d-bSSFP positive signal artifact is, in contrast to the d-SSFP positive signal artifact, inherently unaffected by banding. These characteristics render d-bSSFP, compared to d-FLASH and d-SSFP, a potentially advantageous technique for applications in interventional MRI such as needle localization, as investigated in the further course of this dissertation. For instance, the greater symmetry found for the d-bSSFP positive signal

device artifact improves visibility due to increased number of established signal maxima (six rather than three maxima for the needle as depicted in Fig. 2.7), simplifying the task of identifying the artifact's center. Furthermore, the additional maxima in the d-bSSFP artifact add redundancy which might prove particularly useful when analyzing the artifact in heterogeneous tissues instead of a homogeneous water phantom, as signal intensity can vary for different tissue due to a varying steady-state signal magnitude influenced by the tissues' characteristics (see Section 2.2.2). Some sensitivity to hyperintense artifacts in the image, likely unrelated to the device, was found for d-bSSFP. The found artifacts for d-bSSFP imaging could potentially be eddy-current related and associated with the employed radial acquisition strategy [94]. However, further investigations are required to confirm this hypothesis. As for the investigated localization technique in this dissertation, a good suppression of background signal by the employed imaging technique is crucial (see Section 2.3.3), d-FLASH was used for the conducted localization experiments, despite its lower signal intensity and reduced symmetry.

5.2 3D rapid passive needle localization for automatic slice positioning

Two passive needle localization methods were investigated for the purpose of ASP in MR-guided needle interventions, which make use of the artifact introduced by the needle. While the first investigated method made use of a baseline-subtracted, limited radial k-space acquisition with FLASH contrast, the second method employed an undersampled d-FLASH acquisition without the need for a baseline scan.

Both investigated methods for needle localization were evaluated with the same metrics (Δs and $\Delta\alpha$). An additional metric Δc was used to evaluate the artifact center deviation for the model-based method to characterize the split optimization over phase (encoding the positional parameters of the needle) and magnitude (encoding the angular parameters of the needle) of the k-space model, which does not necessarily provide useful additional information for the CNN-based approach, for which the evaluation of this additional metric was therefore omitted. The visibility of the needle tip in an automatically positioned imaging slice is especially crucial to the interventionalist as it can allow for accurate targeting. The visibility of the needle (tip) artifact in an imaging plane depends on the quality of the slice alignment, slice thickness and on the width of the needle artifact, which in turn depends on various factors including size and material of the needle, magnetic field strength and chosen imaging sequence parameters (see Section 2.3 or cf., e.g., [12]). In MR-guided interventions, the use of relatively thick slices (thickness $0.5\,\mathrm{cm}$ to $1\,\mathrm{cm}$ [8]) can be common to increase artifact and target structure visibility. By definition, Δs can be considered a conservative metric to evaluate feasible automatic slice positioning as it describes the "worst-case" distance of the ground truth needle tip position to a slice aligned with the detected needle trajectory, motivating the threshold of $\Delta s \leq 1.0\,\mathrm{cm}$ that was set to assess localizations in Table 4.3 and the evaluated thresholds in Table 4.5. Mehrtash et al. recommended employing a similar metric to Δs by measuring the distance between the needle tip and a defined axial plane. The introduced Δs offers greater versatility by not restricting the chosen plane to

an axial direction, but rather, it defines the maximum distance from the needle tip to a selected plane, independent of the plane's orientation angle, making it therefore a slightly more general metric. With the proposed metrics, the achieved accuracy for the performed ex-vivo studies was characterized by calculating the median ($\pm$ median absolute deviation) as a measure of central tendency, as also used by various other authors to characterize achieved accuracy for investigated needle localization methods [32–34]. The median was chosen as a characterizing property of the investigated datasets as it is robust with respect to outliers (compared to the mean), which were expected for failed localization attempts. If the localization of the needle failed completely, either due to an unsuccessful optimization for the forward model-based localization approach or an unsuccessful detection of the needle path by the employed CNN, the output needle parameters produced by the algorithm are not expected to be correlated to the true localization and can therefore be considered outliers which cannot be used to estimate the reachable accuracy for successful localization attempts.

5.2.1 Forward model-based 3D needle localization using a baseline-subtracted FLASH acquisition

The first method investigated in this dissertation for passive 3D rapid needle localization was based on a baseline-subtracted limited radial FLASH k-space acquisition after a needle insertion. The subtraction k-space data was then modeled using a 3D sinc function, and a fitting procedure was used to determine the needle's positional and orientational parameters. The detected needle location and orientation could then be employed for ASP.

As demonstrated in Section 4.1.1, the needle artifact for FLASH imaging can be well described with a dephased disk/dephased cylinder model (Section 2.3.2). The needle artifact in an image reconstructed from a baseline-subtracted k-space acquisition after a needle insertion consequently resembles a hyperintense cylinder (the isolated dephasing artifact) on a suppressed image background. To model the needle artifact in the baseline-subtracted FLASH k-space data, a 3D sinc model was employed. Transferred to image space, this model corresponds to a hyperintense cuboid. While a more sophisticated model might be able to approximate a cylinder-shaped artifact in image space, and, therefore, the true artifact k-space signature, more closely, the chosen 3D sinc function was shown to be a simple and robust modeling approach in the conducted ex-vivo study and accurate localization of a needle artifact in 3D from as few as 5 k-space spokes was shown to be feasible (see Section 4.2).

The success of the localization with the investigated method was evaluated for different choices of initial optimization parameters used for the model fit, as well as numbers of acquired k-space spokes employed for the localization. If the proposed needle localization method were to be used for an automatic slice alignment, the initial optimization parameters could be interpreted to correspond to a more or less severe initial slice misalignment to be corrected by the use of ASP. For initial optimization parameters corresponding to a more severe initial slice misalignment, a lower median localization accuracy was found for the samples from the ex-vivo study (represented by all three employed localization metrics, see Table 4.3). An investigation of the model's angular cost function for a selected ex-vivo sample (Fig. 4.6) suggested the conclusion that the optimization,

especially from very few k-space spokes, is non-convex and the employed downhill-simplex optimizer can, therefore, become stuck in local minima. For the example in Fig. 4.6, it can be seen that the global minimum of the angular cost function and the true angular parameters of the needle insertion coincide, indicating that an extraction of the true needle parameters from as few as 5 k-space spokes might still be feasible with a brute-force global minimum search across the cost function. This conclusion also supports the theoretical motivation presented in Section 2.3.3, describing the extraction of a needle's positional and orientational parameters from a limited k-space acquisition. Such a global approach to find the optimization minimum would, however, be computationally expensive and increase localization time. Severe initial slice misalignments that could make such a global minimum search necessary are also not to be expected in many use cases. Typically, a needle trajectory is selected in a 3D planning image by the interventionalist before the needle insertion and the initial 2D real-time imaging planes are aligned with that trajectory [8]. The interventionalist can then chose the insertion point and angle using visual feedback from the real-time image and the chosen real-time imaging plane is not expected to deviate much from the needle trajectory. Increasing the number of sampled k-space spokes used for localization stabilized the optimization in the conducted ex-vivo study (see Fig. 4.6 and Table 4.3).

In the conducted initial ex-vivo study, a needle insertion depth of $l = 5\,\mathrm{cm}$ was chosen for all needle insertions. Other, especially shorter, insertion depths could affect the performance of the localization algorithm and might require an additional fine-tuning of the chosen initial cuboid length l_c for the optimization algorithm. As described above, initial plane alignment is usually established using direct visual feedback from the real-time images, and many misalignments are expected to only affect artifact visibility after a certain insertion depth is reached (needle "moving out" of 2D imaging plane). For the ex-vivo study, needle inclination angles were sampled by manually inserting the needle randomly into the phantom with angles up to $36°$ from the orthogonal to the $\vec{B}_0$ field. The susceptibility-induced field distortion by the needle that causes its FLASH artifact diminishes with a smaller inclination angle to $\vec{B}_0$, leading to a vanishing shaft artifact for a needle orientation parallel to the magnetic field (see Eq. 2.71 or cf. [9, 12]). In this case, the proposed localization method would likely fail as no dephasing artifact could be modeled (a slight artifact can remain due to tissue displacement, see Section 2.3). Further investigations should evaluate a potential dependency of the needle localization accuracy on the needle inclination and limits of the proposed technique concerning steep inclination angles more parallel to $\vec{B}_0$. As the artifact changes in size with a changing inclination angle, an optimization of the cuboid model width (treated as fixed empirical value in this work) could potentially improve the algorithm's performance for trajectories sampled from a wide range of inclination angles. This would however increase the optimization's complexity by one dimension. Transversal or near transversal trajectories, as investigated in the conducted ex-vivo study, are, however, a common choice in MR guided interventions [96].

For an example from the ex-vivo study dataset, as well as for an in-vivo proof-of-principle case, successful retrospective slice realignment was demonstrated using the proposed localization algorithm. The in-vivo data evaluated in this work was acquired under free breathing. Images reconstructed from the acquired subtraction k-space for the displayed proof-of-principle in-vivo experiment in Fig. 4.7 show hyperintense areas which appear unrelated to the needle artifact itself.

This incomplete suppression of background could be related to motion. The proposed needle localization method requires the acquisition of a baseline dataset. The acquisition of the two datasets at different points in time makes the calculated subtraction k-space inherently sensitive to motion-induced tissue displacement or deformation. Due to a potential misregistration of the two acquired k-spaces, areas that are subjected to such motion might present with residual signal. As residual background signal due to a motion-induced misregistration of the k-space acquisitions before and after the needle insertion is not included in the 3D sinc model, it could corrupt the optimization, leading to a decrease in localization accuracy or failure of localization. For the in-vivo localization using initial parameter set 1, $\Delta\alpha$ was largest with 64 acquired k-space spokes (see Table 4.3). Here, motion (e.g., breathing-induced tissue displacement in the exterior of the FOV) could potentially have led to an increasing inconsistency in sequentially acquired k-space spokes as the acquisition time is longer for a higher number of sampled k-space lines, causing the decrease in localization performance. For the in-vivo demonstration, the needle was inserted into the thigh of the animal. More challenges concerning subject motion might also arise when translating the method to interventions in tissue that is directly affected by breathing, e.g., liver. Robustly localizing the needle in in-vivo scenarios with expected tissue motion might therefore require the application of motion correction strategies, such as the acquisition of multiple baseline datasets at different breathing stages or the application of motion triggering to time the acquisition. For ventilated patients, the proposed rapid needle localization could also be performed during a breath hold. Future work must investigate the robustness of the proposed technique for application under in-vivo conditions in a dedicated study.

5.2.2 3D needle localization using dephased FLASH contrast and CNN-based postprocessing

A second approach to rapid 3D passive needle localization in MR-guided interventions was introduced and assessed, leveraging a CNN-based algorithm and susceptibility-based positive contrast imaging with d-FLASH. Due to the inherent background suppression with dephased GRE techniques, no baseline scan was required for the generation of a background-suppressed image with a hyperintense needle artifact.

Needle localization with the proposed approach was evaluated in an ex-vivo study and demonstrated in proof-of-concept in-vivo experiments. The potential for automated slice repositioning was confirmed in retrospective analyses. Only sampling a reduced number of radial k-space spokes (undersampled image acquisition), analogous to the limited radial k-space sampling for the investigated forward model-based approach discussed in the previous section and, again, following the theoretical motivation given in Section 2.3.3, enabled an accelerated needle localization for needles placed with insertion angles close to the perpendicular to the $\vec{B}_0$ field.

In the performed ex-vivo study, the median localization accuracy was reduced as the number of sampled k-space spokes used for the localization decreased and for needle paths aligned more closely with $\vec{B}_0$ and $\vec{G}_{\mathrm{WM}}$. Similarly, in the in-vivo proof-of-principle experiments, localization performed better for the cases where the needle was more closely aligned with the perpendicular to the $\vec{B}_0$ and $\vec{G}_{\mathrm{WM}}$ direction than when the needle was tilted further towards $\vec{B}_0$. While, for

the examples from the ex-vivo dataset depicted in Fig. 4.9, the WM needle artifact could be clearly delineated in the d-FLASH images reconstructed using full k-space sampling, increased background noise obscured the artifact visibility in images reconstructed using less sampled k-space spokes, particularly for the case Fig. 4.9b, where the needle inclination deviated further from the orthogonal to $\vec{B}_0$ and $\vec{G}_{\text{WM}}$ then for the case Fig. 4.9a. As described in Section 2.3.2, a WM gradient moment, e.g., applied along the $\vec{B}_0$ direction, as it was implemented in this work, can no longer be entirely counteracted by the local susceptibility-induced gradient $\vec{G}_{\text{susc}}$ for needle orientations tilted against this orientation, as $\vec{G}_{\text{susc}}$ always remains orthogonal to the needle and the non-counteracted part of the gradient leads to global dephasing and, consequently, a diminished artifact signal. This reduction in artifact visibility appeared to impair the CNN's ability to accurately regress to the needle path, resulting in lower accuracy reached for needle localization from fewer sampled k-space spokes and needle orientations more aligned with $\vec{B}_0$ and $\vec{G}_{\text{WM}}$. In the performed ex-vivo study, localization of needles inserted with inclination angles in the range of $\theta = [78°, 90°]$ was examined. A further reduction in localization accuracy is anticipated for insertion angles beyond this range. Consequently, the proposed method for rapid localization is primarily applicable to needle paths with an inclination near the transversal plane. As an alternative to dephased GRE techniques, other susceptibility-based, positive contrast techniques that allow the generation of hyperintense artifacts for metallic devices have been investigated in the past [18, 22, 23, 97]. These alternative positive contrast techniques might reduce the angular dependence of the contrast, as they are not explicitly direction-dependent compared to dephased GRE. Dharmakumar et al. proposed a susceptibility-based positive contrast technique which makes use of the flip angle-dependent signal magnitude relation of bSSFP contrast with the locally induced dephasing [97]. Stuber et al. propose the suppression of the on-resonant tissue signal, i.e., the background signal further away from a metallic disturber, while only acquiring signal from the proximity of the metallic device where the PRF is altered [22]. Employing an alternative positive contrast method to dephased GRE could, however, come with other limitations, such as reduced background suppression [18]. Future research might explore a similar CNN-based needle localization technique as applied in this work, which, instead of using undersampled d-FLASH images, employs another positive susceptibility-based contrast method with the potential of decreasing angular dependency of the localization accuracy results. However, any employed susceptibility-based technique will still be inherently angular-dependent to a certain degree as the field disturbance introduced by a cylindrical needle (as modeled by Eq. 2.69) reduces with increasing parallel orientation of the needle with respect to $\vec{B}_0$. Recently, CNN-based needle localization using undersampled d-FLASH images (WM gradient applied along three orthogonal axes) was investigated for interventional needles that were specifically designed to include susceptibility markers placed along the shaft [98]. The WM artifact, evoked by the susceptibility markers, was also visible for a needle orientation parallel to the B_0 direction and a localization of the needle was feasible. The results indicate that, using sophisticated needle designs, the angular constraint for the investigated localization method can be mitigated. As already noted in Section 5.2.1, transversal paths or needle paths with an inclination close to $\theta = 90°$ are, however, common in MR-guided interventions [96].

After the acquisition of the d-FLASH data, the proposed localization algorithm includes an image reconstruction step and a CNN-based postprocessing step, as was outlined in Section 3.3. While

the processing time for the reconstructed d-FLASH images remained constant, the reconstruction time itself depended on the number of acquired k-space samples. Utilizing specialized hardware like GPUs could allow to reduce image reconstruction times [99] and therefore further accelerate the localization.

For needle localization from a fully- and undersampled k-space with different numbers of sampled k-space lines, distinct CNN models were trained using the network architecture and the same set of optimization hyperparameters were employed for network training with no dedicated hyperparameter optimization performed on the used training/validation set except for choosing an appropriate number of training epochs (200) to reduce overfitting (see Appendix A.4 for the model loss). While accuracy results for the localization metrics are in the order of the image resolution of the reference images (and therefore also in the order of the annotation accuracy) for the localization from fully sampled images ($\widetilde{\Delta s} \approx 2\,\mathrm{mm}$ for $\theta \in [86°, 90°]$) and a further increase in localization accuracy would not be expected, a further increase of localization precision might be achievable by conducting a systematic optimization of hyperparameters or changes in the network's architecture for needle localization from undersampled images. The physical restriction of a reduced artifact signal magnitude for high undersampling factors and needle inclination angles increasingly parallel to $\vec{G}_{\mathrm{WM}}$ and $\vec{B}_0$, however, remains. The CNN utilized for the implemented localization algorithm was trained using images of needle insertions into ex-vivo porcine tissue phantoms which were acquired with the phantoms placed in a head coil. The set-up facilitated the data acquisition for the training set, as it was easy to move, exchange, and rotate the phantoms during the extensive generation of training data. Successful localizations with the ex-vivo test dataset showed that the network effectively generalized to the adapted, dedicated interventional coil configuration used for the acquisition of the ex-vivo test dataset (loop coil + spine coil), as well as the coil configuration used for the in-vivo animal proof-of-principle experiments (using both loop + spine coil and flex + spine coil). For the needle localizations in the first animal, a slightly larger needle type was used than for the training. The in-vivo animal models were also larger and characterized by more complex anatomical features as represented by the ex-vivo phantoms (as well as subject to physiological processes as breathing motion, blood flow etc.), resulting in various background artifacts. Other differences to the training data comprise a different needle insertion depth and slightly altered imaging parameters (changed bandwidth and T_{R}). Localization was still successfully demonstrated for the proof-of-principle in-vivo cases (2D slice fully or partially aligned with the needle), indicating a certain robustness of the CNN-based WM needle detection mechanism. Future investigations must assess the proposed method's reliability, especially when applying it to in-vivo scenarios that might pose additional challenges to the localization, such as abdominal interventions where patient motion, e.g. due to breathing, could have a larger influence. With the the implemented golden means sampling scheme, the method would however allow the number of k-space spokes acquired, and thus the acquisition duration, to be adjusted based on the anticipated extent of patient motion.

5.2.3 Comparative analysis of the investigated needle localization methods

In the dissertation, two methods for passive 3D rapid needle localization for MR guided interventions were investigated. Both methods made use of MR artifacts induced by a metallic needle. The first introduced method for needle localization employed an optimization over a 3D sinc function to model the needle signature in a baseline-subtracted k-space acquisition with a FLASH pulse sequence. The subtraction k-space (calculated by the subtraction of a baseline acquisition before needle insertion from an acquisition after needle insertion) only contained the k-space signature of the needle, assuming no misregistration between the two acquisitions, e.g., due to patient motion, which could corrupt the subtraction of the background signal. To address and remove the constraint of a motionless or motion-corrected baseline subtraction, the second investigated localization method employed d-FLASH contrast to generate a background-suppressed image with a hyperintense needle artifact. The needle was localized from the (undersampled) d-FLASH images using a CNN-based postprocessing algorithm.

With reported frame rates used in MR-guided needle interventions of 2 to 5 frames per second [8], a localization with an acquisition time below $1\,\mathrm{s}$ would likely not be considered a major disruption to the workflow. For the investigated forward model-based needle localization approach, a median localization accuracy of $\widetilde{\Delta s} = 0.5\,\mathrm{cm}$ and $\widetilde{\Delta\alpha} = 7^\circ$ were achieved in the ex-vivo study for localization from 64 acquired k-space spokes ($t_{\mathrm{acq}} = 0.8\,\mathrm{s}$) with insertion angles sampled up to 36° out of the orthogonal to $\vec{B}_0$ (most general set 3 of initial parameters, see Table 4.3). For the CNN-based approach, a median accuracy of $\widetilde{\Delta s} = 0.4\,\mathrm{cm}$ and $\Delta\alpha = 7^\circ$ was found, equally for a localization from 64 sampled k-space spokes and for insertion angles sampled between 8° and 12° out of the orthogonal to $\vec{B}_0$, with a higher median localization achieved for angles closer to the transversal plane. For the two investigated needle localization approaches, achieved needle localization accuracy, in terms of the defined metrics, was therefore found to be of the same order of magnitude for localizations for a data acquisition time just below one second, with the forward model-based method, however, being evaluated for a larger range of insertion angles. For both investigated needle localization methods, ASP employing the performed localization was successfully demonstrated (full and partial retrospective alignments of 2D imaging slice) for slice thicknesses common in interventions [8] ($4\,\mathrm{mm}$ and $8\,\mathrm{mm}$ for the demonstrations in Fig. 4.9 as well as Fig. 4.10, and Fig. 4.5 as well as Fig. 4.7, respectively).

For the implemented forward model-based localization approach, success of the localization was dependent on the initial set of optimization parameters (e.g., corresponding to an initial misalignment of a chosen imaging plane), while the CNN-based approach has the advantage that it does not rely on prior information of the needle position and orientation. However, using a higher number of acquired k-space spokes for the forward model-based algorithm allowed for accurate needle localization in the ex-vivo study, also for a very general set of initial optimization parameters that can be interpreted as essentially no prior information on the needle position and orientation (a shift of FOV for each artifact center coordinate implicates that the position of the needle is unknown a priori, similar to a shift of 60° in angular parameters being larger than the investigated angular range in the study).

Due to the directional orientation of the WM gradient moment, the WM artifact signal magnitude was diminished for insertion angles tilted out of the orthogonal to $\vec{G}_{\mathrm{WM}}$ and $\vec{B}_0$, which impacted needle path localization. The needle artifact for the employed FLASH imaging is also orientation dependent (Eq. 2.71) and further research must investigate potential angular limits for the localization (for completeness, localization results from the conducted ex-vivo study, broken down individually for the angular orientation of the needle insertion can be found in Fig. A.1).

The CNN-based algorithm employed for the second investigated localization technique was designed to robustly extract the needle parameters from an undersampled d-FLASH image, which can be affected by background artifacts unrelated to the needle, with the use of ML. While the method does not require a baseline acquisition and is therefore inherently insensitive to inter-acquisition patient motion, the employed CNN needed to be trained for the localization of the needle, requiring the acquisition and annotation of a training dataset. The forward model-based needle localization method investigated has the advantage that it can be used without the need for training data and might therefore pose an alternative needle localization method if no trained network is available for a certain needle device or imaging scenario. While they are able to generalize and perform well on previously unseen data, deep learning (DL) models are often described as a "black box" [100], making it challenging to predict their performance for data which might differ from the samples in the training dataset (different scanned anatomies, coil positioning, noise levels, sequence parameters, needle types etc.). While the reported in-vivo experiments served as a proof-of-principle that localization is generally feasible with the CNN trained in an ex-vivo scenario with a different needle and slightly different imaging parameters (see discussion above in Section 5.2.2), for moving from ex-vivo training data to an in-vivo application, an extensive in-vivo study would be required to determine the robustness of the trained network. Larger amounts of training data with a high data variety could make the model more robust and improve the performance on previously unseen data and acquisition scenarios.

The d-FLASH contrast leveraged in the second method to circumvent the need for a baseline acquisition is sensitive to local magnetic field gradients as they appear near a metallic needle (see Section 2.3.2). A forward model-based localization technique, as proposed for a baseline-subtracted k-space acquisition, could potentially also be employed to model the d-FLASH image of a needle insertion. However, while signal from areas with a homogeneous magnetic field (background signal) is generally suppressed with d-FLASH contrast, some image intensity unrelated to the needle can remain (as could be seen in Fig. 4.9 and Fig. 4.10). This residual signal can, e.g., be attributed to other susceptibility interfaces in the imaged volume [19] or partial volume effects [24]. If a voxel is partially filled with different tissue material, or located at an air/tissue interface, the WM gradient moment will only partially dephase the magnetization of a respective tissue in the voxel which can cause residual signal intensity to remain. Accidental rephasing of signal by the employed WM gradient moment at fat/muscle tissue interfaces, where fat and water in the muscle tissue experience a different PRF (chemical shift effect), can also induce undesired residual signal intensity [24, 101]. Residual, non-suppressed image intensities, appearing in addition to the WM needle artifact, would be challenging to included into a handcrafted forward model of the image or k-space, such as the proposed 3D sinc model in Section 3.2. An alternative to such a handcrafted model is the employment of a ML-based approach, as used for the second needle localization method investigated in this dissertation,

which can recognize the needle artifact, but also discern WM artifacts unrelated to the needle, as was shown by the successful localizations.

In the past, different methods for 3D passive MR needle localization to allow for ASP have been investigated, which shall be compared to the approaches investigated in this dissertation. Reichert et al. attached a passive marker to a needle outside the body [30] and used two undersampled 2D tracking slices and a cross-correlation approach [29] to identify the marker position in the undersampled images. They achieved a mean localization accuracy of $1\,\mathrm{mm}$, collecting a total of 4 radial k-space lines. The method, as it relies on an external marker and pre-positioned tracking slice, could be too restrictive for some workflows as opposed to a direct 3D needle localization, e.g., employing localization concept as introduced in this work. Additionally, since the marker is tracked instead of the needle, potential bending of the needle within body tissues must be accounted for. Zijlstra et al. used phase-correlation (similar to Reichert et al.) to track a needle tip in undersampled 2D d-FLASH images [31]. A fully-3D correlation approach (avoiding the use of 2D tracking slices) might come with certain pitfalls such as, e.g., a potential requirement of a large dictionary of templates to exhaustively include different needle orientations and lengths, potentially rendering a full 3D template-based technique challenging for ASP. Patil et al. successfully localized a paramagnetic marker, attachable to interventional devices, using three echo-dephased spatial projections (concept similar to dephased GRE imaging), achieving an accuracy of $4.5\,\mathrm{mm}$ [102]. Their approach was intended to localize only a single marker on a device and, therefore, no information on the device orientation was extracted. In recent work, using d-FLASH imaging for needles with several susceptibility markers, together with CNN-based localization, was shown to be a promising extension of the work conducted in this dissertation [98] (see discussion above in Section 5.2.2 on how to overcome the angular range restriction for the investigated d-FLASH-based needle localization approach). Mehrtash et al. proposed a 3D CNN-based method [32] (similar architecture to the approach investigated in this work) to segment the needle artifact from 3D spin-echo images (resampled to res $= 0.88\,\mathrm{mm} \times 0.88\,\mathrm{mm} \times 3.6\,\mathrm{mm}$) during prostate biopsies. The method allowed the determination of the position of the needle tip and the orientation of the needle trajectory. The authors attained a median accuracy of $0.88\,\mathrm{mm}$ for localizing the needle tip (not to be confused with the metric Δs evaluated for the localization methods in this work, which is the distance of the ground truth needle tip to the detected needle axis) and $0.68°$ median deviation in determining the trajectory orientation. With acquisition times of approximately one minute for the employed conventional spin-echo imaging, the approach by Mehrtash et al. is not optimized for real-time automatic slice alignment, which is the designated application for the rapid 3D needle localization methods investigated in this dissertation, but rather for needle placement verification/target hit confirmation. Li et al. employed a CNN-based needle localization method, localizing the needle in a $15\,\mathrm{mm}$ thick slab of three 2D slices. They achieved a median positional accuracy of $2.2\,\mathrm{mm}$ and an orientation accuracy of $1.2°$ [33]. Li et al.'s method requires some prior knowledge of the needle's position and orientation for initial imaging slice alignment, unlike the fully 3D CNN-based technique proposed in this work. Mehrtash et al.'s and Li et al.'s CNN-based approaches employ cross-entropy and dice loss functions for network training, which are common in segmentation challenges [86]. For the CNN-based approach investigated in this dissertation, an L^2 loss function was employed for network training which is prevalent in regression tasks [86, 88]. The MR needle artifact characteristics vary with the needle

type, material, and employed sequence parameters as discussed in Section 2.3 and the artifact, due to positional signal shifts, signal dephasing or the positive signal formation mechanism, might not necessarily coincide with the needle axis. CNNs have been shown to be capable of inferring the true location of the needle from the artifact [33]. Consequently, the goal of directly identifying the needle axis/vector from MR images could be seen as a regression task rather than a segmentation task, motivating the squared L^2 norm being employed as a loss function for network training. Also, whereas generating a Gaussian heatmap for the needle axis labels in a regression task merely requires marking two points in each feature image of the training dataset (label is automatically generated from annotated needle entry point and tip as described in Section 3.3), accurate binary segmentation of WM needle artifacts would require a labor-intensive 3D pixel annotation for each feature image in the training dataset, thereby making the annotation process less time-efficient. Recently, Zhou et al. [34] suggested the use of a vision transformer as an alternative to the CNN architecture for needle segmentation from 3D intra-procedural MR images. Their experiments yielded promising outcomes ($1.48\,\mathrm{mm}$ and 0.98° in median localization error for tip and axis, respectively). While their implementation was not intended for real-time applicable 3D localization for the purpose of slice realignment (acquisition time $13\,\mathrm{s}$), integrating transformer architecture could be a potential future development step in the 3D d-FLASH framework investigated in this dissertation. Employing a transformer architecture may also facilitate direct image-to-needle vector regression without a PCA post-processing step, whereas direct mappings between an image and a vector remains a challenge for CNN architectures [103]. However, additional training data might be necessary when employing a transformer architecture to achieve similar localization precision as with a CNN architecture [104]. The rapid 3D passive needle localization techniques investigated in this dissertation comprise a method which optimizes a model of baseline-subtracted FLASH k-space data to extract the localization parameters of a needle, as well as a CNN-based method to localize the needle in undersampled d-FLASH images.

In this dissertation, two methods for rapid 3D needle localization for the purpose of enabling ASP were proposed and investigated. Once the needle's position and orientation are determined by the algorithms, 2D real-time imaging planes can be aligned with the needle trajectory, ensuring the needle artifact is visible to the interventionalist in the real-time images. Without ASP, 2D real-time imaging planes must be adjusted manually, usually involving multiple iterative steps executed by an MR technician, which can be a time- and attention-demanding process, potentially impeding the workflow. A fast automatized approach, such as offered by the proposed methods, could therefore provide an acceleration and simplification of the workflow. While the feasibility of a successful localizations from a greatly undersampled k-space was shown with both methods (in some instances, localization was successful from 5 or 16 sampled k-space spokes), a localization from this greatly reduced number of sampled k-space spokes (compared to a fully-sampled k-space with the chosen acquisition scheme and parameters, sampling only 16 spokes would correspond to a 402-fold acceleration) is most likely not necessary for automated slice positioning in most use cases, as less aggressive undersampling would still allow the method to be rapid

enough to enhance needle intervention workflows. ASP was demonstrated retrospectively with both localization methods. Even a partial alignment of the imaging slice with the needle, as, e.g., for some of the alignments depicted in Fig. 4.10, could still be useful during an intervention. Even for the case of an imperfect automatic slice alignment, 3D needle localization methods, as investigated in this dissertation, could help minimize the manual adjustments needed to reposition the 2D imaging plane, e.g., for when the needle is not visible at all in the initially selected slice. This could happen, e.g., when there is a mismatch between the planned and actual needle trajectories or insertion points, or when patient movement causes the needle to exit the imaging slice (for motion, the CNN-based approach would be favorable, as discussed above). A partial alignment can either provide a starting point for manual fine-tuning of the slice alignment or be complemented by a method as proposed by Li et al. [33], which comprises capturing multiple adjacent slices to detect the needle and adjust for minor misalignments between needle and a real-time imaging slice. In case the automatic slice alignment fails, a reversion to the initial slice and a manual slice alignment could still serve as a fallback method. Employing one of the proposed localization methods for ASP during interventions, it is likely also not necessary to constantly update the alignment of the 2D real-time images, for example, by interleaving the radial FLASH or d-FLASH acquisition, used solely for automatic needle localization, with every acquisition of 2D real-time images, used for the image guidance of the intervention. Instead, ASP, and, therefore, a dedicated acquisition for localization, could be initiated by the user only when required. During an MR-guided intervention, the user could balance the the number of k-space spokes acquired to achieve a certain localization precision against the acceptable acquisition time required for the localization sequence. Another factor that can influence the visibility of the needle artifact is the chosen slice thickness for the automatically aligned 2D real-time imaging slice, as discussed above, and relaxing the constraint on a thin slice could make the artifact visible for some cases of partial needle alignment. The two investigated methods for rapid 3D needle localization could also complement 2D needle tracking techniques. Submillimeter precision for localization of the needle tip and determination of the needle's orientation within a 2D plane to an accuracy of about one degree have been reached with existing 2D needle localization methods [31, 89, 105]. However, any 2D technique requires prior knowledge on position and orientation of the image slice that includes the needle. In contrast, fully-3D methods, as investigated in this dissertation, can allow for a needle localization without requiring prior location information, or, with limited prior information (initial parameters for optimization in Section 3.2), enabling the automated positioning of a 2D imaging slice aligned with the needle. Compared with 2D needle tracking techniques for MR-guided interventions, the proposed rapid 3D localization methods can therefore also be seen to offer a complementary solution: Rapid 3D methods, such as the two proposed methods, could be incorporated into real-time imaging sequences as a tracking module, allowing for fast slice realignment when the needle is lost or not entirely visible in the 2D real-time image. After ASP using a fast 3D localization, a 2D tracking technique can then monitor the needle's movement within the 2D imaging slice for precise needle tip localization in order to accurately assess the tip-to-target distance based on the MR image or to confirm if a target was hit. Any 2D localization technique, however, requires visibility of the artifact in the selected 2D plane, which, in case of plane misalignment, can then be restored with a 3D localization technique.

6 Conclusion

In this work, methods were investigated to enable rapid 3D passive needle localization for the purpose of automatic slice alignment during MR-guided interventions.

In a first step, the MR image artifact generated by a metallic needle was characterized for conventional GRE imaging using FLASH contrast, as well as for positive, susceptibility-based contrast imaging using dephased GRE. The hypointensive FLASH needle artifact was well described with a dephased disk/dephased cylinder model. When comparing positive needle artifacts for three different variants of dephased GRE, it was shown that d-bSSFP exhibits a higher cumulated signal magnitude and increased signal symmetry compared to d-SSFP and d-FLASH and greater signal homogeneity than d-SSFP, but potentially suffers from eddy current-induced artifacts for radial sampling strategies.

In a next step, a 3D needle localization method was proposed and implemented that models a baseline-subtracted 3D FLASH acquisition and uses an optimization procedure to find the best fitting model parameters corresponding to the orientation and position of the needle. A 3D sinc was used to model the subtraction k-space, corresponding to a cuboid in image space, which approximates the cylindrical needle artifact. Inter-acquisition motion after the baseline scan could lead to a corrupted subtraction k-space and will likely require the implementation of motion compensation strategies. Feasibility of successful needle localization from a very low number of acquired k-space spokes was shown for needle insertions within a limited range of inclination angles near the transversal plane and ASP was successfully performed retrospectively in an ex-vivo tissue sample, as well as in an in-vivo proof-of-principle demonstration case.

Based on an undersampled d-FLASH image acquisition, a second localization method was proposed and implemented that does not require a baseline scan, employing a CNN-based algorithm for needle localization. In an ex-vivo study, localization accuracy was found to be reduced for needle orientations increasingly tilted towards the direction of $\vec{G}_{\mathrm{WM}}$ and $\vec{B}_0$, which could be partially balanced by longer acquisition times (less undersampling). Successful needle localization based on highly undersampled images was shown for trajectories near the transversal plane and ASP was retrospectively demonstrated for examples from the ex-vivo dataset and in in-vivo animal experiments.

Both localization techniques were retrospectively shown to allow for ASP. The methods were accelerated to real-time applicability. Therefore, they offer the potential to accelerate and facilitate needle intervention workflows in the future.

Appendix

A.1 Closed solutions to dephased GRE signal models

As described in Section 2.2.3, the signal equations Eq. 2.63 describe the mean voxel signal magnitude for the three investigated dephased GRE sequences. The solution for d-FLASH contrast is the well-known sinc function, which is shifted so that the maximum signal appears at full gradient moment compensation $\gamma m_{0,\mathrm{susc}} = \gamma m_{0,\mathrm{WM}}$ [20]. For d-SSFP and d-bSSFP, a closed solution is provided in the following (up to first signal maximum at $\gamma m_{0,\mathrm{susc}} = \pm\frac{2\pi}{\Delta z}$ for $\bar{S}_{\text{d-bSSFP}}$):

$$
\begin{aligned}
\bar{S}_{\text{d-FLASH}} &= S_{\text{SSI}} \left| \int \mathrm{rect}\left(\frac{z}{\Delta z}\right) * e^{-i(\gamma m_{0,\mathrm{susc}} - \frac{2\pi}{\Delta z})z} \mathrm{d}z \right| \\
&= S_{\text{SSI}} \left| \mathrm{sinc}\left(\gamma m_{0,\mathrm{susc}} \Delta z/2 - \pi\right) \right| \\
\\
\bar{S}_{\text{d-SSFP}} &= S_{\text{SSC}} \frac{\int_0^{2\pi} \left| \int \mathrm{rect}\left(\frac{z}{\Delta z}\right) * e^{-i\,\mathrm{SW}((\gamma m_{0,\mathrm{susc}} - \frac{2\pi}{\Delta z})z + \tau)} \mathrm{d}z \right| \mathrm{d}\tau}{2\pi} \\
&= S_{\text{SSC}} \begin{cases} 1 & \text{for } \gamma m_{0,\mathrm{susc}} \Delta z = -2\pi \\ \frac{\mathrm{tri}(\mathrm{mod}(\gamma m_{0,\mathrm{susc}} \Delta z, 2\pi)/\pi - 1)}{|\gamma m_{0,\mathrm{susc}} \Delta z + 2\pi|/\pi} \left(1 - \frac{\mathrm{tri}(\mathrm{mod}(\gamma m_{0,\mathrm{susc}} \Delta z, 2\pi)/\pi - 1)}{2}\right) & \text{for } \gamma m_{0,\mathrm{susc}} \Delta z \neq -2\pi \end{cases} \\
\\
\bar{S}_{\text{d-bSSFP}} &= S_{\text{SSC}} \frac{\int_0^{2\pi} \left| \int \mathrm{rect}(\frac{z}{\Delta z}) * e^{-i(\mathrm{SW}(\gamma m_{0,\mathrm{susc}} z + \tau) - \frac{2\pi}{\Delta z} z)} \mathrm{d}z \right| \mathrm{d}\tau}{2\pi} \\
&= S_{\text{SSC}} \begin{cases} \frac{4}{\pi^3} |\gamma m_{0,\mathrm{susc}} \Delta z| & \text{for } |\gamma m_{0,\mathrm{susc}} \Delta z| < \pi \\ \frac{2|\gamma m_{0,\mathrm{susc}} \Delta z|}{\pi^3} (\cos(\frac{\pi}{\gamma m_{0,\mathrm{susc}} \Delta z} \mathrm{mod}(|\gamma m_{0,\mathrm{susc}} \Delta z|, \pi)) - \cos(\frac{\pi^2}{\gamma m_{0,\mathrm{susc}} \Delta z})) & \\ \quad + \frac{2}{\pi^2} \sin(\frac{\pi^2}{|\gamma m_{0,\mathrm{susc}} \Delta z|}) \mathrm{mod}(|\gamma m_{0,\mathrm{susc}} \Delta z|, \pi) & \text{for } \pi \leq |\gamma m_{0,\mathrm{susc}} \Delta z| < 2\pi \\ \frac{2}{\pi} & \text{for } |\gamma m_{0,\mathrm{susc}} \Delta z| = 2\pi \end{cases}
\end{aligned}
\tag{A.1}
$$

Here, rect is the rectangular function ($\mathrm{rect}(x) = 1$ for $|x| < 0.5$; $\mathrm{rect}(x) = 0.5$ for $x = \pm 0.5$; $\mathrm{rect}(x) = 0$ elsewhere); tri is the triangular function ($\mathrm{tri}(x) = \max(1 - |x|, 0)$); and $\mathrm{mod}(a, b)$ describes the modulo operation. For the signal maximum, the signal magnitude is, therefore, given by $\bar{S}_{\text{d-bSSFP}}(\gamma m_{0,\mathrm{susc}} = \pm\frac{2\pi}{\Delta z}) \approx 0.64 S_{\text{SSC}}$.

A.2 Reparametrization of subtraction k-space needle model

For the implementation of the optimization procedure for the localization algorithm described in Section 3.2.1, Eq. 3.2 was reparametrized by expressing the vector $\hat{\vec{v}}_{c,0}$ in terms of the angles θ

and ϕ:

$$\hat{\vec{v}}_{c,0} = \cos\theta\cos\phi\vec{e}_x + \cos\theta\sin\phi\vec{e}_y + \sin\theta\vec{e}_z \tag{A.2}$$

with the unit vectors $\vec{e}_x, \vec{e}_y$ and $\vec{e}_z$ along the coordinate axes. To determine the two vectors $\hat{\vec{v}}_{c,1}$ and $\hat{\vec{v}}_{c,2}$, which are defined as orthonormal to $\hat{\vec{v}}_{c,0}$, the Gram-Schmidt process (see, e.g., [106]) is used which is initialize with a random vector $\vec{u}$, e.g., $\vec{u} = (1, 1, 1)$. For the vector $\hat{\vec{v}}_{c,1}$, we find

$$\begin{aligned} \vec{v}_{c,1} &= \vec{u} - \frac{\langle \vec{u}, \hat{\vec{v}}_{c,0} \rangle}{\langle \vec{u}, \vec{u} \rangle} \vec{u} \\ \hat{\vec{v}}_{c,1} &= \frac{\vec{v}_{c,1}}{|\vec{v}_{c,1}|}, \end{aligned} \tag{A.3}$$

and for the vector $\hat{\vec{v}}_{c,1}$, we find

$$\begin{aligned} \vec{v}_{c,2} &= \hat{\vec{v}}_{c,0} \times \hat{\vec{v}}_{c,1} \\ \hat{\vec{v}}_{c,2} &= \frac{\vec{v}_{c,2}}{|\vec{v}_{c,2}|}. \end{aligned} \tag{A.4}$$

A.3 Accuracy for forward model-based localization by angular orientation

Figure A.1 depicts the localization accuracy (Δs), broken down by angular orientation of the inserted needle, for the ex-vivo study investigating the proposed forward model-based needle localization method.

A.4 Model loss of CNN used for needle localization

Figure A.2 depicts the training and validation loss curves for the trained CNNs. A seperate CNN was trained for the different employed undersampling factors (d-FLASH images reconstructed from $n_{\text{spokes}1}$ to $n_{\text{spokes}6}$).

In Table A.1, the model losses are reported for the training, validation and test sets. As explained in Section 3.3, the test set was binned for the needle inclination angle θ.

Initial parameter set 1

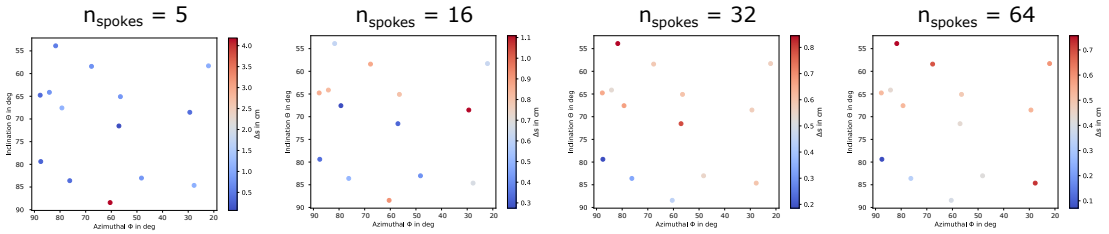

Initial parameter set 2

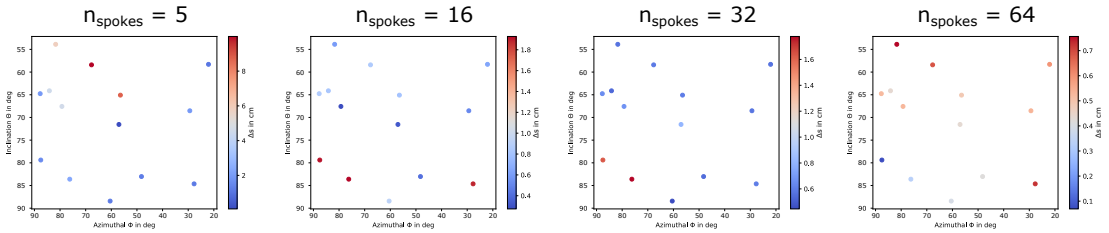

Initial parameter set 3

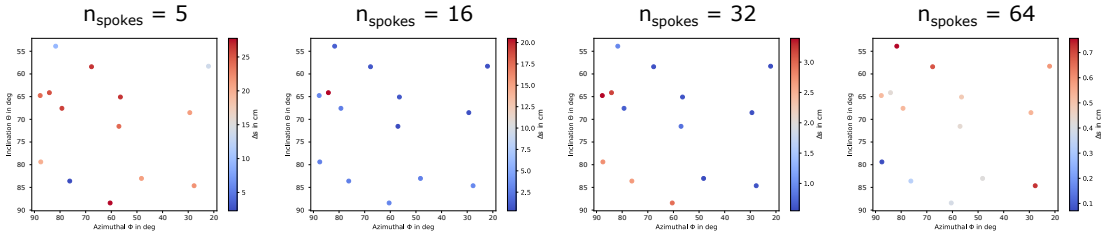

Figure A.1: Localization accuracy (Δs), broken down by angular orientation of the inserted needle, for the ex-vivo study investigating the proposed forward model-based needle localization method. Each insertion is plotted as a datapoint with its coordinates indicating the needle angles ϕ and θ, as defined in Fig. 3.4. The accuracy for Δs is color-coded. Note the different ranges of the colorbars. Accuracy is given for localization from the different sets of initial optimization parameters 1-3 (see Section 3.2) and different numbers n_{spokes} of sampled k-space lines. Angles $\theta > 90°$ and $\phi > 90°$ were mapped to the interval $[0°, 90°]$ by deriving $180° - \theta$ and $180° - \phi$, respectively.

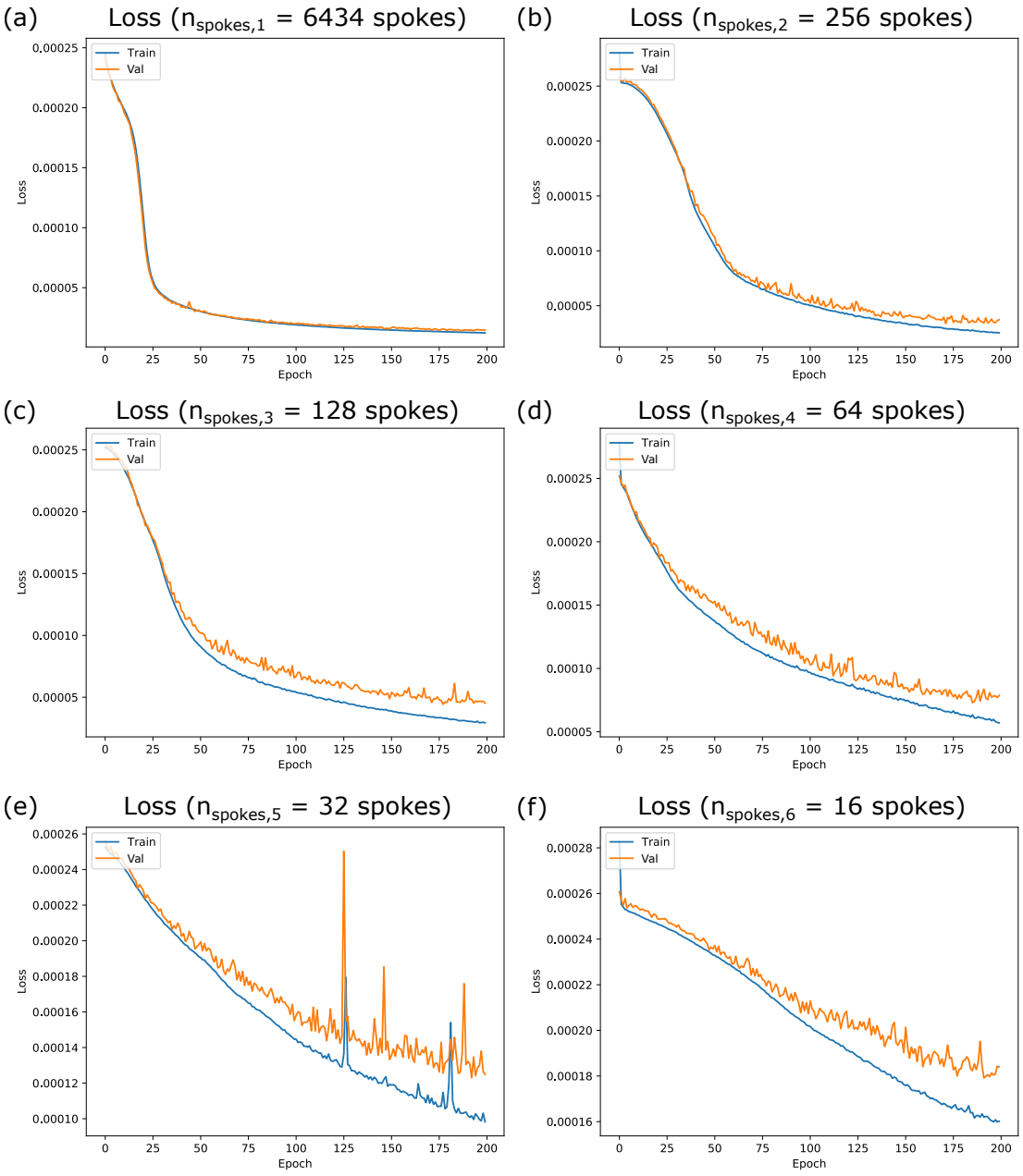

Figure A.2: Plots depict the development of the training and validation loss for the implemented CNN. Seperate models were trained over 200 epochs with d-FLASH images reconstructed from (a) $n_{\text{spokes},1} = 6434$, (b) $n_{\text{spokes},2} = 256$, (c) $n_{\text{spokes},3} = 128$, (d) $n_{\text{spokes},4} = 64$, (e) $n_{\text{spokes},5} = 32$ and (f) $n_{\text{spokes},6} = 16$.

	6434 spokes (fully sampled)	256 spokes	128 spokes	64 spokes	32 spokes	16 spokes
Training dataset						
n = 926 (augmented data)	1.23e-05	2.53e-05	2.93e-05	5.70e-05	9.82e-05	1.60e-04
Validation dataset						
n = 102 (augmented data)	1.46e-05	3.72e-05	4.53e-05	7.88e-05	1.25e-04	1.84e-04
Ex-vivo test dataset						
n = 36 θ ∈ (86°,90°]	9.47e-05	5.17e-05	4.29e-05	7.63e-05	9.00e-05	1.35e-04
n = 40 θ ∈ (82°,86°]	7.77e-05	6.42e-05	7.91e-05	1.07e-04	1.53e-04	2.00e-04
n =33 θ ∈ (78°,82°]	7.63e-05	8.42e-05	1.12e-04	1.34e-04	1.83e-04	2.57e-04
In-vivo experiments						
(a)	2.21e-04	2.81e-04	3.15e-04	5.35e-04	3.79e-04	6.42e-04
(b)	1.54e-04	1.50e-04	2.05e-04	3.81e-04	3.93e-04	3.88e-04
(c)	1.00e-04	3.21e-04	4.62e-04	5.04e-04	5.10e-04	5.05e-04

Table A.1: Model loss of CNN, employed for needle localization as described in Section 3.3, for training, validation and ex-vivo test set, as well as for proof-of-principle in-vivo needle insertions. As described in Section 3.3, the test set was binned for the needle inclination angle θ.

Bibliography

[1] Jonas Frederik Faust et al. “Needle Artifact Prediction by Modeling Dephasing in MR-Guided Interventions.” In: *Proceedings of the 33rd Annual Meeting of ISMRM*. Singapore, 2024, p. 2395.

[2] Jonas Frederik Faust et al. “Positive susceptibility-based contrast imaging with dephased balanced steady-state free precession.” In: *Magnetic Resonance in Medicine* 94.1 (2025), pp. 59–72.

[3] Jonas Frederik Faust et al. “Model-Based Rapid 3D Passive Needle Localization for Automatic Slice Positioning in MR-Guided Interventions.” In: *Proceedings of the 33rd Annual Meeting of ISMRM*. Singapore, 2024, p. 0456.

[4] Jonas Frederik Faust et al. “Rapid CNN-based needle localization for automatic slice alignment in MR-guided interventions using 3D undersampled radial white-marker imaging.” In: *Medical Physics* 51.11 (2024), pp. 8018–8033.

[5] Clifford R. Weiss, Sherif Gamal Nour, and Jonathan S. Lewin. “MR-guided biopsy: A review of current techniques and applications.” In: *Journal of Magnetic Resonance Imaging* 27.2 (2008), pp. 311–325.

[6] Sohrab Afshari Mirak and Steven S. Raman. “MRI-guided interventional procedures: current use and future potentials.” In: *European Radiology* 33.8 (2023), pp. 5717–5718.

[7] Andrea Veltri et al. “CIRSE Guidelines on Percutaneous Needle Biopsy (PNB).” In: *CardioVascular and Interventional Radiology* 40.10 (2017), pp. 1501–1513.

[8] Eva Rothgang et al. “Rapid freehand MR-guided percutaneous needle interventions: An image-based approach to improve workflow and feasibility.” In: *Journal of Magnetic Resonance Imaging* 37.5 (2013), pp. 1202–1212.

[9] Mark E. Ladd et al. “Biopsy needle susceptibility artifacts.” In: *Magnetic Resonance in Medicine* 36.4 (1996), pp. 646–651.

[10] K M Lüdeke, P Röschmann, and R Tischler. “Susceptibility artefacts in NMR imaging.” In: *Magnetic Resonance Imaging* 3.4 (1985), pp. 329–343.

[11] Stefan Posse and Walter P. Aue. “Susceptibility artifacts in spin-echo and gradient-echo imaging.” In: *Journal of Magnetic Resonance Imaging* 88.3 (1990), pp. 473–492.

[12] J S Lewin et al. “Needle localization in MR-guided biopsy and aspiration: effects of field strength, sequence design, and magnetic field orientation.” In: *American Journal of Roentgenology* 166.6 (1996), pp. 1337–1345.

[13] Christian Frahm et al. “Visualization of magnetic resonance-compatible needles at 1.5 and 0.2 Tesla.” In: *Cardiovascular and Interventional Radiology* 19.5 (1996), pp. 335–340.

[14] Tobias Penzkofer et al. “How MRI Compatible is “MRI Compatible”? A Systematic Comparison of Artifacts Caused by Biopsy Needles at 3.0 and 1.5 T.” In: *CardioVascular and Interventional Radiology* 36.6 (2013), pp. 1646–1657.

[15] Vanessa Franziska Schmidt et al. “Artifact reduction of coaxial needles in magnetic resonance imaging-guided abdominal interventions at 1.5 T: a phantom study.” In: *Scientific Reports* 11.1 (2021), p. 22963.

[16] Bernd Müller-Bierl et al. “Numerical modeling of needle tip artifacts in MR gradient echo imaging.” In: *Medical Physics* 31.3 (2004), pp. 579–587.

[17] A. Glowinski et al. “A perspective on needle artifacts in MRI: an electromagnetic model for experimentally separating susceptibility effects.” In: *IEEE Transactions on Medical Imaging* 19.12 (2000), pp. 1248–1252.

[18] E. P.A. Vonken et al. “Direct in vitro comparison of six three-dimensional positive contrast methods for susceptibility marker imaging: Comparison of Positive Contrast Methods.” In: *Journal of Magnetic Resonance Imaging* 38.2 (2013), pp. 344–357.

[19] Jan-Henry Seppenwoolde, Max A. Viergever, and Chris J.G. Bakker. “Passive tracking exploiting local signal conservation: The white marker phenomenon.” In: *Magnetic Resonance in Medicine* 50.4 (Oct. 2003), pp. 784–790.

[20] Chris J G Bakker, Jan-Henry Seppenwoolde, and Koen L Vincken. “Dephased MRI.” In: *Magnetic Resonance in Medicine* 55.1 (2006), pp. 92–97.

[21] Sunil Patil, Oliver Bieri, and Klaus Scheffler. “Echo-dephased steady state free precession.” In: *Magnetic Resonance Materials in Physics, Biology and Medicine* 22.5 (2009), pp. 277–285.

[22] Matthias Stuber et al. “Positive contrast visualization of iron oxide-labeled stem cells using inversion-recovery with ON-resonant water suppression (IRON).” In: *Magnetic Resonance in Medicine* 58.5 (2007), pp. 1072–1077.

[23] Hannes Dahnke et al. “Susceptibility gradient mapping (SGM): A new postprocessing method for positive contrast generation applied to superparamagnetic iron oxide particle (SPIO)-labeled cells.” In: *Magnetic Resonance in Medicine* 60.3 (2008), pp. 595–603.

[24] Jan-Henry Seppenwoolde, Koen L. Vincken, and Chris J.G. Bakker. “White-marker imaging—Separating magnetic susceptibility effects from partial volume effects.” In: *Magnetic Resonance in Medicine* 58.3 (2007), pp. 605–609.

[25] Adrienne E Campbell-Washburn et al. “Dual echo positive contrast bSSFP for real-time visualization of passive devices duringmagnetic resonance guided cardiovascular catheterization.” In: *Journal of Cardiovascular Magnetic Resonance* 16.1 (2014), p. 88.

[26] Jonathan Weine et al. “Interleaved White Marker Contrast with bSSFP Real-Time Imaging for Deep Learning based Needle Localization in MR-Guided Percutaneous Interventions.” In: *Proceedings of the 27th Annual Meeting of ISMRM*. Montréal, QC, Canada, 2019, p. 3832.

[27] Simon Reiß et al. “To Spoil or To Balance? A Comparison of the White Marker Phenomenon in Gradient Echo Pulse Sequences.” In: *Proceedings of the 23th Annual Meeting of ISMRM*. Toronto, ON, Canada, 2015, p. 4160.

[28] Mark E. Ladd and Harald H. Quick. “Reduction of resonant RF heating in intravascular catheters using coaxial chokes.” In: *Magnetic Resonance in Medicine* 43.4 (2000), pp. 615–619.

[29] André De Oliveira et al. “Automatic passive tracking of an endorectal prostate biopsy device using phase-only cross-correlation.” In: *Magnetic Resonance in Medicine* 59.5 (2008), pp. 1043–1050.

[30] Andreas Reichert et al. “Passive needle guide tracking with radial acquisition and phase-only cross-correlation.” In: *Magnetic Resonance in Medicine* 85.2 (2021), pp. 1039–1046.

[31] Frank Zijlstra, Max A. Viergever, and Peter R. Seevinck. “SMART tracking: Simultaneous anatomical imaging and real-time passive device tracking for MR-guided interventions.” In: *Physica Medica* 64 (2019), pp. 252–260.

[32] Alireza Mehrtash et al. “Automatic Needle Segmentation and Localization in MRI With 3-D Convolutional Neural Networks: Application to MRI-Targeted Prostate Biopsy.” In: *IEEE Transactions on Medical Imaging* 38.4 (2019), pp. 1026–1036.

[33] Xinzhou Li et al. “Physics-Driven Mask R-CNN for Physical Needle Localization in MRI-Guided Percutaneous Interventions.” In: *IEEE Access* 9 (2021), pp. 161055–161068.

[34] Wenqi Zhou et al. “Deep learning-based automatic pipeline for 3D needle localization on intra-procedural 3D MRI.” In: *International Journal of Computer Assisted Radiology and Surgery* (2024).

[35] W Strehl et al. “A Passive, Image-Based Navigation Tool for Real-Time Mr-Guided Percutaneous Interventional Procedures.” In: *Proceedings of the 18th Annual Meeting of ISMRM*. Stockholm, 2010, p. 969.

[36] Sebastian Schmitt et al. “Passive 3D Needle Tip Tracking in Freehand MR-Guided Interventions with Needle Model Visualization.” In: *Bildverarbeitung für die Medizin 2015*. Ed. by Heinz Handels et al. Berlin, Heidelberg, 2015, pp. 89–94.

[37] Charles P. Slichter. *Principles of Magnetic Resonance*. Red. by Manuel Cardona et al. Vol. 1. Springer Series in Solid-State Sciences. Berlin, Heidelberg: Springer Berlin Heidelberg, 1990.

[38] Robert W. Brown et al. *Magnetic Resonance Imaging: Physical Principles and Sequence Design*. Hoboken, NY: Wiley, 2014.

[39] Matt A. Bernstein, Kevin F. King, and Xiaohong Joe Zhou. *Handbook of MRI Pulse Sequences*. Elsevier, 2004.

[40] Pieter Zeeman. “Ueber einen Einfluss der Magnetisirung auf die Natur des von einer Substanz emittirten Lichtes.” In: *Verhandlungen der Physikalischen Gesellschaft zu Berlin*. 1896, pp. 128–130.

[41] F. Bloch. “Nuclear Induction.” In: *Physical Review* 70.7 (1946), pp. 460–474.

[42] E. M. Purcell, H. C. Torrey, and R. V. Pound. “Resonance Absorption by Nuclear Magnetic Moments in a Solid.” In: *Physical Review* 69.1 (1946), pp. 37–38.

[43] I. I. Rabi et al. “A New Method of Measuring Nuclear Magnetic Moment.” In: *Physical Review* 53.4 (1938), pp. 318–318.

[44] P. C. Lauterbur. “Image Formation by Induced Local Interactions: Examples Employing Nuclear Magnetic Resonance.” In: *Nature* 242.5394 (1973), pp. 190–191.

[45] H. Nyquist. “Certain Topics in Telegraph Transmission Theory.” In: *Transactions of the American Institute of Electrical Engineers* 47.2 (1928), pp. 617–644.

[46] Dennis L. Parker, Yiping P. Du, and Wayne L. Davis. “The Voxel Sensitivity Function in Fourier Transform Imaging: Applications to Magnetic Resonance Angiography.” In: *Magnetic Resonance in Medicine* 33.2 (1995), pp. 156–162.

[47] James W. Cooley and John W. Tukey. “An algorithm for the machine calculation of complex Fourier series.” In: *Mathematics of Computation* 19.90 (1965), pp. 297–301.

[48] John M. Pauly. “Gridding & the NUFFT for Non-Cartesian Image Reconstruction.” In: *Proceedings of the 21st Annual Meeting of ISMRM*. Salt Lake City, USA, 2013.

[49] Kai Tobias Block. “Advanced methods for radial data sampling in magnetic resonance imaging.” PhD thesis. Universität Göttingen, 2008.

[50] J. D. O’Sullivan. “A Fast Sinc Function Gridding Algorithm for Fourier Inversion in Computer Tomography.” In: *IEEE Transactions on Medical Imaging* 4.4 (1985), pp. 200–207.

[51] J.I. Jackson et al. “Selection of a convolution function for Fourier inversion using gridding (computerised tomography application).” In: *IEEE Transactions on Medical Imaging* 10.3 (1991), pp. 473–478.

[52] P.J. Beatty, D.G. Nishimura, and J.M. Pauly. “Rapid gridding reconstruction with a minimal oversampling ratio.” In: *IEEE Transactions on Medical Imaging* 24.6 (2005), pp. 799–808.

[53] James G. Pipe and Padmanabhan Menon. “Sampling density compensation in MRI: Rationale and an iterative numerical solution.” In: *Magnetic Resonance in Medicine* 41.1 (1999), pp. 179–186.

[54] Jinil Park et al. “Strategies for rapid reconstruction in 3D MRI with radial data acquisition: 3D fast Fourier transform vs two-step 2D filtered back-projection.” In: *Scientific Reports* 10.1 (2020), p. 13813.

[55] E. L. Hahn. “Spin Echoes.” In: *Physical Review* 80.4 (1950), pp. 580–594.

[56] Brian Hargreaves. “Rapid gradient-echo imaging.” In: *Journal of Magnetic Resonance Imaging* 36.6 (2012), pp. 1300–1313.

[57] A Haase et al. “FLASH imaging. Rapid NMR imaging using low flip-angle pulses.” In: *Journal of Magnetic Resonance (1969)* 67.2 (1986), pp. 258–266.

[58] Y. Zur, M. L. Wood, and L. J. Neuringer. “Spoiling of transverse magnetization in steady-state sequences.” In: *Magnetic Resonance in Medicine* 21.2 (1991), pp. 251–263.

[59] R. R. Ernst and W. A. Anderson. “Application of Fourier Transform Spectroscopy to Magnetic Resonance.” In: *Review of Scientific Instruments* 37.1 (1966), pp. 93–102.

[60] H. Y. Carr. “Steady-State Free Precession in Nuclear Magnetic Resonance.” In: *Physical Review* 112.5 (1958), pp. 1693–1701.

[61] A. Oppelt et al. “FISP: eine neue schnelle Pulssequenz für die Kernspintomographie.” In: *Electromedia* 54 (1986), pp. 15–18.

[62] Klaus Scheffler. “On the transient phase of balanced SSFP sequences.” In: *Magnetic Resonance in Medicine* 49.4 (2003), pp. 781–783.

[63] Carl Ganter. “Off-resonance effects in the transient response of SSFP sequences.” In: *Magnetic Resonance in Medicine* 52.2 (2004), pp. 368–375.

[64] Klaus Scheffler and Stefan Lehnhardt. “Principles and applications of balanced SSFP techniques.” In: *European Radiology* 13.11 (2003), pp. 2409–2418.

[65] M Deimling and O Heid. “Magnetization prepared true FISP imaging.” In: *Proceedings of the 2nd Scientific Meeting of ISMRM*. San Francisco, California, USA, 1994, p. 495.

[66] Govind B. Chavhan et al. “Steady-State MR Imaging Sequences: Physics, Classification, and Clinical Applications.” In: *RadioGraphics* 28.4 (2008), pp. 1147–1160.

[67] Ray Freeman and H.D.W Hill. “Phase and intensity anomalies in fourier transform NMR.” In: *Journal of Magnetic Resonance (1969)* 4.3 (1971), pp. 366–383.

[68] Klaus Scheffler and Jürgen Hennig. “Is TrueFISP a gradient-echo or a spin-echo sequence?” In: *Magnetic Resonance in Medicine* 49.2 (2003), pp. 395–397.

[69] R. Marc Lebel, Ravi S. Menon, and Chris V. Bowen. “Relaxometry model of strong dipolar perturbers for balanced-SSFP: Application to quantification of SPIO loaded cells.” In: *Magnetic Resonance in Medicine* 55.3 (2006), pp. 583–591.

[70] Venkatesh Mani et al. “Gradient echo acquisition for superparamagnetic particles with positive contrast (GRASP): Sequence characterization in membrane and glass superparamagnetic iron oxide phantoms at 1.5T and 3T.” In: *Magnetic Resonance in Medicine* 55.1 (2006), pp. 126–135.

[71] John David Jackson. *Classical electrodynamics*. Hoboken, NY: Wiley, 2009. 808 pp.

[72] Jonas Frederik Faust et al. “Analytical estimation of artifact radius for an MR-compatible aspiration biopsy Needle.” In: *Proceedings of the 6th conference on Image-Guided Interventions (IGIC)*. Mannheim, Germany, 2023.

[73] Oliver Bieri and Klaus Scheffler. “Fundamentals of balanced steady state free precession MRI: Fundamentals of Balanced SSFP MRI.” In: *Journal of Magnetic Resonance Imaging* 38.1 (2013), pp. 2–11.

[74] Eyal Kochavi, Dorith Goldsher, and Haim Azhari. “Method for rapid MRI needle tracking.” In: *Magnetic Resonance in Medicine* 51.5 (2004), pp. 1083–1087.

[75] Rn Bracewell. “Strip Integration in Radio Astronomy.” In: *Australian Journal of Physics* 9.2 (1956), p. 198.

[76] Adam J. Griebel et al. “Magnetic Susceptibility of Common Metals and Alloys Used in Medical Devices.” In: *Journal of Testing and Evaluation* 51.6 (2023), pp. 4554–4566.

[77] John F. Schenck. “The role of magnetic susceptibility in magnetic resonance imaging: MRI magnetic compatibility of the first and second kinds.” In: *Medical Physics* 23.6 (1996), pp. 815–850.

[78] Jochen Leupold, Jürgen Hennig, and Klaus Scheffler. “Moment and direction of the spoiler gradient for effective artifact suppression in RF-spoiled gradient echo imaging.” In: *Magnetic Resonance in Medicine* 60.1 (2008), pp. 119–127.

[79] Parmede Vakil et al. “Magnetization spoiling in radial FLASH contrast-enhanced MR digital subtraction angiography.” In: *Journal of Magnetic Resonance Imaging* 36.1 (2012), pp. 249–258.

[80] Rachel W. Chan et al. “Temporal stability of adaptive 3D radial MRI using multidimensional golden means.” In: *Magnetic Resonance in Medicine* 61.2 (2009), pp. 354–363.

[81] Frank Ong and Michael Lustig. “SigPy: a python package for high performance iterative reconstruction.” In: *Proceedings of the 27th Annual Meeting of ISMRM*. Montréal, QC, Canada, 2019, p. 4819.

[82] Pauli Virtanen et al. “SciPy 1.0: fundamental algorithms for scientific computing in Python.” In: *Nature Methods* 17.3 (2020), pp. 261–272.

[83] J. A. Nelder and R. Mead. “A Simplex Method for Function Minimization.” In: *The Computer Journal* 7.4 (1965), pp. 308–313.

[84] Kunihiko Fukushima. “Neocognitron: A self-organizing neural network model for a mechanism of pattern recognition unaffected by shift in position.” In: *Biological Cybernetics* 36.4 (1980), pp. 193–202.

[85] Y. LeCun et al. “Backpropagation Applied to Handwritten Zip Code Recognition.” In: *Neural Computation* 1.4 (1989), pp. 541–551.

[86] Ian Goodfellow, Yoshua Bengio, and Aaron Courville. *Deep learning*. Adaptive computation and machine learning. Cambridge, Massachusetts: The MIT Press, 2016.

[87] Xavier Glorot, Antoine Bordes, and Yoshua Bengio. “Deep sparse rectifier neural networks.” In: *Proceedings of the fourteenth international conference on artificial intelligence and statistics*. Ed. by Geoffrey Gordon, David Dunson, and Miroslav Dudík. Vol. 15. Proceedings of machine learning research. Fort Lauderdale, FL, USA: PMLR, 2011, pp. 315–323.

[88] Christian Payer et al. “Regressing Heatmaps for Multiple Landmark Localization Using CNNs.” In: Medical Image Computing and Computer-Assisted Intervention – MICCAI 2016. Ed. by Sebastien Ourselin et al. Vol. 9901. Lecture Notes in Computer Science. Cham: Springer International Publishing, 2016, pp. 230–238.

[89] Jonathan Weine et al. “Deep Learning Based Needle Localization on Real-Time MR Images of Patients Acquired During MR-guided Percutaneous Interventions.” In: *Proceedings of the 27th Annual Meeting of ISMRM*. Montréal, QC, Canada, 2019, p. 0973.

[90] Geert Litjens et al. “A survey on deep learning in medical image analysis.” In: *Medical Image Analysis* 42 (2017), pp. 60–88.

[91] Olaf Ronneberger, Philipp Fischer, and Thomas Brox. “U-Net: Convolutional Networks for Biomedical Image Segmentation.” In: *Medical Image Computing and Computer-Assisted Intervention – MICCAI 2015*. Ed. by Nassir Navab et al. Basel: Springer International Publishing; 2015, pp. 234–241.

[92] Özgün Çiçek et al. “3D U-Net: Learning Dense Volumetric Segmentation from Sparse Annotation.” In: *Medical Image Computing and Computer-Assisted Intervention – MICCAI 2016*. Ed. by Sebastien Ourselin et al. Basel: Springer International Publishing; 2016, pp. 424–432.

[93] Yu Zhao et al. “Deep learning solution for medical image localization and orientation detection.” In: *Medical Image Analysis* 81 (2022), p. 102529.

[94] Klaus Scheffler and Jürgen Hennig. “Eddy current optimized phase encoding schemes to reduce artifacts in balanced SSFP imaging.” In: *Proceedings of the 11th Annual Meeting of ISMRM*. Toronto, 2003.

[95] O. Bieri et al. “Morphing steady-state free precession.” In: *Magnetic Resonance in Medicine* 58.6 (2007), pp. 1242–1248.

[96] Peter R. Mueller et al. “MR-guided Aspiration Biopsy: Needle Design and Clinical Trials.” In: *Radiology* 161.3 (1986), pp. 605–609.

[97] Rohan Dharmakumar, Ioannis Koktzoglou, and Debiao Li. “Generating positive contrast from off-resonant spins with steady-state free precession magnetic resonance imaging: theory and proof-of-principle experiments.” In: *Physics in Medicine and Biology* 51.17 (2006), pp. 4201–4215.

[98] Germen Wennemars et al. “Automatic 3D Localization of Passively Marked Needles using Under-Sampled Radial Positive Contrast Imaging and nnU-Net.” In: *Book of Abstracts of the 14th Interventional MRI Symposium*. Annapolis, MD, USA, 2024.

[99] T.S. Sorensen et al. “Accelerating the Nonequispaced Fast Fourier Transform on Commodity Graphics Hardware.” In: *IEEE Transactions on Medical Imaging* 27.4 (2008), pp. 538–547.

[100] Davide Castelvecchi. “Can we open the black box of AI?” In: *Nature* 538.7623 (2016), pp. 20–23.

[101] Jonas Frederik Faust et al. “Dephased bSSFP for the Delineation of Interventional Devices.” In: *Proceedings of the 32nd Annual Meeting of ISMRM*. Toronto, Canada, 2023, p. 4382.

[102] S. Patil et al. “Automatic slice positioning (ASP) for passive real-time tracking of interventional devices using projection-reconstruction imaging with echo-dephasing (PRIDE).” In: *Magnetic Resonance in Medicine* 62.4 (2009), pp. 935–942.

[103] Rosanne Liu et al. “An Intriguing Failing of Convolutional Neural Networks and the CoordConv Solution.” In: *Advances in Neural Information Processing Systems 31 (NeurIPS 2018)*. Montréal, Canada, 2018.

[104] Alexey Dosovitskiy et al. “An Image is Worth 16x16 Words: Transformers for Image Recognition at Scale.” In: *The Ninth International Conference on Learning Representations (ICLR 2021)*. 2021.

[105] Xinzhou Li et al. “Automatic needle tracking using Mask R-CNN for MRI-guided percutaneous interventions.” In: *International Journal of Computer Assisted Radiology and Surgery* 15.10 (2020), pp. 1673–1684.

[106] E. W. Cheney and David Kincaid. *Linear algebra: theory and applications*. Sudbury, Mass: Jones and Bartlett Publishers, 2009. 740 pp.

List of publications

Methods and results presented in this dissertation have been published in several peer-reviewed scientific conference and journal contributions listed below.

Journal publications:

- Jonas Frederik Faust et al. "Rapid CNN-based needle localization for automatic slice alignment in MR-guided interventions using 3D undersampled radial white-marker imaging." In: *Medical Physics* 51.11 (2024), pp. 8018–8033. The article was published under the CC-BY license (`https://creativecommons.org/licenses/by/4.0/`).
- Jonas Frederik Faust et al. "Positive susceptibility-based contrast imaging with dephased balanced steady-state free precession." In: *Magnetic Resonance in Medicine* 94.1 (2025), pp. 59-72. The article was published under the CC-BY license (`https://creativecommons.org/licenses/by/4.0/`).

Conference publications:

- Jonas Frederik Faust et al. "Fast 3D Passive Needle Localization for MR-Guided Interventions using Radial White Marker Acquisitions and CNN Postprocessing." In: *Proceedings of the 31st Annual Meeting of ISMRM*. London, United Kingdom, 2022, p. 1196.
- Jonas Frederik Faust et al. "Dephased bSSFP for the Delineation of Interventional Devices." In: *Proceedings of the 32nd Annual Meeting of ISMRM*. Toronto, Canada, 2023, p. 4382.
- Jonas Frederik Faust et al. "Analytical estimation of artifact radius for an MR-compatible aspiration biopsy Needle." In: Proceedings of the 6th conference on Image-Guided Interventions (IGIC). Mannheim, Germany, 2023.
- Jonas Frederik Faust et al. "Model-Based Rapid 3D Passive Needle Localization for Automatic Slice Positioning in MR-Guided Interventions." In: *Proceedings of the 33rd Annual Meeting of ISMRM*. Singapore, 2024, p. 0456.
- Jonas Frederik Faust et al. "Needle Artifact Prediction by Modeling Dephasing in MR-Guided Interventions." In: *Proceedings of the 33rd Annual Meeting of ISMRM*. Singapore, 2024, p. 2395.
- Jonas Frederik Faust et al. "Susceptibility-Based Positive Contrast Device Imaging With Dephased Balanced Steady-State Free Precession (d-bSSFP)." In: *Proceedings of the 40th Annual Meeting of ESMRMB*. Barcelona, Spain, 2024, p. 0026.

- Jonas Frederik Faust et al. “Rapid CNN-Based Needle Localization for Automatic Slice Alignment in MR-Guided Interventions using 3D Undersampled Radial White-Marker Imaging – Initial In-Vivo Results.” In: Proceedings of the 14th Interventional MRI Symposium. Annapolis, MD, United States, 2024.

Acknowledgements

Ich bedanke mich an dieser Stelle bei allen, ohne deren Unterstützung dieses Projekt nicht umzusetzen gewesen wäre:

Zunächst möchte ich mich bei meinem Doktorvater Prof. Dr. Mark E. Ladd bedanken für die Betreuung meines Promotionsprojektes und die Begutachtung meiner Dissertation. Bei Prof. Dr. Leif Schröder bedanke ich mich für die übernommene Zweitbegutachtung meiner Arbeit.

Bei Dr. Florian Maier bedanke ich mich für die Übernahme der Betreuung meiner Arbeit im Therapieteam von Siemens Healthineers MR.

Bei Dr. Arne Hengerer bedanke ich mich für das mir entgegengebrachte Vertrauen und die Anstellung als Doktorand in seinem Team.

Bei Dr. Axel Krafft, Dr. Peter Speier und Dr. Daniel Polak möchte ich mich für die kontinuierliche Unterstützung während meines Promotionsprojektes bedanken und dafür, dass ich bei Fragen und Problemen immer auf sie zählen konnte! Ihre Beratung und Expertise waren an vielen Stellen wegweisend für die erfolgreiche Durchführung meiner Forschungsarbeiten.

Des Weiteren möchte ich mich bei den Kollegen von Cook Medical Dr. Jesse Roll, Joshua Krieger, Dr. Sean Chambers und Nathan Ooms bedanken für die großartige Zusammenarbeit!

Ganz besonders möchte ich aber meinen Eltern danken, ohne deren Rückhalt und Unterstützung meine Promotion sowie schon mein gesamtes Studium nicht möglich gewesen wären.